DEVICES FOR TERAHERTZ RETROMODULATION

by

Mark Henry Bergen

B.A.Sc., The University of British Columbia, 2014

M.A.Sc., The University of British Columbia, 2016

A THESIS SUBMITTED IN PARTIAL FULFILLMENT OF

THE REQUIREMENTS FOR THE DEGREE OF

Doctor of Philosophy

in

THE COLLEGE OF GRADUATE STUDIES

(Electrical Engineering)

THE UNIVERSITY OF BRITISH COLUMBIA

(Okanagan)

July 2021

The following individuals certify that they have read, and recommend to the College of Graduate Studies for acceptance, a thesis/dissertation entitled:

Devices for Terahertz Retromodulation

submitted by Mark Henry Bergen in partial fulfillment of the requirements of

the degree of Doctor of Philosophy .

Dr. Jonathan Holzman, School of Engineering, The University of British Columbia

Supervisor

Dr. Loïc Markley, School of Engineering, The University of British Columbia

Supervisory Committee Member

Dr. Thomas Johnson, School of Engineering, The University of British Columbia

Supervisory Committee Member

Dr. Rebecca Feldman, Irving K. Barber Faculty of Science, The University of British Columbia

University Examiner

Dr. Mira Naftaly, National Physics Laboratory

External Examiner

Abstract

The future of wireless communications will require an eventual transition from current wireless carrier frequencies in the low tens of gigahertz to hundreds of gigahertz and even low terahertz. This transition comes with a technological challenge since wireless transmitters for frequencies above 300 GHz are bulky and consume a significant amount of power. This limits their use to fixed installations and cannot be practically implemented for handheld mobile devices. Consequently, handheld mobile devices cannot transmit data with carrier frequencies over 300 GHz. This thesis proposes a novel solution to this challenge through the introduction of passive THz communication links. A passive THz link uses a retromodulator on a mobile device to return power transmitted by a fixed transceiver. This return power is encoded with data by the retromodulator enabling the mobile device to effectively transmit data at carrier frequencies above 300 GHz without needing an onboard THz transmitter. The goal of this thesis is to discover if a passive THz link is feasible given current technology for THz transmitters, detectors, and retromodulators. Theoretical predictions based on the work of other in the literature is presented first followed by an in-depth design and analysis of technologies required for THz retromodulation. Finally, a prototype THz retromodulator is designed and characterized to provide a true measure of the feasibility of passive uplinks. The results of a link budget analysis using the prototype THz retromodulator show that passive THz uplinks are indeed possible given current technology. This is the first known demonstration of THz retromodulation and will allow low-power handheld mobile devices to operate in bidirectional wireless THz communication system without the need for a THz transmitter.

Lay Summary

Demand for wireless bandwidth is constantly growing as more users demanding faster data rates every year. Consequently, the future of wireless communications will require an eventual transition from current wireless carrier frequencies, which are in the low tens of gigahertz, to terahertz frequencies. This transition is technologically challenging since wireless transmitters for frequencies above 300 GHz are bulky and consume a significant amount of power, preventing their practical use in handheld mobile devices. To address this challenge, this thesis proposes a novel mobile device design that enables it to access terahertz communication networks without a terahertz transmitter. This novel mobile device design is first analysed theoretically, then experimentally validated. It is found that this novel mobile device architecture is capable of operating in terahertz communication systems as a proof-of-concept, and the thesis outlines future work needed to bring this novel mobile device design to full fruition.

Preface

The work presented in this thesis is based on two current publications [J1], [J2], and one submitted work [S1]. Content from [J3] and [J4] appears briefly as supporting information in Chapter 2. In [J1], [J2], and [S1], I designed and ran the experiments, processed and interpreted the results, and wrote the manuscript. In all publications, J. F. Holzman contributed to the editing of the manuscript. In [J2], J. Reich, T. Ho, and F. Clark, assisted in the fabrication and testing of samples as well as the processing of data, while M Reid contributed to the editing of the manuscript. In [J3] and [J4], I assisted in the design and operation of a number of experiments. In [J3] and [J4], I helped design some of the experiments and gather data. Chapter 2 and Chapter 3 are based on the work submitted in [S1]. Chapter 4 is based on work from both [J2] and [S1]. Chapter 5 is based on the work found in [J1]. Chapter 6 is entirely unpublished work that may be submitted at a later date.

Published Journal Articles:

[J1] **M. H. Bergen** and J. F. Holzman, "Terahertz time-domain spectroscopy for ultrafast and quasi-static characterizations of germanium," *IEEE T. THz Sci. Technol.*, vol. 11, no. 1, pp. 54-61, Jan. 2021. [Appears in Chapter 5]

[J2] **M. H. Bergen**, J. Reich, T. Ho, F. Clark, M. Reid, and J. F. Holzman, "Terahertz field depolarization and absorption within composite media," *Appl. Phys. Lett.*, vol. 115, no. 4, p. 041901, Jul. 2019. [Appears in Chapter 4]

[J3] S. Alfihed, **M. H. Bergen**, J. F. Holzman, and I. G. Foulds, "A detailed investigation on the terahertz absorption characteristics of polydimethylsiloxane (PDMS)," *Polymer*, vol. 153, pp. 325-330, Sep 2018. [Appears in Chapter 2]

[J4] S. Alfihed, **M. H. Bergen**, A. Ciocoiu, J. F. Holzman, and I. G. Foulds, "Characterization and integration of terahertz technology within microfluidic platforms," *Micromachines*, vol. 9, no. 9, p. 453, Sep. 2018. [Appears in Chapter 2]

Submitted Journal Articles:

[S1] **M. H. Bergen** and J. F. Holzman, "Terahertz wireless communication systems: Challenges and solutions for the realization of effective bidirectional links," *Proc. IEEE*, Submitted Sep. 2020. [Appears in Chapter 2, Chapter 3, and Chapter 4]

Table of Contents

List of Tables

List of Figures

List of Symbols

a – Aperture diameter

a_{m} – Micro-hole array pitch

A – Aperture area

A_{ϕ} – Effective (diffusion broadened) spot size

B – Bandwidth

c – Speed of light

d – Sphere diameter

d_{m} – Micro-hole array diameter

D_{d} – Detector directivity

D_{r} – Retromodulator directivity

D_{t} – Transmitter directivity

DR(ω) – Dynamic range

$E(\omega)$ – Measured THz amplitude spectrum with sample

$E_{\mathrm{E}}(\omega)$ – Estimated THz amplitude spectrum

E_{t} – Transmitted electric field

$E_0(\omega)$ – Incident electric field amplitude or background amplitude spectrum

Δf – Free spectral range

G_{op} – Optical generation rate

$\hbar$ – Reduced Planck constant

i – Index

I – Intensity

I_0 – Incident intensity

I_{on} – Intensity when the modulator is on

I_{off} – Intensity when the modulator is off

j – Imaginary unit

k – Wavenumber

k_0 – Free space wavenumber

k_{α} – Scaling constant

k_{B} – Boltzmann constant

m_{e}^{*} – Effective mass of electrons

m_{h}^{*} – Effective mass of holes

$n(\omega)$ – Refractive index

$n_c(\omega)$ – Compensated refractive index

n_E – Estimated refractive index

$\Delta n(\omega,t)$ – Change in refractive index

$N(t)$ – Charge carrier density

N_d – Depolarization factor

NEP – Noise equivalent power

OA – Optical axis

P_d – Detected power

P_t – Transmitted power

P_N – Noise power

P_r – Retromodulator power

q – Elementary charge

r – Reflection coefficient

R – Product of two reflection coefficients

R_{link} – Link length

R_{sv} – Surface-area-to-volume ratio

S – Surface recombination velocity

t – Time

t_{in} – Transmission coefficient into the material

t_{out} – Transmission coefficient out of the material

T – Product of two transmission coefficients

T_N – Temperature

T_p – Reference sinusoid period

V – Volumetric fraction

V_0 – Voltage signal amplitude

V_1 – Voltage signal amplitude for configuration one

V_2 – Voltage signal amplitude for configuration two

V_d – Voltage signal

α – Power absorption coefficient

α_{ch} – Channel power absorption coefficient

β – Exponential constant

δ – Modulator thickness

ε_0 – Free space permittivity

$\tilde{\varepsilon}(\omega,t)$ – Dielectric constant

$\tilde{\varepsilon}_c(\omega)$ – Composite dielectric constant

$\tilde{\varepsilon}_h(\omega)$ – Host dielectric constant

$\tilde{\varepsilon}_i(\omega)$ – Intrinsic dielectric constant

$\tilde{\varepsilon}_p(\omega)$ – Particle dielectric constant

$\chi_e(\omega,t)$ – Electrical susceptibility for electrons

$\chi_h(\omega,t)$ – Electrical susceptibility for holes

λ – Wavelength

η – Impedance of free space

η_{IA} – Incident angle efficiency

η_{in} – Insertion efficiency

η_{mod} – Modulation efficiency

η_{re} – Retroreflection efficiency

ϕ – Incident azimuthal angle

$\phi_E(\omega)$ – Estimated THz phase spectrum

$\phi_{THz}(\omega)$ – Measured THz phase spectrum

θ – Incident polar angle

θ_d – Divergence angle

θ_i – Modulator phase delay, frequency dependent

$\kappa(\omega)$ – Extinction coefficient

$\kappa_c(\omega)$ – Compensated extinction coefficient

$\kappa_{max}(\omega)$ – Maximum measurable extinction coefficient

$\Delta\kappa(\omega,t)$ – Change in extinction coefficient

μ_e – Electron mobility

μ_h – Hole mobility

$\sigma(\omega)$ – Standard deviation in measurement spectrum

$\sigma_\kappa(\omega)$ – Standard deviation in measured extinction coefficient spectrum

τ_d – Pump probe time delay

τ_r – Charge carrier lifetime

$\tau_{s,e}$ – Scatter time of electrons

$\tau_{s,h}$ – Scatter time of holes

$\tau_{r,b}$ – Bulk charge carrier lifetime

ω – THz angular frequency

ω_{pr} – Probe angular frequency

ω_{pp} – Pump angular frequency

ω_{ref} – Reference angular frequency

$\Im[\bullet]$ – Fourier transform operator

List of Abbreviations

AL – Active link
BWO – Backward wave oscillator
CCRR – Cornercube retroreflector
COC – Cyclic olefin copolymer
CW – Continuous wave
DSP – Digital signal processing
FOV – Field of view
HDPE – High-density polyethylene
HHG – High harmonic generation
HRFZ Si – High resistivity float zone silicon
HSO – High-speed oscillators
IF – Intermediate frequency
IMPATT – Impact ionization avalanche transit-time
IPL – Ideal passive link
IR – Infrared
LO – Local oscillator
NIR – Near infrared
OA – Optical axis
OHD – Optical heterodyning
OPTP – Optical pump terahertz probe
PDMS – Polydimethyl siloxane
PP – Polypropylene
PS – Polystyrene
PTFE – Polytetrafluoroethylene
QAM – Quadrature amplitude modulation
QCL – Quantum cascade laser
QT – Quantum transition
RPL – Real passive link
SEM – Scanning electron microscope
SHM – Subharmonic mixer
SNR – Signal-to-noise ratio
TDS – Time-domain spectroscopy
THz – Terahertz
UHMWPE – Ultra-high molecular weight polyethylene
UV – Ultraviolet
ZB – Zero-bias

Acknowledgements

I would like to take this opportunity to thank the many individuals and organisations whose financial, technical, and moral support made this thesis and the work it contains possible.

First, I would like to acknowledge the endless support and technical assistance of my supervisor Dr. Jonathan Holzman. His tireless efforts assisting me in all stages of this work were instrumental in bringing it to fruition. I would like to thank my committee members, Dr. Thomas Johnson and Dr. Loïc Markley, for serving on my committee and giving thoughtful advice when I needed it. I would also like to thank my university examiner, Dr. Rebecca Feldman and my external examiner, Dr. Mira Naftaly, for taking the time to adjudicate my thesis.

Many of the experiments carrier out in this thesis were made possible by the technical support provided by Tim Giesbrecht, Praveen Rajan, David Zinz, Emily Zhang, Aria Fani, Jiyee Yoon, Chris Seib, Durwin Bossy, Ray Seida, David Arkinstall, and Alec Smith. Thank you to all of you for being patient with some of my more complicated ideas.

Next, I would like to acknowledge the support and contributions from everyone in the Integrated Optics Laboratory. I foremost would like to thank Salman Alfihed for the time spent working on terahertz spectroscopy and microfabrication. You were a huge contribution to my understanding of THz material properties and an enjoyable person to work with. I would also like to thank Mike Mitchell, Jason Reich, Tyler Ho, Emily Mellors, and Flynn Clark for helping me with the THz composite work over the years. You all spent a lot of time fabricating samples so that we could better understand THz composites. Finally, I would like to thank the other members of the Integrated Optics Laboratory for making my time there enjoyable. These are Ilija Hristovski, Naomi Fredeen, Adebola Adebowale, Mitch Westgate, Adrian Boivin, Nikolai Lesack, Ana Ciociou, Alec Yan, and everyone else who sat with us for tea.

I would also like to acknowledge the people outside the Integrated Optics Laboratory who have contributed to this thesis as well. Thank you to Dr. Matt Reid for the input on THz materials. Thank you as well to Dr. Jerome Faist

and the entire Quantum Optoelectronics Group at ETH Zurich for welcoming me into your group for several months. Finally, I would like to thank Dr. Lukas Bichler and Somi Doja for their technical assistance milling silicon particles and Tim Abbott for his help with particle size analysis.

I would like to recognize the significant financial support of the Natural Sciences and Engineering Research Council of Canada and the UBC School of Engineering.

Finally, I would like to acknowledge the endless patience and encouragement of my family. I would like to thank my parents, Cliff and Donna, and my parents-in-law, Andy and Jacquie, for your financial and moral support over the years. Most importantly, I would like to thank my wife Lisa. You have been with me every step of this journey, you have seen the highs and the lows, and I would not have completed this thesis without your help in so many ways.

For Lisa and Isaac, my wonderful family.

Chapter 1: Introduction

Over the past several decades, the invention and proliferation of personal electronic devices has changed nearly every aspect of society. With the rise of electronic devices came the demand for these devices to be connected to each other, resulting in the internet. Internet access first required the design of wired networks, then eventually the design of wireless networks as electronic devices became smaller and more portable (i.e., smartphones and laptops). One major limitation of wireless networks is the spectrum they must occupy. Since the wireless spectrum is a limited resource, wireless service providers and network operators compete for the rights to use portions of the wireless spectrum. In addition, since each portion of the wireless spectrum can typically be used by only one device at a time, there is a limit to the number of devices that can access a wireless network in a geographical region. This has led to the "wireless spectrum crunch", where spectrum demand has exceeded supply [1], [2].

There are two options to alleviate the wireless spectrum crunch. The first option is to reduce the size of the geographical region covered by a wireless network, which is called a cell. Development of pico- and femto-cells are currently underway [1], [3], [4]. This promises to allow more total connections since portions of the spectrum can be reused in neighbouring cells. The second option is to expand the useable spectrum. The current upper limit of the licensed wireless spectrum is 300 GHz [1], [2], although most commercial devices can only operate up to about 40 GHz. Operating in higher regions of the wireless spectrum increases the network bandwidth allowing for more users at current data rates or a similar number of users at higher data rates. Research into technologies that utilize the wireless spectrum up to 300 GHz is already well established [3], [4], [5], [6], [7] and the current 300 GHz limit will soon be exceeded.

To access the wireless spectrum above the current 300 GHz limit, data carrier frequencies will have to move from the radio frequency regime to the optical regime. Optical frequencies above 300 GHz include infrared (IR), visible, and ultraviolet (UV) regions. The electromagnetic spectrum with its associated regions is shown in Figure 1.1. The X-Ray spectrum is listed in the optical region for completeness, though communication at these frequencies would be extremely challenging.

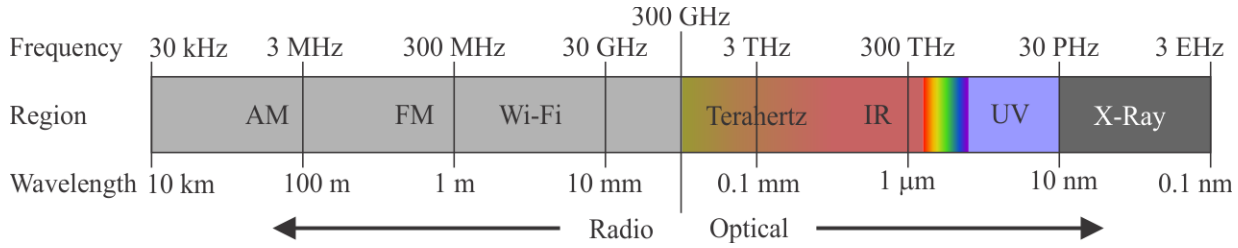

Figure 1.1: A diagram of the electromagnetic spectrum is shown, with the visible light region is denoted by the rainbow.

There has been extensive research into using optical frequency channels to improve wireless data rates [8], [9]. Optical communication research is focused around visible, near-IR (NIR), and mid-IR frequencies, with wavelengths ranging from 10 μm to 400 nm. A good portion of this research is focused specifically on the NIR wavelength 1550 nm, which is the primary wavelength in modern fibre communication systems [8], [9], [10], [11], [12]. In these systems, data is modulated onto a 1550 nm laser source by either modulating the amplitude of the laser emission directly or by using an external modulator [9], [11]. In addition to compatibility with current fibre optic technology, optical and NIR wavelengths are advantageous due to their low atmospheric absorption, ultra-high carrier frequencies (from 30 THz to 1000 THz), and simple generation and detection using lasers and photodetectors. Two disadvantages, especially for the short wavelengths, are difficulty implementing coherent communication systems as well as eye safety considerations. Coherent communication systems allow information to be encoded not only onto the carrier amplitude, but also the carrier phase. These systems are superior to amplitude-based communication systems due to their increased data transmission capabilities by exploiting complex phase modulation schemes such as quadrature amplitude modulation (QAM). Additionally, coherent communication systems have increased immunity to noise since atmospheric turbulence manifests mainly as amplitude noise, as opposed to phase noise. Implementing coherent systems capable of encoding and detecting subtle phase shifts becomes understandably more difficult as the wavelength decreases. However, for laser-based point-to-point wireless systems, coherent free-space optical communication links capable of 5.6 Gbit/s have been demonstrated over 142 km [12]. Unfortunately, these links require precise alignment and complex electronic and optical systems on both ends making them ill-suited for portable consumer devices. The second disadvantage to these portions of the wireless spectrum is eye safety, which is especially stringent for the visible and NIR spectrum as wavelengths in this range can cause permanent eye damage at relatively low powers [13]. Therefore, these

systems require sensitive detection systems due to lower allowable transmitted power, which means implementing more technically challenging coherent detection systems.

Ultraviolet frequencies, which range in wavelength between 400 nm and 10 nm, have also been considered for optical communication [14], [15]. However, health concerns for wavelengths below 320 nm make this region of limited use since these wavelengths are known to cause skin cancer [16]. From a technical standpoint, UV's incredibly high carrier frequencies (> 1000 THz) and simple laser and photodetector design, make UV communication systems intriguing. These systems can also operate in non-line-of-sight environments using atmospheric scattering [15]. Unfortunately, most conventional types of glass have significant UV absorption [17] and UV's extremely short wavelengths make coherent systems enormously challenging to design. Therefore, UV wireless communication systems are not only a health risk, but also technologically challenging to implement.

The final frequency regime considered for optical communication is the far-IR or terahertz (THz) regime, with wavelengths ranging from 1 mm to 10 μm [1], [2]. At these longer wavelengths, coherent communication systems are less challenging to implement and higher data rates through techniques such as QAM have been demonstrated [18]. However, challenges such as high atmospheric absorption, high absorption in conventional glass optics, and difficulties in generating and detecting THz frequencies make communication in this region a challenge. Fortunately, technological advances such as polymer lenses [19], [20] and high-power THz sources [21], [22], [23], [24] have been developed in recent years making THz communication more feasible. These technological advances now allow THz communication to be considered as a viable, exciting new frontier in communication technology.

1.1 Terahertz Communication

In this section, a more detailed description of THz radiation and THz communication systems will be given. The THz spectrum covers frequencies from 300 GHz to 30 THz, which corresponds to wavelengths between 1 mm and 10 μm. This region of the electromagnetic spectrum has traditionally seen little interest due to difficulty generating and detecting THz signals. The THz spectrum lies far enough above frequencies that can be generated using conventional electronic oscillators that, historically, implementing continuous wave (CW) THz sources and

detecting THz frequencies using electronic oscillators and antennas was not practically feasible. Recently though, technological advances over the past decade have allowed conventional electronic devices to operate at the bottom of the THz spectrum around 300 GHz [21], [22]. The THz spectrum also lies below the lower frequency limit of uncooled semiconductor lasers and photodetectors. Thermal effects are detrimental to laser sources with photon energies in the THz spectrum meaning that any conventional THz laser would need to be cooled to operate properly, with longer wavelengths requiring more cooling. In addition, any conventional THz photodetector would also need to be cooled to prevent ambient thermal noise from overloading it. Consequently, there were historically far fewer studies in the THz spectrum than in the radio frequency and IR spectra.

Though prior work exists [25], research into the THz spectrum was truly kickstarted in 1984 with the invention of the photoconductive switch emitter and detector [26]. In a photoconductive switch emitter, ultrafast laser pulses (< 1ps) are used to quickly generate charge-carriers in a semiconductor substrate. If these charge-carriers are subject to an applied electric field, they will accelerate and radiate energy. This creates a pulse of electromagnetic energy whose frequency and bandwidth depend on the rate at which the charge-carriers were generated. For a sub-picosecond laser pulse, this corresponds to frequencies in the THz spectrum. In this thesis, the term emitter will only refer to a photoconductive switch, not to any other THz generation method. Originally, detection of these pulses was carried out using a similar structure to the emitter. A second laser pulse hits another photoconductive switch gap generating more charge-carriers which will drift in the presence of a THz electric field. This charge-carrier drift is measured using a high-gain transimpedance amplifier. By synchronizing the emitter and detector laser pulses, one can create a time-resolved measurement of the THz pulse. An alternative, though similar, THz detection methods exists and was used for most of the work in this thesis. This method will be described in detail in Chapter 4. There are several advantages to photoconductive switch emitters and detectors including broad bandwidth, room temperature operation, and coherent detection. The requirement for an ultrafast laser is somewhat onerous, though the many applications made possible by photoconductive switch emitters and detectors, including spectroscopy [27], [28], [29], [30], [31], [32], [33] and imaging [34], justify this requirement. The main disadvantage of using photoconductive switches for emitters and detectors for THz communication is their pulsed

operation, as opposed to CW operation which is required for communication links. Nonetheless, photoconductive switches can be used for proof-of-concept analyses for many optical components in the THz spectrum such as lenses and modulators.

There has been a great deal of effort put into developing high-power CW THz transmitters and high-speed THz detectors in recent years. Transmitters capable of emitting several hundred milliwatts [21], [22], [23], [24], have been demonstrated as well as coherent detectors [18], [21], [35], [36], although both are still somewhat bulky and consume a large amount of power. These new THz transmitters and detectors have enabled several demonstrations of wireless THz communication links [18], [35], [36], [37] with data rates in excess of 10 Gbps [18], [35], [36]. Unfortunately, these systems sacrificed transmitter power for the sake of speed, which has limited their use to short range, highly directional transmission [35], [37]. This prevents these systems from being feasible in practical wireless communication links where signals need to broadcast over a wide area. Additionally, none of the aforementioned systems were capable of bidirectional wireless THz communication, although one work proposed it [36]. While these recent demonstrations of high-speed wireless THz communication links are promising, they still require bulky THz transmitters and detectors, both of which use a significant amount of power. In a practical wireless THz communication link, these transmitters and detectors may find use in large, fixed THz transceivers. However, the majority of mobile network connections are from small, mobile transceivers. These mobile transceivers cannot fit nor provide enough power for current THz transmitters. Ultimately, future wireless THz communication systems will require more compact, powerful transmitters for mobile transceivers to close the communication link, i.e., have the detected signal powers be well above the detector noise floor at link lengths of a few metres. This of course assumes that every device in the network must be capable of transmitting a THz signal. Relaxing this stipulation opens the door for other novel technological solutions that may be capable of establishing bidirectional wireless THz communication links.

1.2 Terahertz Retromodulation

One promising solution for the realization of bidirectional wireless THz communication links without requiring a THz transmitter in each mobile transceiver is THz retromodulation. Terahertz retromodulation is an extension of

optical retromodulation [38], [39], [40], [41], [42], in which visible or NIR radiation is transmitted by a fixed transceiver to a mobile transceiver, then modulated and retroreflected by the mobile transceiver for its return to the fixed transceiver. The mobile transceiver can then piggyback its data onto the signal returning to the fixed transceiver and avoid the need to broadcast power. In a conventional realization of a bidirectional wireless THz communication system, the fixed transceiver would transmit power to the mobile transceiver over an active downlink, and the mobile transceiver would transmit power to the fixed transceiver over an analogous active uplink. Conversely, for the proposed realization of a bidirectional wireless THz communication system based on THz retromodulation, the fixed transceiver would still transmit power to the mobile transceiver over an active downlink; however, the mobile transceiver would retroreflect power from the active downlink back to the fixed transceiver over a passive uplink. Consequently, for this work, conventional bidirectional wireless THz communication systems will be referred to as active THz links and bidirectional wireless THz communication systems based on THz retromodulation will be referred to as passive THz links. Simple illustrations of an active THz link and a passive THz link are shown in Figure 1.2. Removing the power transmission requirement for the mobile transceivers in the passive THz link results in exceedingly low power consumption on the part of the mobile transceiver.

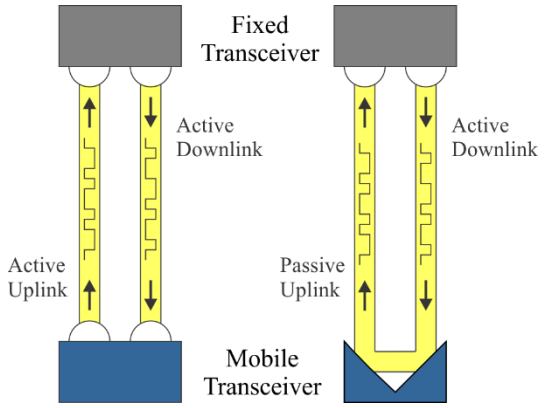

Figure 1.2: Representative schematics of the active and passive THz links. The active THz link is shown on the left, with both a transmitter and detector on the fixed transceiver and the mobile transceiver. The passive THz link is shown on the right, with a transmitter and detector on the fixed transceiver and a THz retromodulator on the mobile transceiver, retroreflecting power from the active downlink to establish the passive uplink.

Despite the benefits, passive THz links come with a few implementation challenges. The first challenge for passive THz links is that the mobile transceiver must provide a detectable level of power to the fixed transceiver regardless of whether an active or passive THz link is used. A simple link budget analysis can be performed to determine

whether a given system design can close the link. For active downlinks and active uplinks, the common Friis transmission equation can be used [43]. For passive uplinks, a retromodulation equation can be derived from the Friis transmission equation. The second challenge for passive THz links is retromodulator design. Optical retromodulators typically employ cornercube retroreflectors made of metalized panels [39], [41], [42] or spherical retroreflectors made of a dielectric glass [38] along with a variety of discrete and integrated modulators [38], [39], [40], [44], [45]. However, since most materials and devices have very different behaviour in the THz spectrum than they do in the visible or NIR spectra, entirely new structures and/or materials may be needed to create THz retroreflectors and modulators. While little investigation has gone into THz retroreflectors [46], [47], [48], much more effort has gone into THz modulators for free-space applications with optical modulators [49], [50], [51], [52], and electronic modulators [53], [54], [55], [56] being the most popular to date. These advances indicate that it should be possible to design and fabricate THz retromodulator for passive THz links using current technology.

1.3 Thesis Outline

The objective of the work described in this thesis, is to assess if THz retromodulation is feasible using current technology. If so, the secondary objective is to demonstrate a passive uplink using THz retromodulation. No mention of passive THz uplinks or THz retromodulation have appeared in the literature to date. Therefore, a successful demonstration of this technology would be the first of its kind. The thesis will be organized into seven chapters. Chapter 1 is an introduction to THz communication and THz retromodulation. Chapter 2 contains a comprehensive literature review of current wireless THz communication technologies including THz transmitters, detectors, free-space modulators, retroreflectors, and channel modelling. This chapter will also include a review of optical retromodulators to draw inspiration for THz retromodulators. Chapter 3 consists of a detailed link budget analysis based on the specifications of the devices reviewed in Chapter 2. This chapter draws conclusions on the feasibility of THz retromodulation. Chapter 4 and Chapter 5 lay out experimental work done to design and implement THz retroreflectors (Chapter 4) and modulators (Chapter 5). Chapter 6 presents results for a simple THz retromodulator based on the devices described in Chapter 4 and Chapter 5. Chapter 7 contains concluding remarks as well as avenues of future research.

Chapter 2: Literature Review

In this chapter, an in-depth literature review of wireless THz communication and the requisite technologies required for THz retromodulation will be carried out. The chapter begins with a review on aspects of a wireless THz communication link that are common to both active and passive THz links. This includes THz transmitters and detectors, as well as some simple channel modelling. After that, the review shifts to aspects specific to passive uplinks including THz retroreflectors and free-space modulators. Finally, this chapter will conclude with a brief look at some optical retromodulator designs to see if adapting them to THz retromodulation is feasible.

2.1 Common Considerations for Active and Passive Uplinks

There are several systems that are common to both active and passive THz links. These include THz transmitters and detectors, as well as channel models. Two of the following subsections will introduce the most prominent technologies capable of high-power CW THz transmission and high-speed THz detection. There have also been two excellent reviews written recently by Lewis on these topics [57], [58] and an excellent full-system review by Alayan *et al*. [59]. For the interested reader, these reviews also include information pertaining to THz transmission and detection technologies relevant to other THz research fields such as spectroscopy and imaging. The review here will highlight literature values for the most promising transmitter and detector technologies to be used in the link budget analysis in Chapter 3.

2.1.1 Transmitters

High-power, continuous wave THz transmitters are the backbone of any THz wireless communication link. This is especially true for passive THz links as retromodulated signals tend to be quite weak. Presently though, compact, high-power THz transmitters are still in the development phase, with no single technology capable of fulfilling all of these requirements. In "The 2017 terahertz science and technology roadmap" a review of THz technologies was done with thought given to THz communication. The conclusion to the communication portion of the review states, "*The most important challenges for commercial realisation of this technology are the development of compact and efficient THz sources providing continuous wave output power levels up to 100 mW and the development of compact*

electronically steerable antenna arrays to minimise wireless link loss." [60]. Clearly, the importance of THz transmitters in any wireless THz communication link cannot be overstated. Presently, a wide variety of potential transmitters exist for wireless THz communication links. These include, but are not limited to, quantum cascade lasers (QCLs) [24], [61], [62], backward wave oscillators (BWOs) [23], [46], [63], high harmonic generation systems [21], [64], [65], high-speed electronic oscillators [22], [66], [67], and optical heterodyning systems [18], [35], [36].

The first THz QCL was demonstrated in 1998 and generated only a few picowatts of power at 3.4 THz [68]. Initial challenges with the THz QCL were related to the cryogenic operating temperatures required for lasing. Consequently, early THz QCLs could only operate in pulsed mode as to limit heating of the solid-state laser substrate. Modern THz QCLs produce transmitted powers in excess of 100 mW and have made significant improvements to the aforementioned limitations. On the subject of high-temperature QCLs, Bosco *et al*. recently demonstrated a THz QCL that could operate at a record high temperature of 210 K [61]. That temperature was high enough that thermoelectric cooling was sufficient for stable laser operation. The device lased at 3.9 THz and produced >1 mW of transmitted power at 210 K. Their device also produced approximately 200 mW at 40 K, although performance at all temperatures was only specified for pulsed operation. On the subject of high-power, continuous wave QCLs, Wang *et al*. demonstrated a THz QCL capable of 230 mW continuous wave emission at 3.1 THz [24]. However, the operating temperature for this device was 15 K. One other drawback inherent to THz QCLs for communication applications is their lack of frequency tunability. Modern communication systems use frequency division multiplexing to increase the number of users for a particular transmitter, which requires transmitter frequency tunability. One potential way to overcome this challenge was demonstrated by Curwen *et al*. who fabricated and tested a tunable wavelength QCL with a tuning range of 3.18 – 3.79 THz at 77 K [62]. The operating frequency was selected by adjusting the cavity length of the laser in low-order mode operation. Continuous wave powers ranging from 5-15 mW were measured depending on frequency. While these recent advancements show that progress is being made towards a continuous wave THz QCL that operates at room

temperature, an ideal THz QCL that provides a significant amount of continuous wave power without cryogenic cooling is likely still several years away.

Backward wave oscillators are another novel THz transmitter alternative. These devices consist of an electron beam surrounded by a waveguide. Any signal present in the waveguide will create an electric field that interacts with the electron beam causing the electrons to cluster in regions of large positive electric field. If this cluster of electrons propagates through the waveguide with the same velocity as the phase velocity of the signal in the waveguide, amplification of the electron density occurs. Finally, the time-varying electron density feeds power back into the waveguide amplifying the signal in it. For this to work, the electron velocity must match the THz signal phase velocity. This can be achieved by adjusting the voltage creating the electron beam. Many designs for BWOs have been presented in the literature [63], however, few have actually been fabricated. One example of a BWO that has been fabricated and tested was done by San *et al*., whose design was based on the slow wave structure architecture. Their device produced 800 mW around 370 GHz [23]. While these devices may seem to be an ideal choice for THz transmitters, the frequency and power stability of these systems are unknown and may be inadequate for THz wireless communication applications.

Since electronics technology is already matured to the point of commercialization below 40 GHz, it stands to reason that it is only a matter of time before conventional electronics are capable of operation in the THz spectrum. In fact, this is already the case to some extent. The most popular method of generating THz frequencies using conventional electronics is high harmonic generation (HHG). This involves taking a conventional oscillator and multiplying its output signal until it contains frequency components in the THz spectrum [21], [64], [65]. These transmitters are comprised of electronic oscillators typically operating below 20 GHz, whose output is then frequency doubled or tripled multiple times until it reaches >300 GHz. These transmitters are much more compact than THz QCLs but produce less power as a result of the inefficient frequency multiplication process. This inefficient frequency multiplication process compounds for higher output frequencies, as can be seen in the plot of transmitted power, P_T, vs frequency for various sources in Figure 2.1.

One major advantage to high harmonic generation is maturity of the technology. Consequently, commercial companies exist that offer CW THz transmitters based on high harmonic generation. One company, Virginia Diodes, has a wide range of commercially available THz sources based on high harmonic generation. Transmitted power varies widely and drops off dramatically for higher frequencies due to the additional frequency multiplier stages required. The company specifies multiplier power efficiencies of 4% for broadband multipliers up to 20% for narrowband multipliers using planar GaAs Schottky diodes to carry out the nonlinear mixing. This allows for transmitted powers of up to 1 W below 100 GHz, which drops off to about 50 mW at 300 GHz and 1 mW at 1 THz [21].

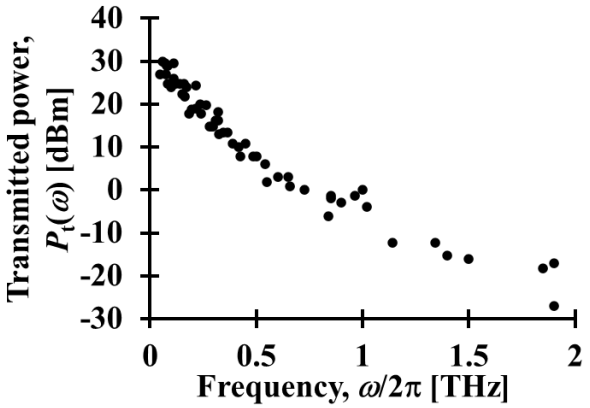

Figure 2.1: Transmitted power of various CW THz transmitters based on HHG from Virginia Diodes is shown as a function of THz frequency. Data from https://www.vadiodes.com/en/products/custom-transmitters. Retrieved March 1, 2021.

The other popular method of generating THz frequencies using conventional electronics is to eschew frequency conversion altogether and directly generate THz frequencies using specialized high-speed oscillators (HSO). Active devices with negative differential resistance, such as impact ionization avalanche transit-time (IMPATT) diodes and Gunn diodes, are capable of oscillating at frequencies above 100 GHz directly [22], [66], [67]. The use of IMPATT diodes to generate THz frequencies is not new and, like high harmonic generation, the technology has matured to the point of commercialization. One company, TeraSense, offers THz transmitters based on IMPATT diode oscillators with transmitted powers of 800 mW at 100 GHz and 40 mW at 280 GHz. The main challenge to using IMPATT diodes as reliable THz transmitters is their large noise characteristics caused by the impact ionization process that gives the device its name. Research is ongoing to reduce this noise [66], as well as on other

device improvements to achieve higher power at higher frequencies [69]. The other common high-speed oscillator is a Gunn diode. Gunn diodes operate similarly to IMPATT diodes so their performance as a THz source is comparable. Recently, a transmitted power of 25 mW at 95 GHz was demonstrated [70]. While progress is being made the in the field of high-speed oscillators, high harmonic generation offers somewhat higher transmitted power with easier frequency tunability making it the more attractive option.

Optical heterodyning (OHD) is the most popular method of generating continuous wave THz signals in previously demonstrated wireless THz communication links [18], [35], [36]. Optical heterodyning involves taking two mid-IR lasers that have a frequency difference of less than one THz and mixing them in a non-linear device such as a uni-travelling carrier photodiode [18]. The popularity of this technique is based on the maturity of mid-IR lasers, especially around the 1550 nm telecom wavelength, which have very narrow linewidths and simple wavelength tuning. Additionally, the availability of fibre amplifiers, polarization elements, and modulators for these wavelengths along with the fact that signals can be coupled into fibre systems, make it much easier to implement complex modulation schemes such as QAM than it would be at THz frequencies [18]. The one major downside to optical heterodyning is the extremely low power output, which requires most wireless THz communication links using them as sources to be point-to-point with a nearly collimated THz beam. While many demonstrations do not give transmitted power [18], [35], one work estimated their transmitted power based on the signal at the detector to be approximately 1 μW around 300 GHz [36]. While this transmitted power is very low, THz amplifiers in that band have recently been shown to give up to 20 dB of gain [71]. This could potentially allow optical heterodyning transmitters to work over more practical link lengths. For now though, most wireless THz communication links with optical heterodyning transmitters are point-to-point over a short distance with a nearly collimated THz beam.

Clearly, there are many potential transmitter technologies for bidirectional wireless THz communication links. Terahertz QCLs are promising due to their high transmitted power; however, cooling requirements remain a challenge. High-speed oscillators and high harmonic generation transmitters are compact, have significant transmitted power at lower frequencies, and are compatible with current electronic devices, but are also energy inefficient. Backward wave oscillators are a novel, high-power THz source; however, suitable beam quality for

wireless communication applications has yet to be demonstrated. Optical heterodyning has been demonstrated in wireless THz communication links, but its low transmitted power requires some type of beam-steering system to operate over a wide area. Table 2.1 shows some properties of the most promising results from the literature for various THz transmitter technologies. Two theoretical transmitters (Theory) were also included with transmitted power levels similar to HFO and HHG systems, but at higher frequencies. This was done so that reasonable results can be obtained for these frequencies in the link budget analysis in Chapter 3.

Table 2.1: Transmitter parameters for various analysed systems

System	P_t [dBm]	Frequency, $\omega/2\pi$ [THz]	Technologies	Ref
1	16	0.28	HFO	[22]
2	-30	0.30	OHD	[36]
3	18.7	0.32	HHG	[21]
4	29	0.37	BWO	[23]
5	20	0.65	Theory	-
6	20	0.85	Theory	-
7	23.6	3.1	QCL	[24]

These parameters will be used in the link budget analysis in Chapter 3 to determine not only the feasibility of THz retromodulation as a whole, but the specific feasibility of THz retromodulation using the various transmitter technologies.

2.1.2 Detectors

Terahertz detectors in their various forms have found use in many applications including wireless THz communication links [18], [35], [36], [37]. An exhaustive review of THz detectors was done last year by Lewis, who gives specifications and comments on the utility of various detector technology [58]. While THz detectors based on bolometers [72], Golay cells [73], quantum transitions [74], and Schottky diodes [18], [35], [36], [37] have all been successfully demonstrated, most are unsuitable for wireless THz communication links. Detectors in a wireless THz communication links must have a fast response time and be low cost. This eliminates the use of bolometers, due to the expense of their cryogenic requirements [72], as well as Golay cells and other pyroelectric detectors due to their slow response time [73]. Quantum transition devices also require extensive cooling, but their

high data rates and carrier frequencies, above 3 THz [74], make them an intriguing option when paired with cryogenically cooled QCLs. The remaining THz detector technology is the Schottky diode detector, which is found in the overwhelming majority of proof-of-concept wireless THz communication links.

Schottky diode detectors are commonly used for THz detection in the literature [18], [35], [36], [37]. With the development of planar GaAs Schottky diodes, reliable detectors can be fabricated with good repeatability [65]. The high-speed and non-linearity of Schottky diodes allow them to be used in two different detector designs. The first is the zero-bias detector, which essentially operates as an envelope detector for THz signals. Zero-bias Schottky diode detectors (ZB) are simple and require no power supply, but they suffer from lower signal to noise ratios than the second design. Since ZB detectors are envelope detectors, they can only detect incoherent or amplitude modulation. Therefore, individual frequency channels must be filtered out before detection. The second Schottky diode detector is the heterodyne mixer. The non-linear properties of the Schottky diode allow it to be used to mix the received THz signal with a local oscillator, which is typically generated using high harmonic generation. A simple diagram of the heterodyne mixing process is shown in Figure 2.2.

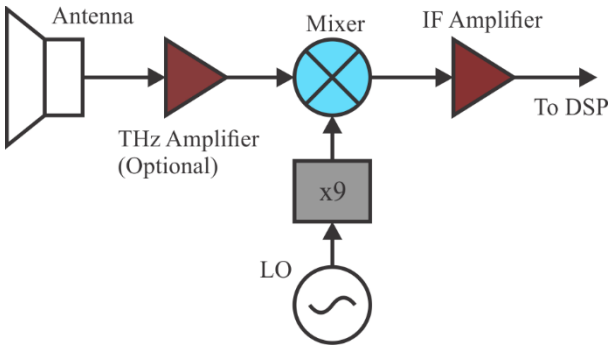

Figure 2.2: A simple schematic of a THz heterodyne mixing detector is shown. An antenna detects the THz signal and feeds it into an optional THz preamp before it is mixed with a THz local oscillator. The THz local oscillator is generated by feeding a GHz local oscillator (LO) into a frequency multiplier, which is shown as x9 here for illustrative purposes. After mixing, the down-converted signal is amplified by an intermediate frequency (IF) amplifier before being sent to conventional digital signal processing (DSP).

One note is that most heterodyne mixing detectors use a subharmonic mixer (SHM), which allows the THz local oscillator to operate at a fraction (typically half) of the frequency of the incoming THz signal. One distinct advantage

that the subharmonic mixer has over the zero-bias detector is that phase information can be retrieved from the detected signal allowing bandwidth enhancing techniques, such as QAM, to be implemented [18].

The maturity and prevalence of Schottky diode detectors have resulted in commercial availability for both detector systems from Virginia Diodes. Their zero-bias detectors can operate at various frequencies between 100 GHz and 1 THz with noise equivalent powers from 1 to 10 pW/√Hz and a maximum bandwidth of around 40 GHz. Their subharmonic mixing detectors are also optimized for various frequency ranges between 100 GHz and 1 THz, with one device operating at 300 GHz with a noise temperature of 1000 K and a conversion loss of about 7 dB [21]. The maximum intermediate frequency for that device was 40 GHz, which sets the upper data bandwidth limit. Multiple works from Shams *et al*. as well as work from Jia *et al*. use subharmonic mixers from Virginia Diodes and experimentally show noise floors below -65 dBm after mixing [18], [35], [36]. One can determine from the given specifications that subharmonic mixing detectors are several orders of magnitude more sensitive than zero-bias detectors, which is to be expected from a coherent detector. Both zero-bias and subharmonic mixing detectors will be investigated in the link budget analysis later.

Before comparing detector technologies, a brief discussion on the various methods of quantifying noise needs to be given. The two Schottky diode detector designs have their noise quantified differently: the zero-bias detector in terms of noise equivalent power, and the subharmonic mixing detector in terms of noise temperature. Noise equivalent power is a measure of how much noise is present in the detector per unit of bandwidth when no signal is incident on the detector. For optical detectors such as photodiodes, this is expressed in W/√Hz, and typically incorporates the responsivity of the photodiode so that the calculated noise is an electrical power. The total noise power can be calculated by taking the noise equivalent power of the detector and multiplying by the square root of the bandwidth over which detection is taking place. Therefore, lower noise equivalent powers and narrower detection bandwidths are more desirable [75]. Noise temperature is a measure of how much noise would be generated by an equivalent matched resistor at that temperature. When expressed in terms of power, the noise temperature is independent of the actual load resistance. Noise power is determined by using $P_N = k_B T_N B$, where k_B is the Boltzmann constant, T_N is the equivalent temperature, and B is the detection bandwidth. Like noise equivalent

power, the total noise out of a detector described by noise temperature is dependent on bandwidth; however, noise temperature is linearly dependent on bandwidth as opposed to the square root dependence seen in noise equivalent power. Table 2.2 gives the noise equivalent power or noise temperature of the detectors described in this subsection along with the total noise power for a 1 GHz bandwidth. A conversion loss is also given for the subharmonic mixers to account for other losses in the detector. For comparison, the quantum transition detector described in [74] is included in the table.

Table 2.2: Detector parameters for various technologies

Technologies	Frequency, $\omega/2\pi$ [THz]	Conversion loss [dB]	NEP [pW/√Hz]	T_N [°K]	P_N [dBm]	Ref
ZB	0.3	-	2.0	-	-45	[21]
ZB	0.85	-	7.9	-	-36	[21]
SHM	0.3	6	-	1000	-79	[21]
SHM	0.85	15	-	10000	-69	[21]
QT	4.2	-	0.4	-	-49	[74]

These parameters will be used in the link budget analysis in Chapter 3 to determine not only the feasibility of THz retromodulation as a whole, but the specific feasibility of THz retromodulation using the various detector technologies.

2.1.3 Transmission Channel

The transmission channel over which the wireless THz communication link operates must also be considered due to the potentially significant losses induced primarily by atmospheric water vapour [76]. Water vapour possesses many rotational and vibrational modes with frequencies in the THz spectrum that couple to and absorb any passing THz signal. Therefore, any wireless THz communication link, regardless of whether the link is active or passive, should aim to avoid these frequencies. Figure 2.3 shows the water vapour absorption spectrum up to 1 THz, revealing major absorption peaks at 557 GHz, 752 GHz, and 988 GHz [77]. In the transmission windows between those peaks, channel power loss coefficients are below 100 dB/km (0.1 dB/m) [77] and are relatively constant over a wide bandwidth. Above 1 THz, absorption lines become more closely spaced and transmission windows are narrow making it difficult to deal with water vapour absorption. However, for links of just a few metres, high

channel power loss coefficients on the order of 1000 dB/km or 1 dB/m could be managed with sufficient transmitter power and detector sensitivity.

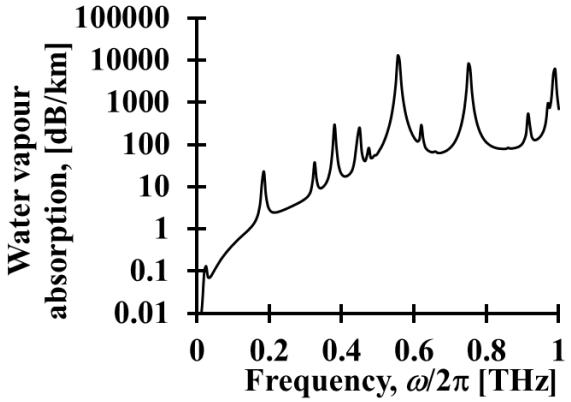

Figure 2.3: Atmospheric absorption due to water vapour is shown in dB/km up to 1 THz for a vapour density of 7.5 g/m^3 at 15°C. Data from "Recommendation ITU-R P.676-12 (08/2019)" [77].

2.2 Specific Considerations for Passive THz Uplinks

The following subsections are literature reviews for components of a passive uplink systems that are not used in active uplink systems. These components can be broadly divided into retroreflectors and modulators, with multiple implementations of each component. These components will be combined in Chapter 6 to form a full working retromodulator.

2.2.1 Retroreflectors

Retroreflectors make use of geometric optics to reverse the direction of incident light, so their structure is similar for all regions of the electromagnetic spectrum provided that ray-based analyses are valid. With the exception of a few studies [46], [47], [48], the literature is quiet when it comes to THz retroreflectors; however, there are many examples of retroreflectors for the optical spectrum [38], [39], [40], [41], [42], [78], [79]. In both cases, there are two main retroreflector architectures: the cornercube retroreflector [39], [41], [42], [46], and the spherical retroreflector [38], [40], [47], [78], [79]. Other retroreflector architectures have been presented [48] but have not seen the same widespread adoption.

2.2.1.1 Cornercube Retroreflectors

The cornercube retroreflector is the simplest retroreflector architecture, consisting of three reflective orthogonal planes which flip the vector components of an incoming light ray to return it along the path in which it arrived. Cornercube retroreflectors have been demonstrated for optical retromodulation [39], [41], [42] and for THz retroreflection [46]. Cornercube retroreflectors have two main benefits. First, they are simple to manufacture with the three planes of a cornercube being either triangular, as seen in Figure 2.4, or square. The second benefit is that the internal surfaces of the cornercube are typically coated with a highly reflective metal making it a virtually lossless reflector. Choosing a material for these internal surfaces is critical as incident light needs to reflect off all three internal surfaces before returning to its source. For visible light applications, silver is the material of choice since it has a high reflectivity (>99%) over most of the visible spectrum. For NIR and mid-IR, gold is the material of choice as it is highly reflective (>99%) over much of this spectrum. For the THz spectrum, gold is also the material of choice, though aluminium and silver are also highly reflective in the THz spectrum [80]. Consequently, gold is commonly used in experimental THz setups as a coating on parabolic mirrors. While THz retroreflection demonstrations using cornercube retroreflectors are quite uncommon, a few have shown up in the literature. In these demonstrations, a THz cornercube was used in atmospheric gas spectroscopy measurements to increase the propagation distance of a THz beam to hundreds of metres or more in outdoor environments [46], [81]. The cornercube was large, on the order of one metre, to both increase signal capture and to limit diffraction over the long propagation distances.

The main weakness of the cornercube retroreflector is its narrow angular field-of-view (FOV), which is limited to one eighth of a full sphere. Furthermore, the strength of the retroreflected signal decreases for glancing incident angles. Each incident angle can be defined by an incident azimuthal angle, ϕ, which is the angle rotated about the optical axis (OA), and an incident polar angle, θ, which is the angle down from the optical axis. These angles are denoted for a cornercube retroreflector in Figure 2.4.

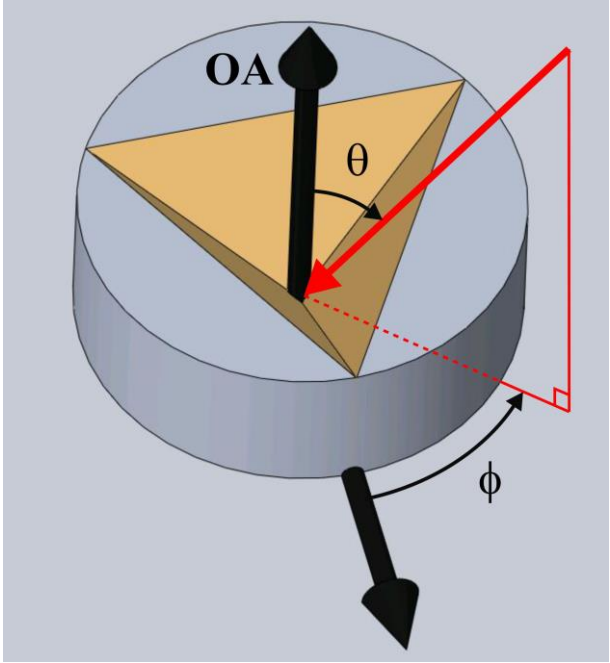

Figure 2.4: The experimental cornercube retroreflector that was fabricated is shown here. A coordinate frame is shown superimposed over the cornercube retroreflector as the thick black arrows, with the optical axis (OA) denoted. A representative incoming ray is shown as the red arrow with its incident azimuthal angle, ϕ, and incident polar angle, θ, denoted.

In addition, cornercube retroreflectors will introduce a certain level of beam divergence due to diffraction. A cornercube retroreflector diffracts any retroreflected beam since it acts as an aperture from which the retroreflected beam is transmitted. This effect is compounded by the fact that only the central region of the cornercube retroreflects the beam fully. The angle of divergence depends on the size of the cornercube retroreflector compared to the wavelength of the beam it is trying to retroreflect. Diffraction over short distances from a centimetre sized cornercube is typically not an issue for visible and NIR due to their micron or submicron wavelengths. Conversely, submillimetre THz wavelengths will be prone to diffraction from centimetre sized cornercube retroreflectors. Others have used metre sized cornercube retroreflectors to minimize diffraction for THz [46], [81]; however, a cornercube retroreflector of this size is not practical for handheld mobile transceivers. The diffraction losses from a cornercube retroreflector can be determined by modelling it as an aperture with an area equal to the cross-sectional area of the cornercube retroreflector, as was done in [82]. More generally, the far-field diffraction pattern of any aperture can be defined by the Fraunhofer diffraction equation [82], [83]. This equation applies when $R_{link} >> a^2/\lambda$, which is to say, when the diffracted wave propagates a long distance, R_{link}, compared to the aperture diameter, a, with respect

to the signal beam wavelength, λ. In a THz retromodulation system, with a cornercube retroreflector with a diameter on the order of one centimetre, a propagation distance of over one metre is required for this equation to hold. The divergence introduced by an aperture is related to the aperture's directivity, which is defined as the maximum power density of the diffraction pattern divided by the average power density of the diffraction pattern [43]. The calculated directivity can be related to the aperture divergence angle, θ_d, using $D = 4\pi / \theta_d^2$. The divergence angles of some common apertures have already been calculated [43]. Square apertures having a divergence angle of $\theta_d = \lambda / a$ and circular apertures having a divergence angle of $\theta_d = 1.22\lambda / a$, where a is the side length (square) or diameter (circle) of the aperture.

The question now becomes, what aperture shape does a cornercube impose on a retroreflected beam? There are several things to consider when answering this question. The first is that not all of the cornercube retroreflector will retroreflect incident energy. Only the central region of the retroreflector actually retroreflects, since energy incident on the edges of a cornercube may not reflect off all three surfaces, which is required for retroreflection. As such, the effective aperture area of the retroreflector is smaller than the overall diameter of the retroreflector. Second, as shown by Zhou *et al*., the aperture shape imposed by a cornercube is hexagonal for normal incidence [83]. For simplicity, a hexagonal aperture will be approximated by a square aperture in this work. While modelling the hexagonal aperture as a circular aperture would be more accurate, the error introduced by the square aperture approximation is minor. Finally, when the cornercube retroreflector is not under normal incidence, the effective aperture formed by the retroreflecting region of the cornercube becomes smaller and more irregular. This will induce additional, asymmetric divergence and some dimensions may become small faster than others. In general, it would be very challenging to derive a closed form expression for the divergence angle of an arbitrary cornercube orientation.

In summary, cornercube retroreflectors are viable for use in passive THz links. Gold coating the inner surfaces of the cornercube retroreflector allows for virtually perfect power reflection. The only design challenge is the diffraction introduced if the size of the cornercube retroreflector is on the order of the wavelength it is trying to

retroreflect. However, existing models can be used to predict the diffraction of light of an arbitrary wavelength off an arbitrarily sized cornercube.

2.2.1.2 Spherical Retroreflectors

The spherical retroreflector is a somewhat more complex alternative to the cornercube retroreflector, albeit with a superior angular FOV. From ray theory, a spherical retroreflector is a dielectric sphere that refracts collimated incident light at its front of the sphere, focusing this light on its back surface. Fresnel reflection off the back surface of the sphere returns some of the focused light to the front of the sphere where it is recollimated by the front surface. In order for this to happen, the sphere must have a refractive index, *n*, equal to two [78]. Additionally, if the back half of the sphere is coated with a reflective material, it has an angular FOV of a full hemisphere. Figure 2.5 shows a simple diagram of a spherical retroreflector.

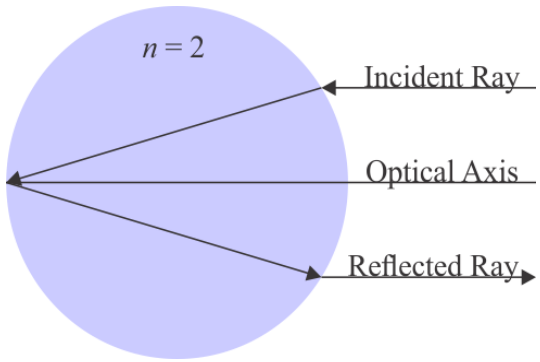

Figure 2.5: Light rays propagating through a spherical retroreflector is shown in this figure.

Like with cornercube retroreflectors, there are additional considerations for spherical retroreflectors when their size is on the order of the incident wavelength. As previously stated, when a spherical retroreflector is very large compared to the incident wavelength of the signal beam it is retroreflecting, the required refractive index can be determined, using a paraxial ray approximation, to be 2.0 [40], [44], [47], [78]. However, when the sphere diameter is on the order of the incident wavelength of the beam it is retroreflecting, a smaller refractive index must be used. This is especially important for passive THz links as centimeter sized spheres will be used to retroreflect wavelengths of up to 1 mm. Born *et al*. ran numerical simulations using Mie theory to determine the optimal refractive index for spherical retroreflectors with diameters that were on the order of the wavelength [44]. Applying

those results to THz spherical retroreflectors indicates that a centimetre sized sphere requires a refractive index of about 1.8 ± 0.1 depending upon the incident wavelength.

In addition to having the appropriate refractive index, efficient spherical retroreflectors necessitate the dielectric sphere be sufficiently transparent to the wavelengths it is retroreflecting, since power must pass through it twice. For visible and NIR wavelengths, a variety of materials exist with both the correct refractive index and low absorption making spherical retroreflectors commonplace [38], [40], [44], [78], [79], [84], [85]. Single material spherical retroreflectors made of custom grades of glass with a refractive index of exactly two, such as S-LAH79 [38], [40], [44] and TaFD44 [84], have been demonstrated. In, Jin *et al*., an S-LAH79 spherical retroreflector was used to retroreflect a 1550 nm beam with a beam divergence below 0.02° [40]. This low divergence was due to the large sphere size, 2.5 mm, compared to the communication signal wavelength, 1550 nm, and its ideal refractive index of two. Since making large spherical retroreflectors out of custom glass is costly, Luneburg lens spherical retroreflectors comprised of multiple layers of commonly available dielectrics have been demonstrated as a cheaper option [78], [79], [85]. Oakley *et al*. demonstrated a 7 cm diameter Luneburg lens spherical retroreflector that was fabricated out of several shells of common glasses such as BK7 [78]. Retroreflection of a 690 nm beam was determined to be theoretically detectable at 1.5 km. The advantage to using several layers of glass with dissimilar refractive indices is that spherical aberration can be compensated resulting in a higher retroreflected signal [78]. Kucharski *et al*. carried out laser ranging experiments on the BLITS (Ball Lens In The Space) Luneburg lens spherical retroreflector microsatellite orbiting at an altitude of 832 km. The Luneburg lens is 17 cm in diameter to ensure good collimation at low-orbital distances [79].

Unfortunately, the wealth of viable dielectric materials for use in visible and NIR spherical retroreflectors is of little use in the THz spectrum. This is because most conventional types of glass are highly absorptive for THz wavelengths [25], [32]. Consequently, entirely new materials need to be considered when fabricating spherical retroreflectors for the THz spectrum. These materials need to have a refractive index of about 1.8, as indicated by Born *et al.*, as well as very low power absorption. The literature shows that there are several classes of low-absorption materials in the THz spectrum. The first class of materials is polymers, though their refractive indices

typically range from 1.4 to 1.6 [27], [31], [32], [86]. The second class of materials is semiconductors, which typically have refractive indices above 3.0 and very low power absorption [30]. The final class is oxides, which have low power absorption in the THz spectrum and feature the widest range of refractive indices of any class. In particular, crystalline quartz is close to the ideal material with a refractive index of 2.05 and low power absorption. It has been used for a large spherical THz retroreflector [47]; however, this refractive index is too large for small-sphere applications. Table 2.3 shows the refractive index, $n(\omega)$, and power absorption coefficient, $\alpha(\omega)$ for a variety of polymers, semiconductors, and oxides. The polymers shown are high density polyethylene (HDPE), polydimethylsiloxane (PDMS), polystyrene (PS), polypropylene (PP), polytetrafluoroethylene, also known as Teflon (PTFE), and cyclic olefin copolymer (COC). The semiconductors shown are high-resistivity float zone silicon (HRFZ Si), gallium arsenide (GaAs), and germanium (Ge). The oxide materials shown in the table are silicon dioxide (Quartz and Fused Silica), aluminum oxide (Sapphire), and titanium dioxide (TiO_2). It appears that no materials with both low power absorption, defined as $\alpha(\omega) < 1$ cm^{-1}, and a refractive index of around 1.8 exist in the THz spectrum. However, there is an alternative solution to creating a material with the correct refractive index: composite materials. By combining a low refractive index polymer with a high refractive index oxide or semiconductor, a composite material can be created with a tunable refractive index. The low refractive index material is called the host and can either be in the form of a liquid or of solid particles during fabrication. Any high refractive index material is typically made of solid particles that are suspended in the host, and so will be referred to as the particles. The exact refractive index can be designed by varying the volumetric fraction of each component in the composite. Many groups have reported tunable refractive index polymer composites for the THz spectrum using this method [19], [20], [28], [33], [87], [88], [89], [90], [91], [92], [93], [94]. The polymer filler is typically polydimethylsiloxane [90], high-density polyethylene [19], [87], [89], polypropylene [19], [20], [28], [33], [93], or polystyrene [91]. Typical high-index particles include silicon [28], [88], [89], silicon dioxide [28], titanium dioxide [87], [91], [92], [93], and others [19], [20], [28], [33], [90], [93], [94].

Table 2.3: Refractive indices and power absorption coefficients for various materials at THz frequencies

Material	n(300 GHz – 1 THz)	α(300 GHz) [cm^{-1}]	α(1 THz) [cm^{-1}]	Ref
HDPE	1.53	0.05	0.1	[129]
PDMS	1.57 – 1.65	3	8-10	[27]
PS	1.6	0.5	1.7	[31]
PTFE	1.43	0.38	1.3	[31]
PP	1.51	<0.5	1	[20]
COC	1.52	<0.4	<0.4	[128]
HRFZ Si	3.42	0.02	0.04	[30]
GaAs	3.6	0.2	0.5	[30]
Ge	4.0	2	0.7	[30]
Quartz	2.1	0.02	0.05	[30]
Fused Silica	1.96	0.02	2	[30]
Sapphire	3.07	0.02	1	[30]
TiO_2	9.6 – 9.9	6	104	[140]

A variety of effective medium theories have been applied to understand the refraction and absorption characteristics of THz composite materials [93], [95], [96], [97]. These theories are founded upon models whose assumptions largely dictate the extent of their validity. The simplest model is the Maxwell-Garnett model, which assumes that the particles make up only a small volumetric fraction of the composite and that these particles are both spherical and much smaller than the wavelength of the incident radiation. Thus, the model is particularly effective in characterizing composites with low concentrations of small spherical particles [93]. For small volumetric fractions of aspherical particles, the Landau-Lifshitz-Looyenga model is sometimes employed. This model makes no assumption of particle geometry allowing it to describe composites containing any shape of particle; however, it is limited to low volumetric fractions due to a Taylor series approximation in its derivation [93]. The two previously mentioned effective medium theories are inadequate for the composite materials used in a spherical THz retroreflector, since these composites may need to have large volumetric fractions as no pure material exists with a refractive index near 1.8. Other effective medium theories exist that can model composites with higher volumetric fractions. The Polder van Santen model is one of these that considers ellipsoidal particles over a wide range of volumetric fractions. The particles are quantified using a depolarization factor, which can be calculated for various aspect ratios of ellipsoidal particles. However, this model is limited to ellipsoidal particles and cannot describe particles with arbitrary geometries [93], [97]. The final effective medium theory is the Bruggeman model, which is

an extension of the Maxwell-Garnett model that allows for any volumetric fraction of particles. This lets the Bruggeman model characterize a wider array of composites [89], [93], [95], [98], although it maintains the assumption that the particles are much smaller than the incident wavelength. Like the Polder van Santen model, the Bruggeman model considers the depolarization factor of the particles, though by leaving the depolarization factor as a fitting parameter, composites containing particles of arbitrary geometries can be modelled. In fact, the Polder van Santen model degenerates into the Bruggeman model for spherical particles [99], though this does not hold for particles with arbitrary geometries.

The Bruggeman model is a foundational effective medium theory for studies of composites within the THz spectrum [89], [93], [95], [96], [98] and will be the exclusive model used in this thesis. The Bruggeman model quantifies the refraction and absorption characteristics of a composite, with a volumetric fraction of V, using [96]

$$(1-V)\frac{\tilde{\varepsilon}_{\mathrm{h}}(\omega)-\tilde{\varepsilon}_{\mathrm{c}}(\omega)}{N_{\mathrm{d}}\tilde{\varepsilon}_{\mathrm{h}}(\omega)+(1-N_{\mathrm{d}})\tilde{\varepsilon}_{\mathrm{c}}(\omega)}+V\frac{\tilde{\varepsilon}_{\mathrm{p}}(\omega)-\tilde{\varepsilon}_{\mathrm{c}}(\omega)}{N_{\mathrm{d}}\tilde{\varepsilon}_{\mathrm{p}}(\omega)+(1-N_{\mathrm{d}})\tilde{\varepsilon}_{\mathrm{c}}(\omega)}=0, \tag{2.1}$$

where $\tilde{\varepsilon}_{\mathrm{h}}(\omega)$, $\tilde{\varepsilon}_{\mathrm{p}}(\omega)$, and $\tilde{\varepsilon}_{\mathrm{c}}(\omega)$ are the complex dielectric constants of the host, particles, and overall composite, respectively, and ω is the angular frequency of the incident THz radiation. The depolarization factor, N_{d}, appears in this equation to generalize the Bruggeman model and its description of dielectric polarization to particles of arbitrary shape. It does so by characterizing the distribution of bound charges on the particles' surfaces and the depolarization field that such charges form in opposition to the applied electric field. It is possible to numerically determine the depolarization factor for a few simple particle geometries. Spherical particles have a depolarization factor of $N_{\mathrm{d}} = 1/3$ [89], [95]. Ellipsoidal particles have three different depolarization factors, one for each Cartesian axis. These depolarization factor values range between $N_{\mathrm{d}} = 0$ and $N_{\mathrm{d}} = 1$ [97], [100] depending on the ellipsoid geometry. If the ellipsoidal particles are aligned to a particular axis, a single depolarization factor can be quoted. However, if the ellipsoidal particles are randomly oriented, a weighted average of depolarization factors is used to determine the overall depolarization factor. This weighted average considers the polarizability along each Cartesian axis and thus is dependent on the dielectric constants of the host and particles. It is interesting to note that the overall

depolarization factor values for randomly oriented ellipsoidal particles range between $N_d = 0$ and $N_d = 1/3$ [100]. Ultimately, (2.1) is manipulated to give an explicit expression for $\tilde{\varepsilon}_c(\omega)$, which is used to determine the real valued refractive index, $n(\omega)$, and extinction coefficient, $\kappa(\omega)$, of the composite using $\sqrt{\tilde{\varepsilon}_c(\omega)} = n(\omega) - j\kappa(\omega)$. However, as will be seen in Section 4.2.1, the Bruggeman model with ellipsoidal particles cannot describe the measured dielectric constant of composite materials made of particles with arbitrary geometries. Therefore, modelling particles of arbitrary geometries with ellipsoids is inadequate and the overall depolarization factor of the particles must simply be left as a fitting parameter.

One final consideration when fabricating composite materials in the THz spectrum is particle size. The Bruggeman model assumes that all particles are infinitely small, so not scattering effects are seen in the dielectric constant. This is untrue in practice as the finite size of the particles will introduce scattering losses, which has been observed for composites in the THz spectrum [95]. However, scattering losses are minimal so long as the particle diameter is much smaller than the wavelength. As will be seen in Section 4.2, the composites used in this work all have particle diameters that are well below $\lambda/10$; therefore, scattering losses will be minimal. Additionally, other sources of loss in the fabricated THz composites dwarf any potential scattering losses. Therefore, scattering loss will not be discussed further in this thesis.

In summary, spherical retroreflectors can be used in a passive THz link provided judicious selection of the dielectric material used to make the spheres. Pure conventional materials do not have the required properties to make an effective spherical retroreflector in the THz spectrum, so composite materials will be considered instead. The literature shows that creating a composite material with the correct refractive index is viable using a polymer host with either semiconductor or oxide particles. The Bruggeman model can be used to determine the correct volumetric fraction of each material to create a composite with the desired refractive index.

2.2.2 Free Space Modulators

Retromodulation demands the use of free-space modulators to ensure that retroreflection is not disrupted by the modulator. While data rates above 1 Gbps have been demonstrated in fibre-coupled systems [101], [102], these systems are incompatible with free-space operation, and therefore cannot be used for passive THz links. However, there has been significant effort invested in free-space THz modulators over the past decade [49], [50], [51], [52], [53], [54], [55], [56]. Free-space THz modulator designs can be broadly separated into two categories, electrical modulators, and optical modulators, both of which exist for the optical, NIR, and THz spectra. Optical modulators are based on an incident optical beam exciting a charge carrier density in a semiconductor substrate [38], [41], [44], [49], [50], [51], [52], [103] inducing modulation either directly through free carrier absorption or by shifting the resonant frequency of a frequency-selective surface. Electrical modulators are based on shifting the resonant frequency of a frequency-selective surface by using a potential to move charge carriers around [9], [53], [54], [55], [56], [104], [105], [106], [107], [108] as opposed to generating them as is done in optical modulators. Ultimately, electrical modulators are more practical for THz modulation as they require only a few volts to carry out switching and have been shown to operate at speeds of up to 1 GHz [53]; however, they are more complicated to fabricate. Other modulators based on polarization rotation [109], liquid crystals [39], [45], and mechanical modulation [82], [83], [110], have been demonstrated for certain spectra. Unfortunately, many of these other methods are limited to kilohertz switching speeds [39], [45], [82], [83], [110] and have not seen widespread adoption.

2.2.2.1 Optical Modulators

Free-space optical modulators for THz are based either on free carrier absorption [50], [51], [52] or shifting a frequency-selective surface resonance [49], [111], [112]. Free carrier absorption can be modelled using the Drude model, which can be used to relate free carrier density to refractive index and extinction coefficient [50], [51], [52]. Large free carrier densities are photogenerated by an optical source, typically a laser, to bring about both amplitude and phase modulation. The magnitude of the free carrier density is proportional to the optical generation rate of carriers and the charge carrier lifetime. For high-speed modulators, the charge carrier lifetime must be short, however this reduces the magnitude of the free carrier density and thus modulation depth, which will be referred to

as modulation efficiency in this thesis. As a result, there are three distinct methods of implementing optical THz modulators. The first method, which aims to induce appreciable modulation using a pulsed laser to generate extremely high optical intensity on short lifetime semiconductors, is called optical pump THz probe (OPTP). Using this method, Strait *et al*. measured the ultrafast charge-carrier dynamics of Ge nanowires [113]. It was found that these nanowires have an optically induced charge-carrier lifetime of 100 ps, corresponding to a modulation rate of 10 GHz. An all-optical graphene modulator was tested using OPTP by George *et al*. Graphene was shown to have a charge-carrier lifetime of about 5 ps, which would suggest remarkable modulation rates above 100 GHz [114]. The disadvantage to using the materials from OPTP studies as modulators is their requirement for the ultra-high charge-carrier densities delivered by a pulsed laser. While this gives impressive modulation rates, which can be extracted from charge-carrier lifetimes, it ignores the fact that generating these ultra-high charge-carrier densities is impractical for the CW lasers needed to encode bits onto a THz signal. The second method takes the opposite approach by inducing appreciable modulation using modest optical intensities from a CW laser in long lifetime semiconductors. Recently, optical modulators based on graphene on Si [52] and graphene on Ge [51] have been demonstrated. One modulator, which featured graphene on Si, was capable of a modulation efficiency of 50% with 50 mW of optical pump power at 780 nm and a maximum modulation efficiency of 99% at a 500 mW of pump power [52]. This is due to the long charge-carrier lifetime of the intrinsic Si used in the study and is likely the reason that no modulation rate was given by the authors. Another modulator, based on graphene on Ge, achieved a modulation efficiency of 40% at 200 mW and 90% at 800 mW of 1550 nm pump laser power [51]. The 200 mW pump laser was used to modulate a 340 GHz CW THz source at up to 200 kHz. This maximum modulation rate was limited by the charge-carrier lifetime of the Ge substrate. The third and final optical modulation method is to use the optically induced charge carrier density to modify the resonant frequency of a frequency-selective surface coupled to the passing THz wave [49], [111], [112] similar to electronic modulators. These optically switched frequency-selective surfaces have the advantage that smaller charge carrier densities can induce higher modulation efficiencies due to coupling between the THz wave and the frequency-selective surface, although they only operate over a limited bandwidth.

The modulation induced by the first two methods mentioned previously is based on free carrier absorption, which can be simply described by the Drude model. A basic summary of the Drude model will be given here, although some slight modifications will be given as required in later chapters and a more detailed derivation can be found in Appendix A. The dielectric constant of a semiconductor material depends on its intrinsic dielectric constant, $\tilde{\varepsilon}_{\mathrm{i}}(\omega)$, plus perturbations induced by the existence of free carriers. Note that these carriers do not need to be optically induced, this model equally applies to extrinsically doped semiconductors as well. The Drude model states that the perturbed dielectric constant, $\tilde{\varepsilon}(\omega,t)$, can be modelled using the complex electrical susceptibility for both electrons, $\chi_{\mathrm{e}}(\omega,t)$, and holes, $\chi_{\mathrm{h}}(\omega,t)$ using

$$\tilde{\varepsilon}(\omega,t) = \tilde{\varepsilon}_{\mathrm{i}}(\omega) + (\,\tilde{\chi}_{\mathrm{e}}(\omega,t) + \tilde{\chi}_{\mathrm{h}}(\omega,t)\,)\,. \tag{2.2}$$

Note that the charge carrier induced susceptibility is a function of time, *t*, which allows for modulation. The intrinsic dielectric constant can be defined in terms of the intrinsic refractive index, $n(\omega)$, and extinction coefficient, $\kappa(\omega)$, using $\sqrt{\tilde{\varepsilon}_{\mathrm{i}}(\omega)} = n(\omega) - j\kappa(\omega)$. Note that both electrical susceptibilities can be functions of time, and so the perturbed dielectric constant must also be a function of time. While the intrinsic dielectric constant of a semiconductor is time independent, it along with the rest of the terms in (2.2) are functions of THz frequency, ω. The perturbed dielectric constant can be related to changes in the refractive index, $\Delta n(\omega,t)$, and extinction coefficient, $\Delta\kappa(\omega,t)$ using

$$\sqrt{\tilde{\varepsilon}(\omega,t)} = \sqrt{\tilde{\varepsilon}_{\mathrm{i}}(\omega)} + \Delta n(\omega,t) - \mathrm{j}\Delta\kappa(\omega,t)\ . \tag{2.3}$$

The time varying susceptibilities for electrons and holes are derived by assuming that free carriers move through the semiconductor in the presence of an applied electric field and only lose energy when they interact with nuclei or other carriers. This creates a classical dynamics equation with momentum and damping, which can be solved to give the motion of the carriers. Since the applied field oscillates in time, so do the electrons. The oscillating electrons create a polarization density, which can be related to electrical susceptibility. The equations for susceptibility of both electrons and holes are

$$\tilde{\chi}_{\mathrm{e}}(\omega,t)=\frac{-q^2N(t)}{\varepsilon_0 m_{\mathrm{e}}^{*}\omega(\omega+\mathrm{j}(1/\tau_{\mathrm{s,e}}))} \tag{2.4a}$$

and

$$\tilde{\chi}_{\mathrm{h}}(\omega,t)=\frac{-q^2N(t)}{\varepsilon_0 m_{\mathrm{h}}^{*}\omega(\omega+\mathrm{j}(1/\tau_{\mathrm{s,h}}))}\,. \tag{2.4b}$$

In these equations, q is the elementary charge, ε_0 is the permittivity of free space, j is the imaginary unit, m_{e}^{*} and m_{h}^{*} are the effective masses of electrons and holes, respectively, while $\tau_{\mathrm{s,e}}$ and $\tau_{\mathrm{s,h}}$ are the scatter times of electrons and holes, respectively. The final term in (2.4a) and (2.4b) is the time dependent charge carrier density, $N(t)$. This is proportional to the time varying intensity of the optical beam on the modulator and is what defines the modulation signal. Modulation efficiency in an optical modulator is largely dictated by the extinction coefficient and will be discussed in Chapter 3.

2.2.2.2 Electronic Modulators

Free-space electrical modulators for THz are more prevalent in the literature due to their practicality. Most free-space electrical modulators are based on shifting the resonance frequency of a frequency-selective surface by using a voltage to alter the charge carrier density of the substrate just below the surface of the modulator [53], [54], [55], [56], [106], [115], [116]. The frequency-selective surface is typically an antenna array, either dipole [53], [54] or split ring [55], [56], with specifically designed frequency characteristics. Many early devices were based on a semiconductor substrate that had been doped with extra electrons near the surface [54], [56]. These devices were capable of operating at modulation rates of up to 100 kHz [54] but were limited by the capacitance between the metal on the frequency-selective surface and the substrate. To enhance modulation rate, newer electronic modulators place transistors, such as high electron mobility transistors, in the gaps between the antennas of the frequency-selective surface [53], [55]. This reduces the device capacitance significantly, since only the gates need to be charged as opposed to the entire antenna array, and modulation rates of up to 1 GHz have been demonstrated [53]. It should be noted that all electronic modulators are inherently are more narrow-band than optical modulators

based on free carrier absorption, with bandwidths of a few hundred gigahertz or less [54], [55]. Table 2.4 shows the operating frequency, bandwidth, modulation rate, drive voltage, and polarization sensitivity for a number of electronic modulators found in the literature. Modulation rates in the table were quoted for 50% modulation efficiencies to allow all modulators to be fairly compared, though many modulators still induced an appreciable modulation efficiency for higher modulation rates.

Table 2.4: Summary of various electrical modulators from the literature

Frequency (GHz)	Carrier bandwidth (GHz)	Modulation rate (MHz)	Drive voltage (V)	Polarization Sensitive	Ref
850	150	2.75	-4	No	[55]
630	150	0.08	15	No	[54]
350	50	150	4.5	Yes	[53]
1000	250	<0.01	16	Partial	[56]
700	N/A	0.1	-12	Partial	[106]

It appears from the devices outlined in Table 2.4 that electronic modulators are designed for one or two specific parameters. The one designed for the highest modulation rate suffers from polarization sensitivity, and those that were designed for modulation over a broad bandwidth suffer from low modulation rates. In addition, modulators based on surface doping require a much higher drive voltage than those with transistors integrated into the frequency-selective surface. In summary, electrical modulator are capable of polarization insensitive modulation of THz wavelengths at high modulation rates [55]. However, electrical modulators require microfabrication techniques that are complex to implement, and so were not considered for fabrication in this thesis.

2.3 Review of Retromodulators

Now that retroreflectors and modulators have been reviewed separately, this section will review the merging of both components into a retromodulator. To understand how this might be accomplished, guidance will be taken from existing retromodulator architectures for the visible [39], [82], [83], [110] and NIR [38], [40], [41], [44] spectrum. The literature shows that retromodulators can be broken down into two primary architectures: shutter retromodulators and integrated retromodulators.

The simplest and most prevalent retromodulator architecture is the shutter architecture [39], [45]. In this architecture, the retroreflector and modulator are spatially separated. An incoming signal beam first passes through the modulator before arriving at the retroreflector, then passes through the modulator again on the return trip. This architecture can be used for both cornercube retroreflectors and spherical retroreflectors with equal effectiveness. The shutter architecture also lends itself well to modulators based on Drude free carrier absorption operating in transmission, since transmission through the modulator allows for attenuation due to an increased extinction coefficient. In addition, the retroreflected signal must pass through the modulator twice, increasing modulation efficiency. The shutter architecture has typically been implemented for the visible and NIR spectra with LCD shutters due to their simplicity [39], [45]. One of the earliest retromodulation demonstrations was in 1997 when Swenson *et al*. implemented a retromodulation system sending phase modulated data over 30 km at 1.2 kbit/s using a cornercube retroreflector and LCD shutter [39]. In a more recent demonstration of the shutter architecture, Collier *et al*. designed a retromodulation system operating at 150 Hz with several cornercube retroreflectors placed at different angles to increase the field-of-view of the retromodulator [45]. While the shutter architecture is the simplest conceptually, other retromodulators may be equally viable and easier to implement for the THz spectrum.

Integrated retromodulator designs are typically more elegant and compact; however, they come at the cost of design complexity. For cornercube retroreflectors, mechanical modulators can be built into the cornercube retroreflector to physically move one or more of the internal surfaces to modulate retroreflected signal power [82], [83], [110]. However, to avoid diffraction, THz cornercube retroreflectors will need to be much larger than cornercube retroreflectors for visible and NIR data signals. Increasing cornercube retroreflector dimensions makes mechanical modulation much more difficult due to the added mass of the sides that need to be moved. Consequently, this method is impractical for THz retromodulation. Integrating a Drude free carrier absorption-based modulator into a cornercube retroreflector by making the cornercube retroreflector surfaces into modulators is one possibility that has yet to be seen in the literature. Drude free carrier absorption could be used to modulate the refractive index of the internal surfaces thereby modulating surface reflectivity. For spherical retroreflectors, the intense focus created on the back surface of the sphere has been shown to enhance Drude free carrier absorption in a semiconductor

material coated to the back of the sphere [38], [40], [44]. Since the signal beam is focused down to a small area, a charge-carrier plasma only needs to exist in that small area. This allows the charge-carrier density to be higher, inducing a higher modulation efficiency. Another option, which has not been demonstrated in the literature, would be to make an entire retroreflecting sphere out of a material that can be modulated. This could be accomplished using polymer composites with high-resistivity semiconductor particles. By applying a separate pump beam to the sphere, Drude free carrier absorption in the semiconductor particles would increase absorption of the signal beam in the sphere. This method would require the filler polymer to be transparent to the pump beam.

In summary, both shutter and integrated retromodulator architectures are viable for optical retromodulation and so their migration to the THz spectrum should be considered. The literature seems to favour the shutter method, as it allows designers to optimize both the retroreflector and modulator separately. Still, an integrated architecture may be worth pursuing as it allows for more elegant designs and has the potential to be more compact.

Chapter 3: Link Budget Analysis

Every device in a wireless communication system must be able to transmit enough energy to be received by other devices in the network. This is commonly referred to as closing the link. The primary analysis used to determine if communication links can be closed is called a link budget analysis. A link budget analysis looks at the power radiated by a transmitter and determines the signal intensity at an arbitrary point in space, typically far from the transmitter. The intensity at this point is affected by the link length, since energy diverges from the transmitter, and propagation loss, which will mostly be atmospheric absorption for wireless THz communication links. This chapter will carry out link budget analyses for both active and passive THz links. In general, active THz links will always provide superior detected signal power; however, with the proper design, passive THz links can approach the performance of active THz links in certain scenarios. For active THz links, the standard Friis transmission equation will be used to model the data link [43]. For passive THz links, the Friis transmission equation will be used to derive a retromodulation equation, which is similar in form to the radar range equation. These equations will be populated using data for transmitters, detectors, and channel loss given in Chapter 2. The retromodulation equation for passive uplinks will also be populated with modulation efficiencies, retroreflection efficiencies, and insertion efficiencies from systems mentioned in the previous chapter. The link budget results for active and passive uplinks will be contrasted at the end of this chapter and the most feasible scenarios for THz retromodulation will be identified.

3.1 Active THz Uplinks

Active THz uplinks are relatively easy to model as they can simply use the Friis transmission equation between the transmitter and detector. The Friis transmission equation can be cast in the form

$$P_{\mathrm{d}}(\omega) = \frac{P_{\mathrm{t}}(\omega) D_{\mathrm{t}}(\omega) D_{\mathrm{d}}(\omega) c^2 \exp(-\alpha_{\mathrm{ch}}(\omega) R_{\mathrm{link}})}{(2\omega R_{\mathrm{link}})^2}, \tag{3.1}$$

where $P_{\mathrm{d}}(\omega)$ is the power arriving at the detector, $P_{\mathrm{t}}(\omega)$ is the power radiated from the transmitter, D_{t} is the transmitter directivity, $D_{\mathrm{d}}(\omega)$ is the detector directivity, $\alpha_{\mathrm{ch}}(\omega)$ is the channel power loss (i.e., absorption) coefficient, ω is the angular frequency of the transmitted wave, and R_{link} is the link length [43]. Note that this

equation is able to give detected power as it takes into account the detector directivity, which is related to the detector area. This is the form of Friis transmission equation that will be used to analyse active THz links.

3.2 Passive THz Uplinks

The retromodulation equation for passive THz links requires applying the Friis transmission equation twice, once for propagation from the fixed transceiver to the mobile transceiver containing the retromodulator and once for propagation from this mobile transceiver back to the fixed transceiver. Propagation from the fixed transceiver to the mobile transceiver can be modelled using the Friis transmission equation in (3.1) for active THz links while replacing the directivity of the detector, $D_{\mathrm{d}}(\omega)$, with the directivity of the retromodulator, $D_{\mathrm{r}}(\omega)$. Now the power at the retromodulator, $P_{\mathrm{r}}(\omega)$, is

$$P_{\mathrm{r}}(\omega) = \frac{P_{\mathrm{t}}(\omega) D_{\mathrm{t}}(\omega) D_{\mathrm{r}}(\omega) c^2 \exp(-\alpha_{\mathrm{ch}}(\omega) R_{\mathrm{link}})}{(2\omega R_{\mathrm{link}})^2}. \tag{3.2a}$$

Propagation from the mobile transceiver containing the retromodulator back to the fixed transceiver can be modelled by an analogous equation,

$$P_{\mathrm{d}}(\omega) = \frac{P_{\mathrm{r}}(\omega) D_{\mathrm{r}}(\omega) D_{\mathrm{d}}(\omega) c^2 \exp(-\alpha_{\mathrm{ch}}(\omega) R_{\mathrm{link}})}{(2\omega R_{\mathrm{link}})^2}. \tag{3.2b}$$

Inserting (3.2a) into (3.2b) provides the link budget for a complete passive THz link,

$$P_{\mathrm{d}}(\omega) = \frac{P_{\mathrm{t}}(\omega) D_{\mathrm{t}}(\omega) D_{\mathrm{r}}(\omega)^2 D_{\mathrm{d}}(\omega) c^4 \exp(-2\alpha_{\mathrm{ch}}(\omega) R_{\mathrm{link}})}{(2\omega R_{\mathrm{link}})^4}. \tag{3.3}$$

The directivities in the previous equation can be approximated by a square aperture of side length a_i and THz wavelength λ as was shown in Section 2.2.1.1. These directivities are $D_i(\lambda)=4\pi/\theta_{\mathrm{d}}^2(\lambda)=4\pi a_i^2/\lambda^2$, which can be written in terms of aperture area A_i and THz frequency ω, $D_i(\omega)=A_i\omega^2/\pi c^2$, where i = t, r, and d denotes the transmitter, retromodulator, and detector, respectively. A circular aperture with an equivalent area will have about a 9% higher directivity due to a slightly lower divergence angle. Equation (3.3) will be referred to as the ideal retromodulation equation because it assumes perfect retroreflection, 100% modulation efficiency, and no other

losses associated with the retromodulator. In reality, this is unrealistic. A more practical retromodulation equation should include retroreflection efficiency, $\eta_{re}(\omega)$, incident angle efficiency, η_{IA}, modulation efficiency, $\eta_{mod}(\omega)$, and insertion efficiency for the modulator, $\eta_{in}(\omega)$. Note that insertion efficiency is the inverse of the more common insertion loss and the modulation efficiency is equivalent to modulation depth in many cases. In general, the real retromodulation equation, including nonidealities of the retromodulator, is

$$P_d(\omega) = \frac{P_t(\omega)D_t(\omega)D_r(\omega)^2 D_d(\omega)\eta_{IA}\eta_{mod}(\omega)\eta_{re}(\omega)\eta_{in}(\omega)c^4 \exp(-2\alpha_{ch}(\omega)R_{link})}{(2\omega R_{link})^4}. \quad (3.4)$$

All the terms describing the various non-idealities in (3.4) are set to one in the ideal retromodulation equation. One point to remember is that the expression $D_r(\omega)D_t(\omega)c^2/(2\omega R_{link})^2$ cannot be greater than one, as this would indicate that more power is arriving at the mobile transceiver than is being transmitted by the fixed transceiver. Likewise, the ratio $D_d(\omega)D_r(\omega)c^2/(2\omega R_{link})^2$ must also be less than one; otherwise, more power would arrive at the fixed transceiver than was retroreflected by the mobile transceiver. This is a result of the assumption in the Friis transmission equation that any beam incident on a device is larger than that device's aperture. The link budgets for active THz links, (3.1), ideal passive THz links, (3.3), and real passive THz links, (3.4), will now be populated and compared.

3.2.1 Link Budget Comparison

There are a few obvious differences between the link budget equation for active THz links in (3.1) and the retromodulation equations for passive THz links in (3.3) and (3.4). The most obvious difference is the path loss, which is $(c/2\omega R_{link})^2$ for active THz links and $(c/2\omega R_{link})^4$ for passive THz links. Consequently, path loss increases with link length much faster for passive THz links, limiting their long-range usefulness. It is also tempting to conclude that path loss increases for higher THz frequencies, making them impractical, though this is false. While path loss does increase for higher THz frequencies, the directivity of any device with a fixed aperture size also increases. The net result is an improvement in detected power for the passive THz links at higher frequencies and no frequency dependence in the detected power for active THz links. The second obvious difference is the inclusion

of retromodulator directivity squared in both passive THz link equations. This occurs because the retromodulator effectively acts twice on the propagating signal: once as a detector, and once as a transmitter. As a result, improving retromodulator directivity (i.e., increasing retromodulator aperture area) greatly improves the system performance of passive THz links. Finally, constraints on maximum transmitter and retromodulator directivity mean that, at best, passive THz links will match the detected power of active THz links. As will be seen later though, real passive THz links typically have much lower detected power than active THz links. This introduces a trade-off between the complexity of generating the additional transmitter power required to close the link for a passive THz link over an active THz link and the complexity of adding a THz transmitter to mobile transceivers. The remainder of this chapter will focus on populating the link budgets for the active THz link and both passive THz links, then comparing the results.

3.3 Ideal Retromodulation Analysis

To begin, the Friis transmission equation for active uplinks and the ideal retromodulation equation for ideal passive uplinks will be populated. This initial analysis will answer two questions: how much weaker is an ideal passive uplink in comparison to an active uplink, and can an ideal passive uplink close the link over useful distances? For the purpose of the analyses in this thesis, a useful distance is defined as a link length of five metres, which is suitable for many indoor settings. The analysis will be broken down into a number of systems, each containing a different transmitter technology, frequency, and transmitted power level. A summary of these systems was given in Table 2.1. For all systems, transmitter directivity is set to two, which simulates a wall or ceiling mounted transmitter broadcasting over a hemisphere. Each system will have link budgets calculated for the following scenarios: an active THz link with a 2 cm diameter detecting aperture (AL 2 cm), an active THz link with a 3 cm diameter detecting aperture (AL 3 cm), an ideal passive THz link with a 2 cm diameter retromodulator (IPL 2 cm), and an ideal passive THz link with a 3 cm diameter retromodulator (IPL 3 cm). Detector and retromodulator aperture diameters of two and three centimetres were chosen as they are on the large end of reasonable for mobile devices. All passive THz links have a 10 cm diameter detector aperture apart from system 7. This large detecting aperture was chosen to mitigate the additional losses of the passive THz links, though it may result in phase interference effects due to the

rest of the system not being in the far-field of the detector. This can be alleviated by decreasing the detector aperture diameter to 4 cm (at an 8 dB penalty), which would place the entire system in the far-field of the detector. System 7 is the only one with a smaller detector aperture diameter of 2 cm or 3 cm, matching the corresponding to the retromodulator diameter. This is required since a 10 cm diameter aperture would be larger than the returning signal beam due to the minimal divergence introduced by the high frequency of this system. Table 3.1 gives a summary of the aperture diameters for the various links.

Table 3.1: Summary of aperture diameters and directivities used in the link budget analysis

System	D_t [dB]	Active link detector aperture diameter [cm]	Passive link aperture diameter [cm]	Retromodulator diameter [cm]
1-6	3	2 or 3	10	2 or 3
7	3	2 or 3	2 or 3	2 or 3

Figure 3.1 shows the results of these link budgets along with the noise floors for both zero-bias (ZB) and subharmonic mixing (SHM) Schottky detectors as well as quantum transition detectors with a bandwidth of 1 GHz based on the numbers given by Virginia Diodes [21] and Li *et al*. [74]. Note that the quantum transition detector used with system 7 was designed for use at 4.2 THz [74], since no detector at 3.1 THz was available in the literature.

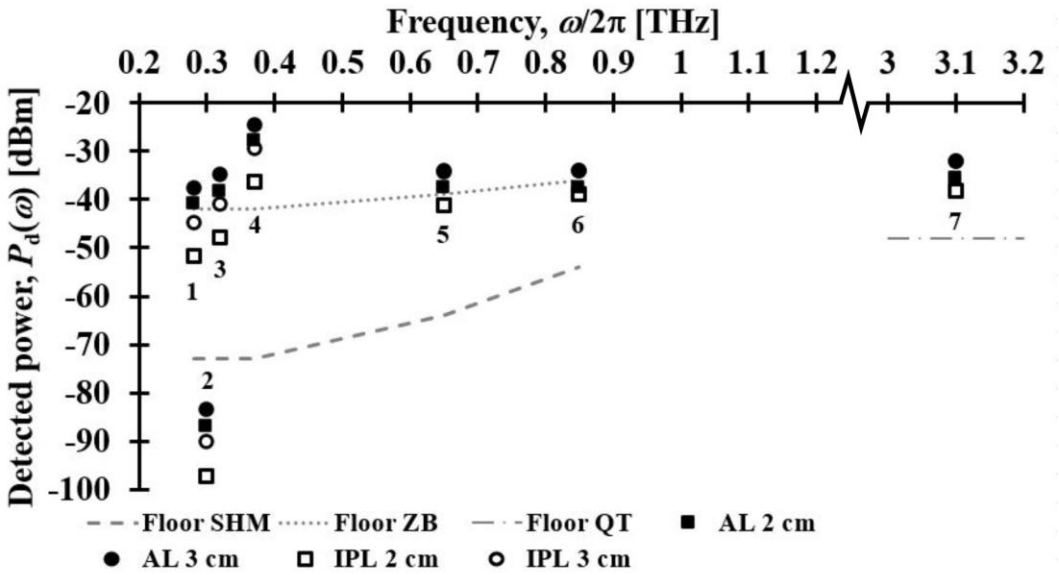

Figure 3.1: The link budget results for the seven different wireless THz communication links are shown along with noise floors for subharmonic mixing (SHM), zero-bias (ZB), and quantum transition (QT) detectors. The parameters for each of these systems were given in Table 2.1. Each system has four link budgets, two for active THz links (AL), and two for ideal passive THz links (IPL). The active THz links have results for a 2 cm and 3 cm detecting aperture, whereas the ideal passive THz links have results for 2 cm and 3 cm retromodulators. All ideal passive THz links assume a 10 cm detector aperture except system 7, which has identical retromodulator and detector aperture diameters.

In Figure 3.1, it is apparent that the various transmitter technologies were the single biggest factor in the performance of each system. The high-frequency electronic transmitters in systems 1 and 3 have a signal-to-noise ratio (SNR) of 20 dB and 30 dB for ideal passive and active THz links, respectively, with a subharmonic mixing detector. In all systems, SNR is the ratio to detected power to noise power. Given the commercial availability of both transmitters and detectors, these systems are a viable option for passive THz links. However, the same cannot be said for system 2, based on optical heterodyning. The SNR for active THz links is -10 dB using subharmonic mixing detectors, with ideal passive THz links being even worse off. This is unfortunate since optical heterodyning shows the greatest potential for high-bandwidth wireless THz communication links. However, the low transmitted power eliminates any possibility of using optical heterodyning transmitters in wide area passive THz links. The THz QCLs in system 7 perform admirably despite the larger path and channel losses at 3.1 THz. A minimum SNR of 10 dB is achieved for a 2 cm diameter ideal passive THz link, corresponding closely to the active THz link. However, the cost of implementing a cryogenically cooled QCL and quantum transition detector make this system an impractical candidate for passive THz links. The BWO in system 4 produces a significant amount of power, and therefore can be used with either zero-bias or subharmonic mixing detectors for all but the smaller retroreflector. While its beam quality is unknown and may be unsuitable for wireless THz communication link, BWOs are intriguing as the highest power option for passive THz links. Finally, two theoretical cases were considered at 650 GHz, system 5, and 850 GHz, system 6, with a transmitted power of -10 dB. These systems had SNRs of 25 dB and 15 dB for systems 5 and 6, respectively, using a subharmonic mixing detector. The higher frequencies associated with these systems create such high retromodulator directivities that the passive and active THz links have virtually identical performance for the 3 cm retromodulator.

The other clearly apparent result in Figure 3.1 is that the incoherent nature of zero-bias detectors prevents them from detecting signals with a useful SNR, whereas the coherent subharmonic mixers have SNRs above 15 dB for every transmitter within their detection range (with the exception of system 2). Additionally, passive THz links for lower frequencies underperformed active links by up to 10 dB, whereas the difference was negligible for higher frequencies due to increased device directivity. Finally, it must be emphasized that these results are for a 5 m link.

The overwhelming effect that link length has on detected power means that adjusting the link length will dramatically change the results. Each doubling of the link length will decrease the detected power of all active THz links by 6 dB and all passive THz links by 12 dB due to path loss. By two doublings (a 20 m link), the ideal passive THz link will no longer be able to close the link for any system. By contrast, the active THz link could operate up to four doublings (an 80 m link) before failing. The link length could be extended by increasing the transmitter directivity, but this would reduce the network coverage area.

In summary, this analysis shows that ideal passive uplinks are certainly feasible over short link lengths with currently available technology. In the next section, the non-idealities of THz retromodulation will be reviewed and the real passive uplinks will be added to the link budget analysis.

3.4 Real Retromodulation Analysis

The previous section contrasted active THz links with ideal passive THz links and concluded that ideal passive THz links are feasible for short range wireless THz communication links assuming an ideal retromodulator. With that conclusion, this section contrasts active THz links with real passive THz links, described by the real retromodulation equation, to determine if passive THz links are feasible using a real retromodulator. Real retromodulators will be subject to additional loss due to lower retroreflection efficiency, glancing incident angles, low modulation efficiency, and low insertion efficiency. These losses will be analysed for two types of retroreflector, cornercube and spherical, as well as two types of modulator, optical and electronic. The section will conclude with a link budget analysis given by the real retromodulation equation comparing real passive THz links to active THz links to determine if real passive THz links can still be closed.

3.4.1 Cornercube Retroreflectors

This section will analyse how cornercube retroreflectors deviate from an ideal retroreflector and will quantify these deviations as additional losses in the form of retroreflection efficiency, η_{re}, and incident angle efficiency, η_{IA}. The analysis was carried out using a ray tracing algorithm that determines the portion of power that is retroreflected for a range of incident angles. While this may not give perfect results, since the incident THz signal has wavelengths

that are an appreciable portion of the dimensions of the cornercube and the incident THz signal with be slightly diverging, the ray tracing analysis will still give an indication of the general trend. The incident angle efficiency is taken to be proportional to the power capture area of the cornercube. The power capture area is determined by illuminating the cornercube with a rastered grid of rays and counting the number of rays that are returned to the source assuming perfect reflection off each internal surface. The grid of rays was tilted to various azimuthal and polar angles. Figure 3.2a shows the results for power capture area as a function of incident azimuthal and polar angles for a cornercube with triangular faces. The results are normalized to the case of normal incidence, i.e. the polar angle is zero. Figure 3.2b shows the normalized retroreflected signal as a function of incident polar angle for a few different incident azimuthal angles. This better shows that the deviation in normalized retroreflected signal is virtually independent of incident azimuthal angle, especially for small incident polar angles. The shape of the returning beam is shown in Figure 3.2c along with the outline of the cornercube for normal incidence. This clearly shows the shape of the aperture imposed by the cornercube as well as the fraction of power retroreflected compared to the size of the cornercube. While the internal surfaces of the cornercube may be perfectly reflective if coated with gold or another highly reflective metal in the THz spectrum [80], the periphery of the cornercube does not typically contribute to the retroreflected signal. Additionally, the irregular shape of the cornercube makes it difficult to compare to alternative retroreflectors, such as spheres. Therefore, the retroreflection efficiency will be taken to be the portion of the signal that returns relative to the total signal incident on the area of a circle encapsulating the front profile of the cornercube. An image of the fabricated cornercube used to gather these experimental results in this thesis is shown in Figure 3.2d.

The results in Figure 3.2a show that retroreflected power is largely independent of incident azimuthal angle, although slight periodic deviations occur every 120°. The solid line in Figure 3.2b shows a slice of the surface in Figure 3.2a at $\phi = 30°$, the dashed line shows a slice of the surface at $\phi = 0°$, and the dotted line shows a slice of the surface at $\phi = 60°$. The angular dependence of the normalized retroreflected signal from the cornercube retroreflector can be modelled empirically to be $\cos(2.3\theta)$, shown as the circles in Figure 3.2b. The weak correlation between the angular dependence of the normalized retroreflected signal and incident azimuthal angle allows any

incident azimuthal angle dependence to be neglected. This omission introduces an average error magnitude of less than 3% over all incident angles. The angular dependence of the normalized retroreflected signal will be factored into the real retromodulation equation using incident angle efficiency, η_{IA}, which is equal to the square of the angular dependence of the normalized retroreflected signal. The square relationship is due to the area of the retroreflector affecting the directivity of the retroreflector, which is squared in the real retromodulation equation due to the cornercube acting as both a receiving and transmitting aperture. For cornercube retroreflectors the incident angle efficiency is, $\eta_{IA} = \cos^2(2.3\theta)$.

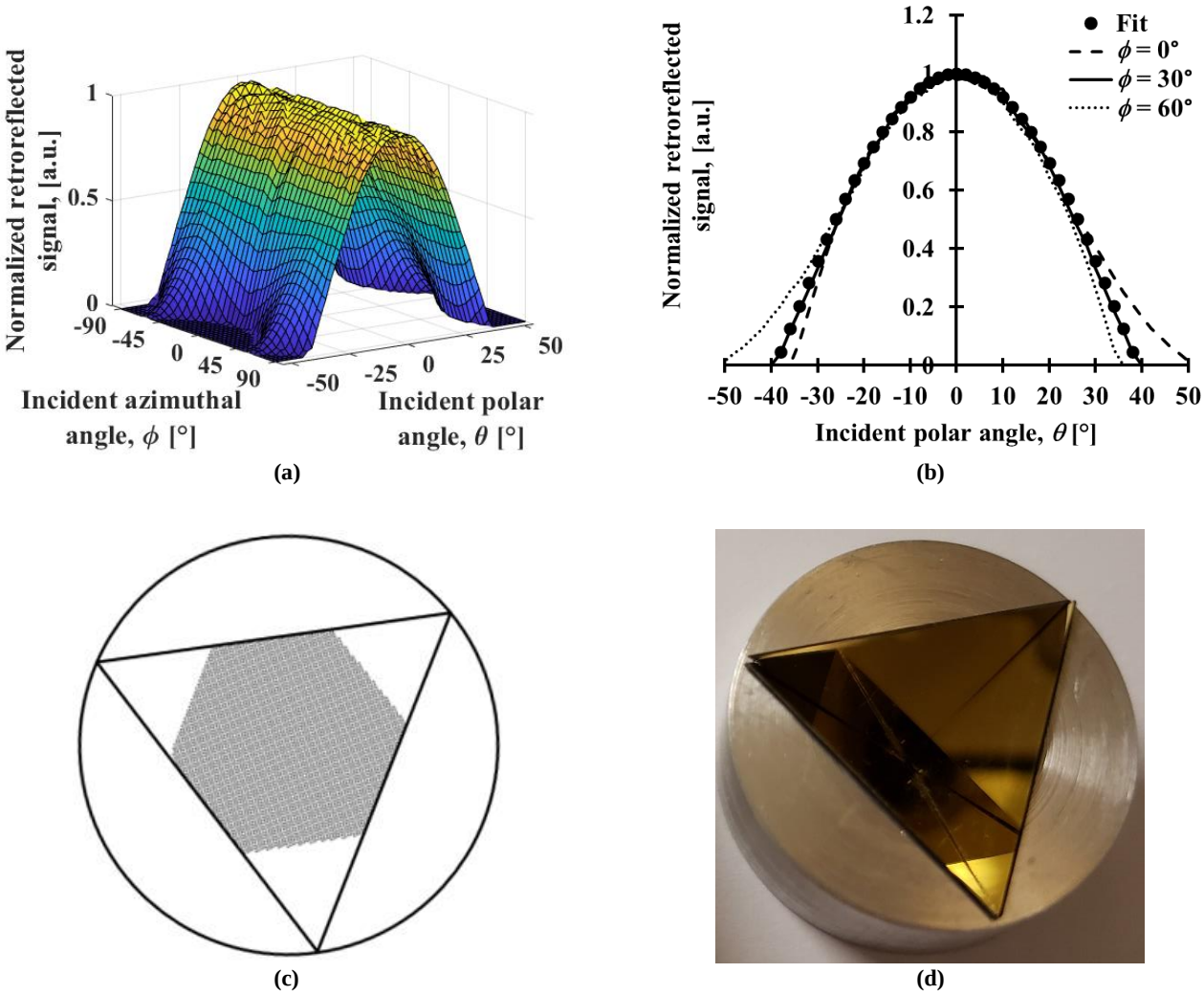

Figure 3.2: Normalized retroreflected signal dependence on incident azimuthal angle, ϕ, and incident polar angle, θ, is shown in (a) for cornercube retroreflectors with triangular sides. A slice of the curve in (a) at ϕ = 0°, denoted by the dashed line, ϕ = 30°, denoted by the solid line, and ϕ = 60°, denoted by the dotted line, is shown in (b). The circles in (b) correspond to the empirical fit for the angular dependence of the power capture area. A diagram showing the portion of the retroreflector that actually returns power to the source is shown in (c). An image of the cornercube used to gather the experimental results in the rest of the thesis is shown in (d).

The ray tracing analysis also shows the percentage of the retroreflector area that is actually retroreflected. To fairly compare cornercubes to dielectric spheres, the overall area of the retroreflector is defined as the smallest circle that can enclose the equilateral triangle formed by the cornercube. Figure 3.2c shows the overall area, as the large circle, the outline of the cornercube when viewed from normal incidence, the equilateral triangle, and the area where power is actually retroreflected, the black dots. Each black dot in Figure 3.2c represents a ray in the ray tracing analysis. Clearly the majority of the overall area of the retroreflector does not retroreflect any power. For normal incidence, the ratio of the area that retroreflects power to the overall area of the retroreflector is $\sqrt{3}/2\pi$ or approximately 27.5%. This reduced area will be incorporated into the retroreflection efficiency, which is now $\eta_{re}(\omega) = \sqrt{3}/2\pi$ assuming perfect reflection off each internal surface of the cornercube.

3.4.2 Spherical Retroreflectors

This section will analyse how spherical retroreflectors deviate from an ideal retroreflector and will quantify these deviations as additional losses in the form of retroreflection efficiency, $\eta_{re}(\omega)$, and incident angle efficiency, η_{IA}. A similar ray-based analysis to the one done for cornercube retroreflectors is shown below in Figure 3.3 for spherical retroreflectors with the same limitations. This analysis assumes that the back half of the spherical retroreflector is coated in a highly reflective metal, such as gold. Therefore, the retroreflection efficiency would be 100% for normal incidence if material loss and Fresnel reflection off the front surface were ignored. However, the ray tracing analysis below includes Fresnel losses, and material losses will be accounted for later. The ray tracing analysis shows the reduction in the normalized retroreflected signal with increasing incident polar angle in Figure 3.3a. The rotational symmetry of the spherical retroreflector eliminates any dependence in the normalized retroreflected signal on incident azimuthal angle. The reduction in retroreflected power based on Fresnel reflection at the front surface of the sphere is shown in Figure 3.3b.

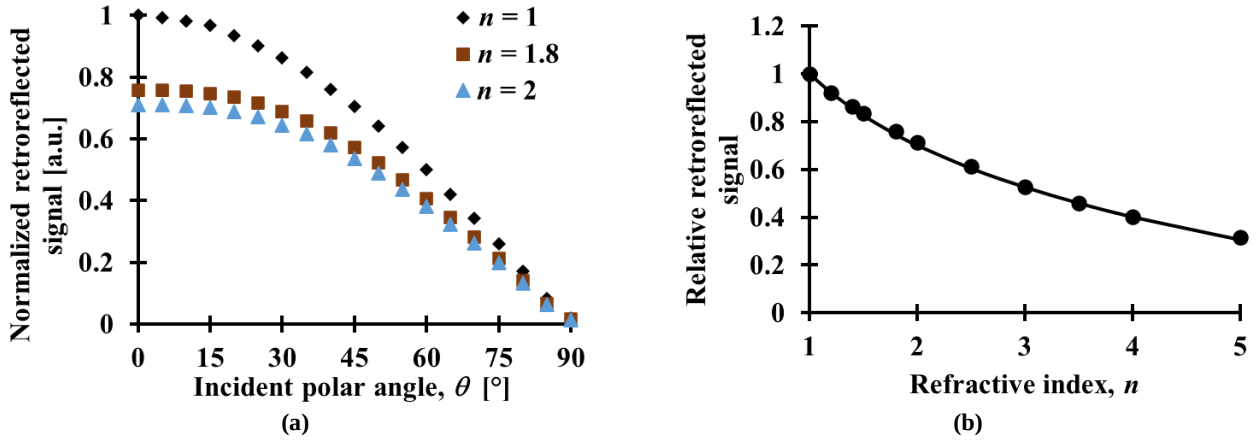

Figure 3.3: Ray tracing results for normalized retroreflected signal of a sphere are shown as a function of incident polar angle in (a). Results include power capture area and losses from surface reflection at n = 1, as black diamonds, n = 1.8, as red squares, and n = 2.0, as blue triangles. The decrease in retroreflected signal due to Fresnel reflection off the front surface of the sphere is plotted in (b) as a function of sphere refractive index.

Ray tracing results are obtained for several different scenarios. In the simplest scenario, which assumes no Fresnel reflection off the front surface of the spherical retroreflector, the normalized retroreflected signal is equal to the angular dependence of the normalized retroreflected signal from a tilted hemisphere and is shown by the black diamonds in Figure 3.3a, which can also be calculated to be $\cos(\theta)$. Practically, the presence of a dielectric interface at the surface of the sphere will reduce the retroreflected signal due to Fresnel reflection. To account for this, additional ray trace analyses were done to include surface effects for two different refractive indices. In Figure 3.3a, the red squares correspond to $n(\omega) = 1.8$, and the blue triangles correspond to $n(\omega) = 2$. Simulating for $n(\omega) = 2$ was explained previously as it corresponds ideal refractive index for retroreflection based on ray theory. The simulation at $n(\omega) = 1.8$ represents the ideal refractive index for spherical THz retroreflectors as identified by Born *et al*. [44]. Even with the dielectric interface, the retroreflection results follow a similar $\cos(\theta)$ trend as the results that did not consider the interface. Therefore, the angular dependence of the normalized retroreflected signal of the spherical retroreflector can be modelled with a simple expression, $\cos(\theta)$, giving an incident angle efficiency of, $\eta_{IA} = \cos^2(\theta)$. The effects of surface reflection at normal incidence are shown in Figure 3.3b, which show decreasing retroreflected signal for higher refractive index spheres. The relationship between retroreflected signal and refractive index can be modelled empirically by fitting the retroreflection efficiency, which gives $\eta_{re}(\omega) = 1 - 0.431\ln(n)$.

Another mechanism that reduces retroreflected power from a spherical retroreflector is material loss. The presence of material loss in the spherical retroreflector brings about an interesting trade-off when determining the diameter of the spherical retroreflector. While it was concluded earlier that a larger retroreflector drastically improves the link budget, these larger retroreflectors will also have increased material loss making them less desirable. A simple optimization can be done by taking the product of the gain introduced by increasing sphere diameter and the material loss in the sphere to give the optimal diameter, d, given a specific power absorption coefficient, $\alpha(\omega)$. The material loss in the sphere is defined to be $\exp(-2\alpha(\omega)d)$, which is for two passes through the sphere, and the gain introduced by the area of the sphere to be $\pi^2 d^4 / 16$, which is the square of the retroreflector cross sectional area. Optimizing gives an analytical result for the ideal sphere diameter, which is $d = 2 / \alpha(\omega)$. Consequently, the 2 cm diameter spheres shown in the previous section would be optimal for a material with a power absorption coefficient of 1 cm^{-1}. This power absorption coefficient is a maximum optimal coefficient for the sphere diameter, although lower loss would be preferable. Including material losses in the expression for spherical retroreflection efficiency gives $\eta_{re}(\omega) = (1 - 0.431\ln(n))\exp(-2\alpha(\omega)d)$.

3.4.3 Electronic Modulators

This section will analyse how electronic modulators deviate from an ideal modulator and will tabulate these deviations as additional losses in the form of modulation efficiency, $\eta_{mod}(\omega)$, and insertion efficiency for the modulator, $\eta_{in}(\omega)$. Unlike the other components of a retromodulator discussed so far, electronic modulators do not have an easily definable value or equation for these losses. Therefore, all that will be given in this section is a table showing the losses for various modulators described in the literature. It should be noted that for retromodulators employing the shutter architecture, the modulator must be passed through twice, and thus the modulation efficiency and insertion efficiency may also need to be applied twice. Most electronic modulators in the literature are designed with modulation efficiency in mind and have poor insertion efficiency. Additionally, many designs, especially those based on dipole antenna arrays [53], only modulate one polarization. The unknown orientation of the mobile transceiver with respect to the fixed transceiver means that a real retromodulator with polarization sensitive designs

is unacceptable. Designs with symmetric antenna elements are superior as they are much more immune to polarization effects.

Table 3.2 gives a summary of insertion efficiency and modulation efficiency for two electronic modulator technologies. These were the designs given in Table 2.4 that were polarization insensitive. For convenience, the remaining information from Table 2.4 is reproduced here. Values are given for two passes through the modulator as these discrete modulators would be used in a shutter architecture retromodulation system.

Table 3.2: Summary of insertion efficiency and modulation efficiency for polarization insensitive electronic THz modulators from the literature

Frequency (GHz)	Carrier bandwidth (GHz)	Modulation rate (MHz)	Drive voltage (V)	$\eta_{in}(\omega)$	$\eta_{mod}(\omega)$	Ref
850	150	2.75	-4	<0.01	>0.99	[55]
630	150	0.08	15	0.01	0.83	[54]

The table clearly confirms that both free-space modulators were designed with modulation efficiency in mind resulting in poor insertion efficiency, though both have excellent modulation efficiency. It should be noted that many of the electronic designs both here and in Table 2.4 provide results over a wide bandwidth, with varying insertion efficiency and modulation efficiency away from the quoted frequency. A few designs have insertion efficiencies near one for frequencies other than the quoted frequency, while still having good modulation efficiency [53]. This shows that a viable modulator could be designed and fabricated for THz retromodulation by altering the design criteria. To estimate the performance of a modulator more suited to retromodulation, later analyses will consider a theoretical modulator with a single pass insertion efficiency of 0.9 and modulation efficiency of 0.2. Due to the complexity of designing and fabricating electronic modulators, no additional analysis or design work will be given in this thesis.

3.4.4 Optical Modulators

This section will analyse how optical modulators deviate from an ideal modulator and will quantify these deviations as additional losses in the form of modulation efficiency, $\eta_{mod}(\omega)$, and insertion efficiency for the modulator, $\eta_{in}(\omega)$. As discussed earlier, optical modulators come in two general designs: semiconductors utilizing Drude free carrier

absorption, and frequency-selective surfaces. Frequency-selective surface based optical modulators are similarly difficult to quantify as their electronic counterparts due to their performance being greatly design dependent [49], [111], [112]. Therefore, modulation efficiency and insertion efficiency are simply tabulated in Table 3.3 along with operating frequency, modulation rate, and optical pump power for two passes through the modulator. Modulators that required optical pumping with a pulsed laser are denoted by a "P" in the table and modulators that operate using a continuous wave laser are denoted "CW" in the table.

Table 3.3: Summary of the performance of various frequency-selective surface based optical THz modulators

Frequency (GHz)	$\eta_{in}(\omega)$	$\eta_{mod}(\omega)$	Modulation rate (MHz)	Pump power (W)	Ref
800	0.41	0.96	N/A	0.5 P	[49]
550	0.13	0.99	N/A	1.5 P	[112]
Broadband	0.36	0.83	0.1	0.4 CW	[51]

The challenge with specifying many of these modulators lies in the fact that they require optical pumping by a pulsed laser amplified by a regenerative amplifier [49], [112]. While these modulators have picosecond response times, they require extremely high-power lasers, and are thus not practical for mobile THz transceivers. This reasoning also applies to modulators utilizing Drude free carrier absorption with a picosecond charge carrier lifetime.

While frequency-selective surface based optical modulators are difficult to model, the modulation efficiency and insertion efficiency of semiconductors utilizing Drude free carrier absorption can be modelled with a high degree of accuracy. These modulators take the form of a semiconductor wafer, so insertion efficiency can be equated to the Fresnel losses off the surface of the modulator. Fresnel losses are unique in that they only apply to the incoming pass through the modulator for retromodulators utilizing the shutter architecture. Any reflection of the outgoing beam will simply be redirected into the retroreflector and return to the modulator once retroreflected again. While this may cause interference effects for frequencies with low insertion efficiency, these effects will be negligible for frequencies with high insertion efficiency, which is the objective for modulator design. The general equation for the transmissivity through a semiconductor modulator needs to consider both reflection and transmission off the

front and back surfaces. In the case of high-refractive index modulators (which are common), transmissivity also needs to consider internal reflections. Finally, for modulators that are only a few wavelengths thick (common for THz wavelengths), transmissivity must also consider interference effects caused by the presence of standing waves within the modulator. One rigorous analysis takes the travelling wave equation and propagates it through the modulator with an infinite number of internal reflections. This gives the complex electric field, containing both amplitude and phase information, of the wave passing through a modulator immersed in free space to be

$$E_{\mathrm{t}}(\omega) = E_0(\omega) t_{\mathrm{in}}(\omega) t_{\mathrm{out}}(\omega) e^{-k_0 \kappa(\omega)\delta} e^{-\mathrm{j}(k_0 n(\omega)\delta - \omega t)} \sum_{i=0}^{\infty} r(\omega)^{2i} e^{-2ik_0 \kappa(\omega)\delta} e^{-\mathrm{j}2ik_0 n(\omega)\delta}, \tag{3.5}$$

where

$$t_{\mathrm{in}}(\omega) = \frac{2}{n(\omega)+1}, \tag{3.6a}$$

$$t_{\mathrm{out}}(\omega) = \frac{2n(\omega)}{n(\omega)+1}, \tag{3.6b}$$

and

$$r(\omega) = \frac{n(\omega)-1}{n(\omega)+1}. \tag{3.6c}$$

In these equations, $E_0(\omega)$ is the incident electric field amplitude and δ is the modulator thickness. The summation term, whose index is *i*, represents contributions from internal reflections. Note that this expression includes absorption loss, which means that it can be used to describe signals with or without modulation applied. The infinite series in (3.5) converges allowing (3.5) to be simplified into

$$E_{\mathrm{t}}(\omega) = E_0(\omega) t_{\mathrm{in}}(\omega) t_{\mathrm{out}}(\omega) \frac{e^{-k_0 \kappa(\omega)\delta} e^{-\mathrm{j}(k_0 n(\omega)\delta - \omega t)}}{1 - r(\omega)^2 e^{-2k_0 \kappa(\omega)\delta} e^{-\mathrm{j}2k_0 n(\omega)\delta}}. \tag{3.7}$$

Insertion efficiency and modulation efficiency in the retromodulation equations are intensity ratios (equivalent to power ratios), so the complex electric field must be converted to intensity. This is done by squaring the magnitude of the electric field and dividing it by twice the free space impedance, η. Doing so gives

$$I(\omega) = \frac{\left|E_t(\omega)\right|^2}{2\eta} = I_0(\omega)T(\omega)^2 e^{-2k_0\kappa(\omega)\delta} \frac{1}{1-2R(\omega)e^{-2k_0\kappa(\omega)\delta}\cos(2k_0 n(\omega)\delta) + R(\omega)^2 e^{-4k_0\kappa(\omega)\delta}}, \quad (3.8)$$

where

$$T(\omega) = t_{in}(\omega)t_{out}(\omega) = \frac{4n(\omega)}{(1+n(\omega))^2}, \quad (3.9a)$$

and

$$R(\omega) = r(\omega)^2 = \left(\frac{n(\omega)-1}{n(\omega)+1}\right)^2. \quad (3.9b)$$

In this expression, the incident intensity is defined as $I_0(\omega) = \left|E_0(\omega)\right|^2 / 2\eta$. The insertion efficiency calculation takes the previous expression for intensity and assumes no absorption loss, then normalizes by the incident intensity to obtain

$$\eta_{in}(\omega) = T(\omega)^2 e^{-2k_0\kappa(\omega)\delta} \frac{1}{1-2R(\omega)e^{-2k_0\kappa(\omega)\delta}\cos(2k_0 n(\omega)\delta) + R(\omega)^2 e^{-4k_0\kappa(\omega)\delta}}. \quad (3.10)$$

The insertion efficiency shows several interesting phenomena. First, the entire expression is multiplied by $T(\omega)^2$, which demonstrates that power must pass into and out of the modulator exactly once. Second, the fraction represents the interference effects caused by standing waves in the modulator, where the cosine terms dictates whether the interference is constructive or destructive. The frequencies that observe perfect constructive or destructive interference are periodic with a frequency spacing of $2k_0 n(\omega)\delta$, which corresponds to the free spectral range of the

modulator. In the case of no extinction, i.e. $\kappa(\omega) = 0$, perfect constructive interference, corresponding to unity transmission, can be shown by converting $T(\omega)^2$ into $(1\text{-}R(\omega))^2$.

The equations above are for normal incidence, which this is an excellent approximation for unpolarized signals at most incident angles. Ignoring phase interference effects, the normal incidence approximation introduces an error below 1% for incident polar angles below 37° when $n(\omega) = 2$, 44° when $n(\omega) = 3$, and 70° when $n(\omega) = 4$. At steeper polar angles past these cutoffs, the insertion efficiency will degrade quickly. Including phase interference effects for other incident angles would require modifying the distance through the modulator, δ, to account for the fact that the internal waves would be travelling diagonally through the modulator, and thus would have a longer path length. Additionally, the transmission and reflection coefficients, as well as the transmissivity and reflectivity would need to be modified to include the incident angle and the transmitted angle within the modulator. These modifications greatly complicate (3.10) and so were not considered in this thesis.

The expression for modulation efficiency is a bit more involved. First, the modulation efficiency is defined to be $\eta_{\text{mod}}(\omega) = 1 - \left(I_{\text{on}}(\omega) / I_{\text{off}}(\omega)\right)$, where $I_{\text{on}}(\omega)$ is the intensity being transmitted through the modulator when the modulator is on (absorbing) and $I_{\text{off}}(\omega)$ is the intensity transmitted through the modulator when the modulator is off (no absorption). It is important to remember that modulation can perturb both the refractive index and extinction coefficient within the modulator, which are denoted $\Delta n(\omega)$ and $\Delta\kappa(\omega)$, respectively. Populating the equation, cancelling out a few common terms gives

$$\eta_{\text{mod}}(\omega) = 1 - e^{-2k_0\Delta\kappa(\omega)\delta}\frac{1 - 2R(\omega)e^{-2k_0\kappa(\omega)\delta}\cos(2k_0 n(\omega)\delta) + R(\omega)^2 e^{-4k_0\kappa(\omega)\delta}}{1 - 2R(\omega)e^{-2k_0(\kappa(\omega)+\Delta\kappa(\omega))\delta}\cos(2k_0(n(\omega)+\Delta n(\omega))\delta) + R(\omega)^2 e^{-4k_0(\kappa(\omega)+\Delta\kappa(\omega))\delta}}. \quad (3.11)$$

It can be seen that modulation efficiency will be increasingly frequency dependent as the modulator refractive index increases, since the arguments for each cosine term become more dissimilar. Interestingly, this shift in the location of the internal reflection resonances during modulation allows for increased transmission or negative modulation efficiencies if the cosine term in the denominator becomes significantly larger than the one in the numerator. It can

also be seen that the presence of extinction disrupts the interference effects in the denominator. Consequently, deeper modulation will result in fewer interference effects in the transmitted beam. A very simple first order approximation of (3.11) is to ignore internal reflections and interference effects to give a modulation efficiency of

$$\eta_{\mathrm{mod}}(\omega) = 1 - e^{-2k_0\kappa(\omega)\delta}. \tag{3.12}$$

This corresponds to the average modulation efficiency over a wide range of frequencies and is useful for determining the modulation efficiency order of magnitude. However, especially for modulators with high refractive indices, modulation efficiency must be calculated using (3.11). Figure 3.4 shows modulation efficiency as a function of frequency calculated using the simple approximation in (3.12), thick line, and the full equation in (3.11), dashed line. In Figure 3.4a, the modulator has a refractive index of $n(\omega) = 4$, a thickness of $\delta = 350$ μm, and an extinction coefficient of $\Delta\kappa(\omega) = 0.01$. In Figure 3.4b, the modulator has an additional change in refractive index of $\Delta n(\omega) = 0.015$ over the modulator in Figure 3.4a.

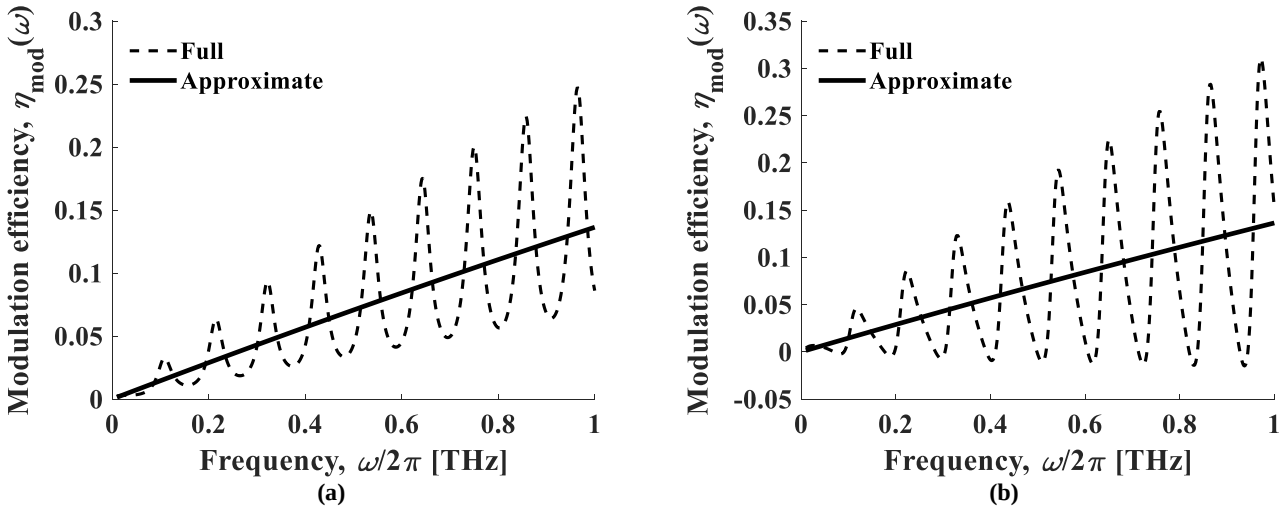

Figure 3.4: Modulation efficiency as a function of THz frequency is shown for two modulators, (a) and (b), and two numerical models. Both modulators have a refractive index of $n(\omega) = 4$, a thickness of $d = 350$ mm, and an extinction coefficient of $\Delta\kappa(\omega) = 0.01$. In (a) there is no change in refractive index, while in (b) there is a change in refractive index of $\Delta n(\omega) = 0.015$. In both figures, the modulation efficiency as a function of frequency calculated using the simple approximation in (3.12), thick line, and the full equation in (3.11), dashed line.

Several things are apparent from the figure. First, the simple approximation does indeed follow the average modulation efficiency; however, this approximation is of limited use seeing as the large refractive index of the

modulator makes modulation efficiency extremely frequency dependent. Second, the frequency dependence of the modulation efficiency takes the form of fringes superimposed on top of the average modulation efficiency as expected. These fringes are the result of phase interference effects, and the maxima are separated by the free spectral range of the modulator. Finally, the effects of a small change in refractive index during the process of modulation significantly impacts the modulation efficiency etalons. The change in refractive index during modulation alters the free spectral range of the modulator, resulting in etalon fringes that do not line up in the frequency domain. As a result, the fringes in the modulation efficiency are more pronounced and can even give negative modulation efficiencies.

3.4.5 Link Budget Analysis

Now that the nonidealities of THz retromodulators have been explored, it is time to populate the real retromodulation equation and assess the feasibility of passive THz links. This analysis will only include passive THz links from Section 3.3 that were deemed viable. For simplicity, only systems with 2 cm retromodulators and 10 cm detecting apertures will be analysed. Retroreflection efficiency is -5.6 dB for all corner cubes and is -10 dB for all spheres. The modelled spheres are assumed to be made of a composite material with a refractive index of 1.8 and power absorption coefficient of 0.5 cm^{-1} at 300 GHz and 1 cm^{-1} at 1 THz. Two different modulators are considered for the analysis. Modulator one is based on optical free carrier absorption with an insertion efficiency of $\eta_{in}(\omega)$= 0.17 and a modulation efficiency of $\eta_{mod}(\omega)$ = 0.94 for two passes. Modulator two is based on the theoretical electronic modulator discussed earlier with an insertion efficiency of $\eta_{in}(\omega)$ = 0.81 and a modulation efficiency of $\eta_{mod}(\omega)$ = 0.36 for two passes. Figure 3.5 shows the retromodulation link budget for active THz links (AL), ideal passive THz links (IPL), real passive THz links with modulator one (RPL1), and real passive THz links with modulator two (RPL2). Both real passive THz links are analysed for both cornercube retroreflectors (CCRR) and spherical retroreflectors (Sphere). All active THz links use the same parameters as Section 3.3. All links assume normal incidence, i.e., θ = 0° and η_{IA} = 0 dB. Finally, only the noise floor for the subharmonic mixing detector is shown, for a bandwidth of 1 GHz, since it is vastly superior to the zero-bias detector.

Figure 3.5 indicates that real passive THz links lose an additional 10 dB to 20 dB over ideal passive THz links and that cornercube retroreflectors outperform spherical retroreflectors by a few dB because of their higher retroreflection efficiency. The majority of the losses for all real retromodulation systems were due to poor retroreflection efficiency. For the cornercube retroreflector, the outer points of the cornercube could be removed so that a much larger cornercube fits into the same circular area (see Figure 3.2). The outer points do not contribute to retroreflection at normal incidence, only at glancing angles where performance is already poor. This would improve system performance by a few dB. For spherical retroreflectors, the material loss in the sphere eliminates approximately 90% of the retroreflected signal. By finding a lower loss material, this could be reduced significantly.

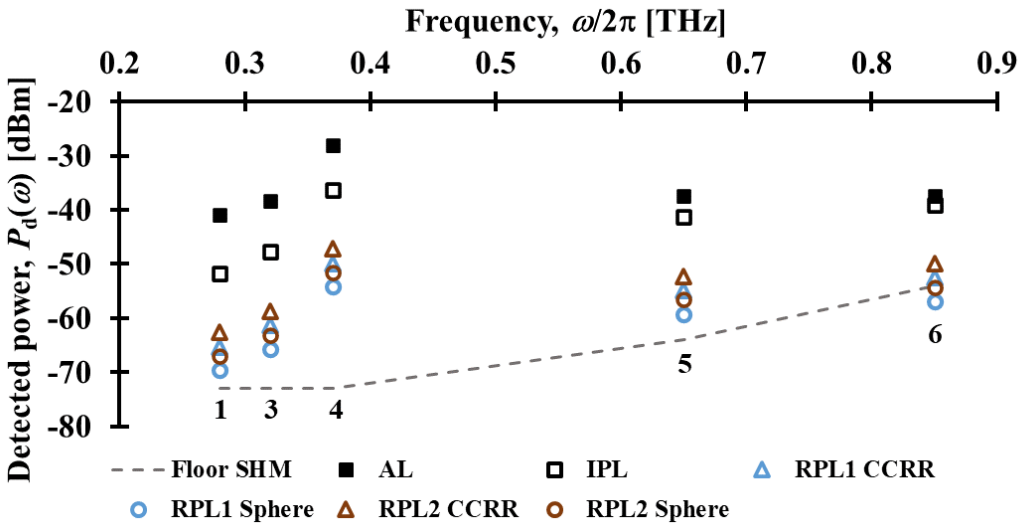

Figure 3.5: Real passive THz link budget results for the five viable systems in Section 3.3 are shown along with the noise floor for subharmonic mixing detector with a bandwidth of 1 GHz (SHM). The number shown below each set of results corresponds to the respective system. The parameters for each of these systems were given in Table 2.1. Each system has six link budgets, one active THz link (AL) and one ideal passive THz link (IPL) from Section 3.3, two real passive THz links with modulator one (RPL1), and two real passive THz links with modulator two (RPL2). Each modulator is analysed with a spherical (Sphere) or cornercube (CCRR) retroreflector. The results are for normal incidence, i.e., a polar angle of $\theta = 0°$.

While the material losses in this simulation may seem somewhat higher than most values in Table 2.3, they are comparable to the material losses seen in the experimentally fabricated composite materials in Section 4.2. Overall, the losses incurred by the retromodulator are still small when compared to the path loss of the whole wireless THz communication link. The results in Figure 3.5 are for normal incidence but results for any angle can be determined by incorporating the incident angle efficiency, which is plotted in Figure 3.6 as a function of incident polar angle for both cornercube retroreflectors (dashed line) and spherical retroreflectors (solid line). The curves in Figure 3.6

emphasize just how much wider the FOV of the spherical retroreflector is compared to the cornercube retroreflector, with incident angle loss 3-dB points at 20° and 60° for the cornercube and spherical retroreflectors, respectively.

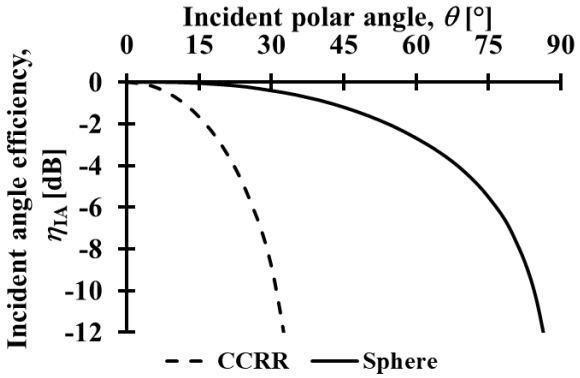

Figure 3.6: Incident angle efficiency as a function of incident polar angle is shown for both cornercube (dashed line) and spherical (solid line) retroreflectors.

For systems 1 and 3 in Figure 3.5, an SNR above 10 dB is feasible for the cornercube retroreflector, but not the spherical retroreflector regardless of modulator. Even factoring in a few dB of additional loss due to glancing incidence, all these systems can still operate with a sufficiently large SNR making them viable options for passive THz links, with the exception of the spherical retroreflectors in system 1. The SNR improves to over 15 dB for higher power BWO transmitters in system 4. This makes them a viable option for passive THz links in terms of power, although other considerations could make BWOs impractical. The results for the two theoretical systems 5 and 6 are also insightful. The detected power for these systems is only slightly lower than those for the higher power BWO transmitter, so one could conclude that these systems are more practical. However, the subharmonic mixer noise floor drastically increases at higher frequencies as generating the heterodyning local oscillator becomes more challenging. As a result, the SNR for system 5 is barely above 5 dB and the retromodulated signal in system 6 is at or below the noise floor. Evidently, despite increased directivities at higher operational frequencies, difficulty detecting these frequencies hampers their usefulness. In summary, systems based on high-frequency electronic transmitters and detectors (i.e., systems 1 and 3) are the most viable options for the implementation of passive THz links. The combination of commercial availability of components, reasonable power output from transmitters, and high coherent detector sensitivity make these systems superior to the other options presented here. The remaining chapters of this thesis will be dedicated to the implementation of a real passive THz links.

Chapter 4: Terahertz Retroreflectors

The previous chapters have laid out the theoretical framework for THz retromodulation and have shown it to be theoretically feasible. In this chapter, a comprehensive analysis of the fabrication and experimental testing of retroreflectors is presented. The results are compared to the theoretical predictions in Chapter 3. Both cornercube and spherical retroreflectors will be analysed. It is found that the performance of cornercube retroreflectors agrees well with the theoretical analysis, while spherical retroreflectors are challenging to implement due to material loss.

The remaining chapters of this thesis will present experimental data gathered for real retroreflectors, modulators, and retromodulators. All of this experimental data is gathered using a THz time-domain spectroscopy (TDS) measurement system. While THz TDS is not suitable for data communication due to its pulsed operation, it is ideal for characterising system components as it is inherently broadband and coherent. This allows a single measurement system to gather amplitude and phase data for a wide range of THz frequencies. A brief description of the THz TDS system will be given here. For a more in-depth discussion, the literature contains many excellent descriptions of THz TDS systems [117]. While there are several THz TDS systems used in this work, all of them are comprised of three elements: the emitter, the beam focusing optics, and the detector. A brief synopsis of each element is given below.

There are many different THz TDS emitter technologies including photoconductive switches [26], [118], optical rectification [119], and other novel effects [120]. Every system in this work uses a photoconductive switch as the THz emitter. These photoconductive switches are a piece of semiconductor with an external bias field placed across it. The biased semiconductor region is then illuminated by an ultrafast pulsed laser, typically with a pulse duration of approximately 100 fs. This rapidly generates charge carriers in the semiconductor, which are immediately accelerated by the bias field. Each of these accelerating charges radiates energy as a pulse. Therefore, the overall strength of the pulse is proportional to the charge carrier generation rate. An optical excitation pulse with a duration of 100 fs results in a radiated energy pulse with a bandwidth up to several THz. In practice, the bandwidth is limited by the bias field and the carrier mobility of the semiconductor selected as well as any absorption in the emitter,

beam focusing optics, or detector. This work uses semi-insulating GaAs as an emitter substrate due to its very high electron mobility and low THz absorption.

There are two prominent THz detection methods used in THz TDS systems, both are used in this work. The first is electro-optic detection [113], [118], which is used in most of the following THz TDS experiments. Electro-optic detection has an ultrafast probe pulse and the THz pulse simultaneously pass through an electro-optic crystal with electric field induced birefringence. To simultaneously pass both pulses though the electro-optic crystal, a pellicle is used as a dichroic beamsplitter to merge the probe pulses with the THz pulses. The probe pulse must be much shorter than the THz pulse. In this case, the THz pulse amplitude will appear to be effectively constant while the probe pulse passes through the electro-optic crystal. The amplitude of the THz pulse induces birefringence in the electro-optic crystal and rotates the polarization of the probe beam. This polarization rotation is measured by splitting the two polarizations of the probe beam after the electro-optic crystal and sending them into opposite sides of a differential photodetector. The change in polarization, which is recorded, is linearly related to the strength of the THz field. The allows the THz TDS system to sample the THz field at a specific point in time if the THz and probe pulses are synchronized, which is the case when both the THz emitter and detector to be fed by the same pulsed laser. By adjusting the time delay between the THz pulse and the probe beam pulse, the THz pulse can be reproduced as a time-domain waveform containing both amplitude and phase information. The time delay between the THz and probe pulses is modified using a motorized stage to adjust the path length of one of the beams. The crystal employed in all electro-optic detection systems in this work is <110>-cut ZnTe, which transmits THz radiation well up to 2.8 THz, where absorption from a broad longitudinal acoustic phonon peak at 3.7 THz reduces the measured signal [121].

The second detection method uses a photoconductive switch similar to the one in the emitter to carry out detection [117]. As opposed to the emitter, the photoconductive detector has no external bias field to the semiconductor substrate. Instead, the passing THz field acts as the bias field. Now, when an ultrafast probe pulse excites charge carriers in the semiconductor substrate of the detector, these charge carriers are accelerated by any THz electric field present, which generates a current of typically a few nanoamperes. This current is then detected using a low

noise transimpedance amplifier. In order to sample the THz electric field at a single point in time, the substrate must be a semiconductor material with a charge carrier lifetime that is much shorter than the THz pulse. In this case, the measured current is proportional to the passing THz electric field when the probe pulse arrives at the detector. Therefore, a time-domain waveform can be constructed by sampling over a range of time delays as was done for electro-optic detection. In the systems used in this work, low temperature grown GaAs is used as the detector substrate.

The beam focusing optics used in THz TDS systems are either lenses or parabolic mirrors. Parabolic mirrors are a common method of collimating and focusing THz radiation due to the large material losses associated with refractive optics. Systems with large beam diameters and high numerical apertures would require thicker refracting optics, and THz TDS systems with a wide bandwidth would suffer from the dispersion seen in some materials. Reflective optics overcome these issues using metallic coatings such as gold, which have virtually perfect reflection over the entire THz spectrum and no material losses nor dispersion. There are still situations where refractive optics are used in THz TDS systems. Materials such as HRFZ Si or certain polymers have low enough material losses that they can be used in systems requiring optics with a maximum thickness of about 1 cm. Regardless of the type of optic used, THz TDS systems typically have at least two optics: one to collimate THz radiation from the emitter and one to focus the collimated THz beam onto the detector. In systems requiring a small investigation area, two additional optical elements are used to create a focal point.

Several different THz TDS systems were used in this work. These systems varied in terms of beam diameter, bandwidth, the presence of a focal spot, and the ability to carry out reflection measurements. All of the systems are pictured in Figure 4.1. The first system used a photoconductive switch emitter and a photoconductive switch detector (Ekspla EMT-08 and DET-08). Both the emitter and detector were equipped with hyper-hemispherical lenses made of high resistivity Si to reduce the divergence of the THz beam. Both the emitter and detector were pumped by a 780-nm pulsed laser (Toptica Photonics, FFS.SYS-2B), with a 100-fs pulse duration and 90-MHz repetition rate. This pulsed laser beam is split into two arms, one of which is delayed using a motorized delay line and incident on the THz emitter with an average power of 25 mW, while the other is incident on the THz detector

with an average power of 10 mW. This produced THz radiation spanning 0.2 to 1.5 THz in a quasi-collimated beam between the emitter and detector. The beam diameter for this system was about 1 cm, limited by the diameter of the hyper-hemispherical lenses. The first system can be seen in Figure 4.1a. The second system used a photoconductive switch emitter and electro-optic detector with two parabolic mirrors. The mirrors created a collimated THz beam, which was approximately 2 cm in diameter, that traveled from the emitter to the detector. Both the emitter and detector were pumped by a femtosecond pulsed laser (Spectra Physics Mai Tai HP) at a wavelength of 780 nm, a pulse duration of 100 fs, and a repetition rate of 80 MHz. This produced THz radiation spanning 0.3 THz to 3 THz. In this system, and all of the following systems, the pulsed laser beam is split into two arms, one of which is delayed using a motorized delay line and incident on the THz emitter with an average power of 750 mW, while the other is incident on the THz detector with an average power of 1 mW. The second system can be seen in Figure 4.1b. The third system also made use of a photoconductive switch emitter and an electro-optic detector, though with four parabolic mirrors instead of two. The first parabolic mirror collimated the radiation from the THz emitter into a 5 cm diameter beam. The second and third mirrors focused and recollimated the THz beam with a minimum spot diameter of 1.5 mm at the focus, measured by passing a razor blade through the focus and observing the full-width at half-maximum of the beam as it is blocked. The fourth parabolic mirror focused the THz beam into the detector. This system was also pumped by a femtosecond pulsed laser (Spectra Physics Mai Tai HP) at a wavelength of 780 nm, a pulse duration of 100 fs, and a repetition rate of 80 MHz. This produced THz radiation spanning 0.3 THz to 3 THz. The third system can be seen in Figure 4.1c. The first three systems were only capable of making transmission measurements, though for various sized samples depending on beam diameter. The fourth system uses a photoconductive switch emitter and electro-optic detector arranged to measure the reflection off a sample. Measurement system two was modified into a Michelson interferometer to be able to measure retroreflection specifically. Two parabolic mirrors are used, one to collimate THz radiation from the emitter and one to focus THz radiation into the detector. The collimated beam coming from the emitter is split into two arms by a beamsplitter made of semi-insulating GaAs. The cornercube retroreflector was placed in one arm of the interferometer, while the other arm contained a flat mirror used for calibration. Since the interferometer was implemented for a pulsed measurement system, the signal from each arm could be measured separately so long as the path length of each arm

was sufficiently different. The reflected beam paths were then merged again by the beamsplitter and sent to the final parabolic mirror which focused the THz radiation into the detector. This system was also pumped by a femtosecond pulsed laser (Spectra Physics Mai Tai HP) at a wavelength of 780 nm, a pulse duration of 100 fs, and a repetition rate of 80 MHz. This produced THz radiation spanning 0.3 THz to 3 THz. The fourth system can be seen in Figure 4.1d.

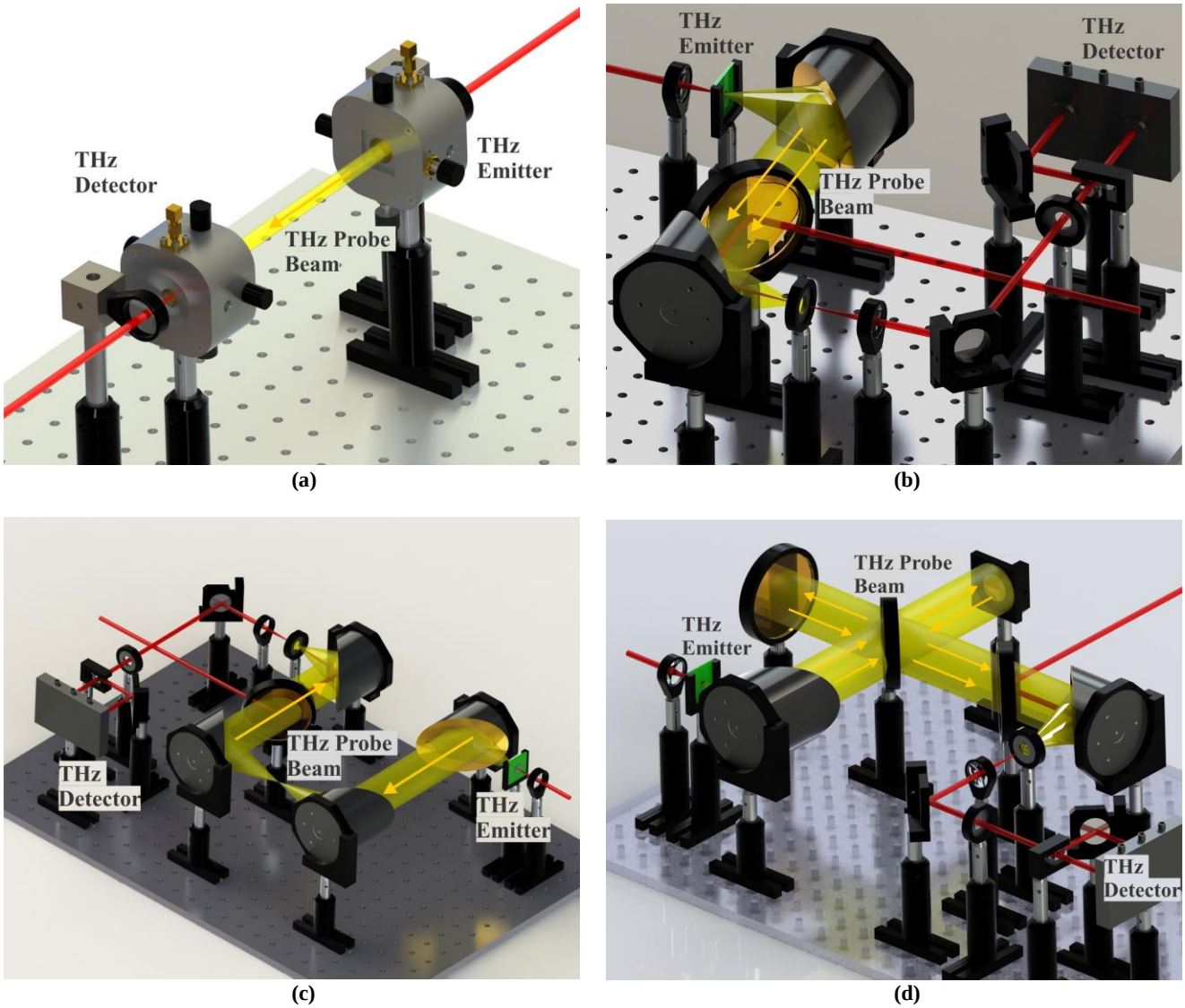

Figure 4.1: Images of the various THz TDS systems used in this work are shown. System one is shown in (a), system two is shown in (b), system three is shown in (c), and system four is shown in (d). In all figures, the yellow beam is the pulsed THz beam and the red beams are the ultrafast NIR beams pumping the emitters and detectors. In (b)-(d), the green square is the THz emitter and the large orange disc is the pellicle beamsplitter.

Measurements from the three transmission systems were fed into a parameter extraction algorithm to obtain the refractive index, $n(\omega)$, and extinction coefficient, $\kappa(\omega)$, of any samples present in the collimated THz beam. To extract these parameters, two THz TDS measurements are taken, one with the sample and one without. These scans are Fourier transformed into complex spectra, containing amplitude and phase data, which must be fit to a model of propagation through the sample in order to extract material parameters. The model for the signal propagating through the sample is

$$E(\omega) = E_0(\omega) t_{\text{in}}(\omega) t_{\text{out}}(\omega) \frac{e^{-k_0 \kappa(\omega)\delta} e^{-\text{j}(k_0 n(\omega)\delta - \omega t)}}{1 - r(\omega)^2 e^{-2k_0 \kappa(\omega)\delta} e^{-\text{j}2k_0 n(\omega)\delta}} . \tag{4.1}$$

Given the nature of this equation, it is impossible to write an explicit solution for the refractive index and extinction coefficient. There exist iterative algorithms to solve this problem [122]; however, in many circumstances, the internal reflections can be ignored. This is a good approximation when $r(\omega)^2 e^{-2k_0 \kappa(\omega)\delta} << 1$, which is the case for materials with a small refractive index (since Fresnel reflection is small) or materials with appreciable signal loss due to extinction during propagation through the sample. In this case, transmission through the sample can be approximated using

$$E(\omega) \approx E_0(\omega) t_{\text{in}}(\omega) t_{\text{out}}(\omega) e^{-k_0 \kappa(\omega)\delta} e^{-\text{j}(k_0 n(\omega)\delta - \omega t)} . \tag{4.2}$$

This produces explicit solutions for refractive index and extinction coefficient to be

$$n(\omega) = 1 + \left(\phi_{\text{THz}}(\omega) + 2\pi i\right) \frac{c}{\omega \delta} \tag{4.3}$$

and

$$\kappa(\omega) = -\ln\left[\frac{E(\omega)}{t_{\text{in}}(\omega) t_{\text{out}}(\omega) E_0(\omega)}\right] \frac{c}{\omega \delta} , \tag{4.4}$$

where $t_{in}(\omega)$ and $t_{out}(\omega)$ are the field transmission coefficients for the wave passing into and out of the sample, respectively, and δ is the sample thickness. Additionally, $E(\omega)$ is the measured amplitude spectrum with the sample in place, $E_0(\omega)$ is the amplitude spectrum without the sample, and ϕ_{THz} is the phase difference between the phase spectra with and without the sample in place. The measured phase difference only gives values between $\pm\pi$, so multiples of 2π need to be added to the measured phase to unwrap it if the phase rolls over. Additional detail on the effects of neglecting internal reflections is given in Appendix B. There is one significant limitation with this type of measurement, which is related to the extinction coefficient. The measurable extinction coefficient is bounded between maximum and minimum values, which are generally frequency dependent. The maximum extinction coefficient is related to the frequency spectrum dynamic range, $DR(\omega)$, of the TDS measurement system. The frequency spectrum dynamic range is defined as the signal strength of the background amplitude spectrum divided by the amplitude spectrum measured when the THz emitter is completely off (i.e., the noise floor) [123]. For the THz TDS systems used in this thesis, the maximum frequency spectrum dynamic range was typically between 100 and 500, corresponding to 40 dB and 54 dB, respectively. The variance in maximum frequency spectrum dynamic range comes from proper THz TDS setup alignment and whether the sample holder is blocking some of the power. For all systems, the frequency spectrum dynamic range is frequency dependent and decreases with increasing frequency with the exception of frequencies below 300 GHz. An example of the frequency spectrum dynamic range of a THz TDS system is shown in Figure 4.2a. The maximum extinction coefficient for each frequency, which is defined as the measured extinction coefficient at each frequency when the THz beam is completely blocked, can be calculated using

$$\kappa_{max}(\omega) = \frac{c \ln\left[t_{in}(\omega) t_{out}(\omega) \mathrm{DR}(\omega)\right]}{\omega\delta}, \tag{4.5}$$

and is shown in Figure 4.2b.

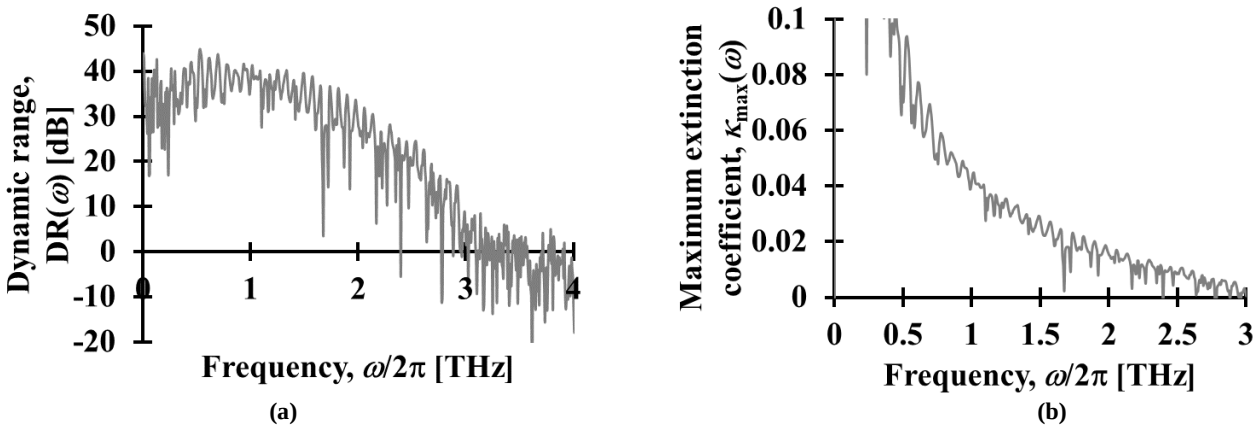

Figure 4.2: The frequency spectrum dynamic range and maximum extinction coefficient of THz TDS system two are shown in (a) and (b), respectively. The maximum extinction coefficient shown in (b) assumes a 5 mm thick sample.

The figure shows that for this specific THz TDS system, the frequency spectrum dynamic range is at least 30 dB between 300 GHz and 2.0 THz, with a maximum value near 45 dB at 500 GHz. This drops off quickly to the noise floor of the system around 3 THz. The corresponding maximum extinction coefficients that can be measured for a 5 mm thick sample are seen in Figure 4.2b. The maximum extinction coefficient decreases approximately with $1/\omega$ as expected and can be scaled linearly by changing the sample thickness. The etalon effects seen in both figures are due to internal reflections within the THz emitter and electro-optic crystal in the detection setup.

The minimum extinction coefficient that can be measured is related to the variance between measurement spectra. Ideally, taking several measurements of the same sample or background should produce identical results. This is not the case in practice, where seemingly identical measurements will produce slightly different magnitude spectra. When these amplitude spectra are divided, they will produce an amplitude spectrum ratio with an average magnitude that is slightly greater than or less than one and a non-negligible standard deviation, $\sigma(\omega)$. Interestingly, experimental measurements have found the magnitude of the standard deviation to be mostly independent of frequency providing the dynamic range is sufficiently large. Equation (4.4) can be modified to include the standard deviation in measured spectra to become

$$\kappa(\omega) = \ln\left[\left(\frac{t_{\text{in}}(\omega)t_{\text{out}}(\omega)E_0(\omega)}{E(\omega)} + \sigma(\omega)\right)\right]\frac{c}{\omega\delta}. \tag{4.6}$$

Now, when measuring a sample with very low extinction, the first term of the expression inside the natural logarithm in (4.6) approaches one. This allows the natural logarithm to be linearized providing a standard deviation in extinction coefficient

$$\sigma_{\kappa}(\omega) \approx t_{\text{in}}(\omega) t_{\text{out}}(\omega) \sigma(\omega) \frac{c}{\omega \delta}, \tag{4.7}$$

so long as the standard deviation of the amplitude spectrum ratio is much less than one. It must be emphasized here there is no single value for the minimum measurable extinction coefficient, but a noise floor that must be overcome. It is possible to take many measurements in an attempt to reduce this noise floor, though in most cases it is simply easier to make a thicker sample. Equation (4.7) assumes that the noise floor of the measurement system is well below both the signal and background spectra. The typical measurement standard deviations in the THz TDS systems used in this thesis were at least 0.05. This is shown in Figure 4.3, for two background measurements. The extinction coefficient corresponds to a sample with a 5 mm thickness.

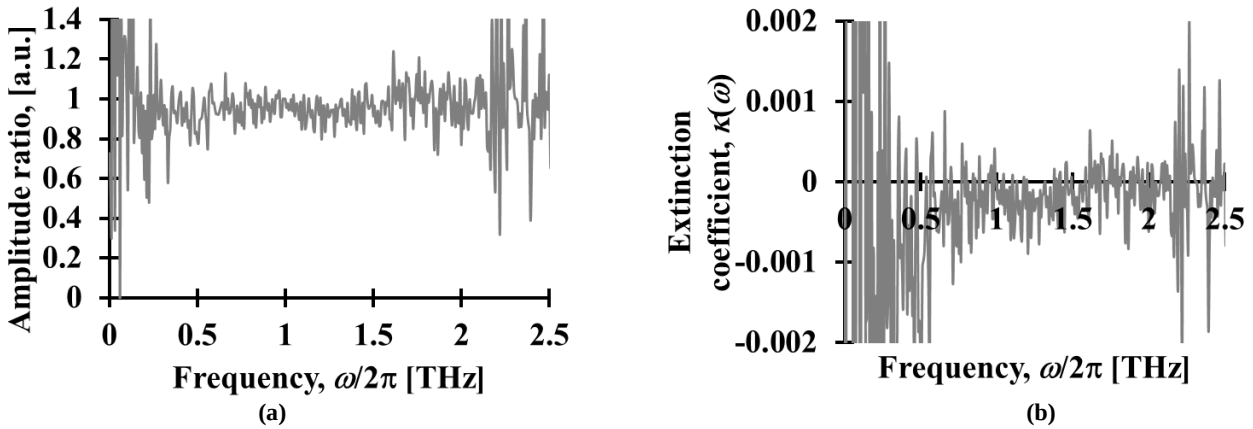

Figure 4.3: The amplitude spectrum ratio and extinction coefficient due to measurement standard deviation of THz TDS system two are shown in (a) and (b), respectively. The noise extinction coefficient in (b) assumes a 5 mm thick sample.

The results clearly show a mean amplitude spectrum ratio of less than one and a fairly significant standard deviation on the amplitude ratio. This standard deviation of the amplitude ratio, which appears to be fairly constant over THz frequency, was measured to be 0.081 between 500 GHz and 2 THz. Above 2 THz, water vapour spectral absorption lines and decreasing dynamic range cause the amplitude spectrum ratio to become noisy. The measured standard deviation in amplitude spectrum ratio corresponds to an extinction coefficient standard deviation of 0.8×10^{-3} at 1

THz. Compare this to the extinction spectrum shown in Figure 4.3b. The average measured extinction was slightly negative due to the mean amplitude spectrum ratio being less than one, and a had a standard deviation of 0.5×10^{-3} over a frequency range of 500 GHz to 2 THz. Remember that no sample was present in either of these measurements, so the extinction coefficient is entirely due to experimental error and noise.

The various THz TDS systems mentioned in this section will be applied in the remainder of this thesis to measure the performance of THz retroreflectors, modulators, and retromodulators. Each experiment will reference which of the systems from Figure 4.1 was used to capture its respective measurements. For material characterizations, the validity of the measured results will be discussed based on the limitations imposed by the extinction coefficient of particular samples. It should be noted that THz TDS scans must be run well beyond the point where the entire signal has passed. This allows for effects that would be evident in a CW THz testing system, such as standing waves and scattered reflections, to also be measured by the THz TDS system.

4.1 Cornercube Retroreflector

In this section, a cornercube retroreflector is fabricated and its incident angle efficiency and retroreflection efficiency are experimentally validated. The cornercube retroreflector was fabricated by machining a cornercube into a 25 mm diameter rod of aluminum as a holder. The internal surfaces of the cornercube were made of gold coated silicon wafers to ensure maximum reflectivity and surface flatness. The internal surfaces were cut using a laser milling machine (Oxford Lasers A-355) and bonded to the inner surfaces of the holder. An image of the completed retroreflector was shown previously in Figure 3.2d. An analysis of the incident angle efficiency was carried out by mounting the cornercube retroreflector at a fixed incident azimuthal angle and varying the incident polar angle in THz TDS system four. A THz TDS waveform was measured for each incident polar angle and was Fourier transformed into an amplitude spectrum. The signal strength at each incident azimuthal angle was the average of this amplitude spectrum over a THz frequency range of 300 GHz to 1 THz. The retroreflected signal was fairly weak due to the beamsplitting process and small retroreflection area, which resulted in a measurement bandwidth well below the true system bandwidth. A few representative spectra are shown in Figure 4.4a for various incident angles. The averaged amplitude at each incident polar angle was squared to convert to intensity, then

normalized with respect to the estimated value at normal incidence. These data points are finally plotted in Figure 4.4b along with the theoretical curve from Section 3.4.1. The error bars on each measured data point show the standard deviation of the measurements over the aforementioned frequency range.

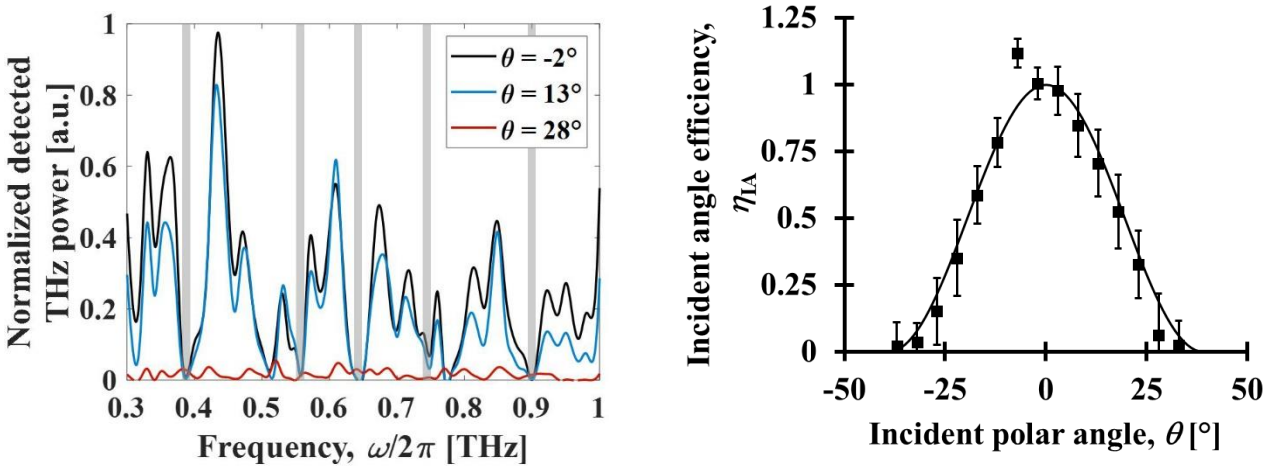

(a) (b)

Figure 4.4: Experimental results for the retroreflection performance of a cornercube retroreflector with triangular sides in the THz spectrum is shown. Three representative amplitude spectra of the normalized detected power are shown in (a) as a function of THz frequency. Experimental results for the incident angle efficiency, black squares, averaged between 300 GHz and 1 THz are shown in (b) along with the theoretical incident angle efficiency, solid line. The error bars correspond to the standard deviation over this frequency range.

Normalized detected THz power spectra for a few representative incident polar angles are shown in Figure 4.4a. While the results show spectral absorption peaks due to water vapour, around 380 GHz, 560 GHz, 650 GHz, 750 GHz, and 900 GHz, the results also show that the retroreflected signals along (θ = -2°) and near (θ = 13°) the optical axis are very similar, in contrast to the retroreflected signal far from (θ = 28°) the optical axis. The incident angle efficiency results are shown in Figure 4.4b with experimental data shown as black squares and the theoretical curve from Section 3.4.1 shown as the black line. These results show good agreement between the results of the ray tracing analysis and the experimental data. This is interesting since the wavelengths of the THz frequencies used to measure the incident angle efficiency in this experiment were only about an order of magnitude smaller than the cornercube side length, yet the ray analysis still produced an accurate model of the behaviour of this device indicating that diffraction is not a major loss mechanism over the distances used in this experiment. The outlier at θ = -7° is likely due to additional reflection off the holder. Clearly, the cornercube retroreflector is an efficient retroreflector near normal incidence, but its performance falters as the incident polar angle increases.

The retroreflection efficiency of the fabricated cornercube retroreflector was also investigated. Based on the holder diameter of 25 mm, the retroreflection area should be 1.35 cm^2 after considering that not all of the cornercube retroreflects. To experimentally validate this, a signal was measured from the cornercube retroreflector at normal incidence and compared to the reflection of an apertured flat mirror. The retroreflected signal from the cornercube was found to be equivalent to a flat mirror with an aperture area of 0.87 cm^2. While this equivalent area is somewhat lower than predicted, it is likely due to additional divergence introduced by the fact that the cornercube retroreflector's internal surfaces may not have been perfectly orthogonal or it may be due to diffraction off the edges of the internal surfaces. However, these results do confirm that only a portion of the cornercube retroreflector actually retroreflects the THz signal back to its source. The experimental retroreflection efficiency of the cornercube based on these measurements is $\eta_{re}(\omega) = 0.177$.

4.2 Spherical Retroreflector

In this section, the development of a spherical THz retroreflector is outlined. The first objective in developing a spherical THz retroreflector is to obtain a material with the correct refractive index. Since no pure material exists in the THz spectrum with a refractive index of 1.8, polymer composites are fabricated. The next objective is to ensure that the polymer composite has absorption in the THz spectrum. This will be accomplished by selecting the correct materials to use in the polymer composite. It is found that these materials are challenging to source, particularly the particles, making the fabrication of a spherical THz retroreflector impractical at this time.

4.2.1 Polymer Composites with Variable Refractive Indices

The first step to fabricating a spherical THz retroreflector using polymer composites is to ensure that these polymer composites can be made with the correct refractive index. This requires experimentation to fully understand the nuances of the effective medium theories used to predict the dielectric constant of composite materials given in Section 2.2.1.2. A series of experiments were carried out for polymer composites fabricated using PDMS as a host material and either Si or SiO_2 as the particles and are also summarized in [124]. These materials were chosen as the host and particles for a number of practical reasons. The host material was chosen to be PDMS (Sylgard 184), despite its large extinction coefficient, because its fabrication involves mixing two liquid components.

Consequently, the desired particles could be mixed with the polymer base while it was still a liquid allowing for uniform dispersion of the particles within the host. Then, curing agent could be added to solidify the polymer composite. The PDMS in these experiments was mixed at a 20:1 base-to-curing-agent ratio, degassed in a vacuum chamber for 30 minutes, and finally cured at room temperature for 48 hours. Prior work has shown that this process yields the lowest absorption in PDMS [29]. After curing, each sample was mounted as a free-standing slab for measurement in THz TDS system one. Silicon and SiO_2 were chosen as particles due to their commercial availability, assumed low absorption (though Si was later found to be highly absorbing), and their discrepancy in dielectric constant. The discrepancy in dielectric constant was particularly important as it was found that depolarization factor disproportionately affects composites with a large contrast between the host and particle dielectric constants. Nanoparticles and microparticles for both Si and SiO_2 were purchased from US Research Nanomaterials and were used as particles. Scanning electron microscope (SEM) images of the nanoparticles and microparticles are shown in Figure 4.5.

It can be seen from the SEM images in Figure 4.5 that some of the particles are roughly spherical, while others are highly irregular. The SiO_2 and Si nanoparticles are roughly spherical due to their synthesis via thermal processes allowing their surface energy to be minimized. The SiO_2 and Si microparticles are highly irregular due to their synthesis by mechanical disaggregation causing them to have broken into shards. The nanoparticles and microparticles shown in Figure 4.5 were used to fabricate composite samples with volumetric fractions of particles that spanned from zero up to the onset of agglomeration. Agglomeration was defined as the volumetric fraction above which the liquid mixture of PDMS and particles became a paste that could not be poured. This corresponded to volumetric fractions of 7%, 40%, 5%, and 30%, for SiO_2 nanoparticles, SiO_2 microparticles, Si nanoparticles, and Si microparticles, respectively. The onset of agglomeration at significantly lower volumetric fractions for nanoparticles is attributed to their high surface energy when compared to microparticles [125].

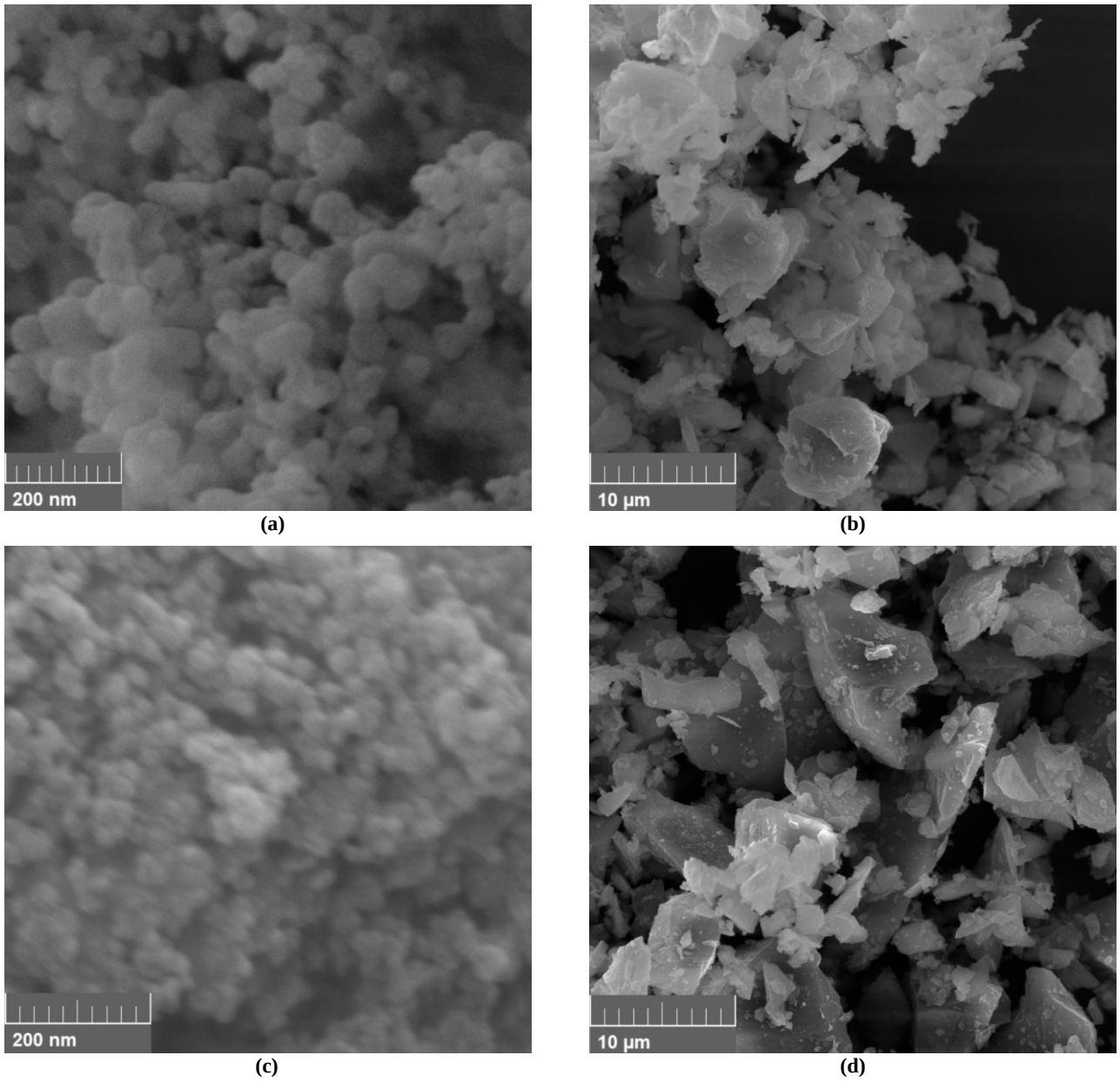

Figure 4.5: Representative SEM images of the (a) SiO_2 nanoparticles, (b) SiO_2 microparticles, (c) Si nanoparticles, and (d) Si microparticles. Adapted from [124], with the permission of AIP Publishing.

THz TDS system one was used to measure the refractive index and extinction coefficient of the PDMS composite samples. The results for a set of representative samples are plotted as a function of frequency in Figure 4.6. The results are shown for a representative nano-SiO_2, micro-SiO_2, nano-Si, and micro-Si composite with volumetric fractions of 6.4%, 25.9%, 4.8%, and 20.3%, respectively. The frequency range of 500 GHz to 1 THz was selected because it yields clear spectra for samples with all combinations of particle type, size, and volumetric fraction. The trends for both refractive index, Figure 4.6a, and extinction coefficient, Figure 4.6b, are primarily constant over the

displayed frequency range. The slight decrease in refractive index with increasing frequency for all samples in Figure 4.6a is attributed to the PDMS host [27], while the slight decrease in the extinction coefficient of the micro-Si composite with increasing frequency in Figure 4.6b is attributed to free carrier absorption, which can be quantified via the Drude model. Note that the small particles sizes of both the microparticles and nanoparticles result in negligible scattering losses in these composites.

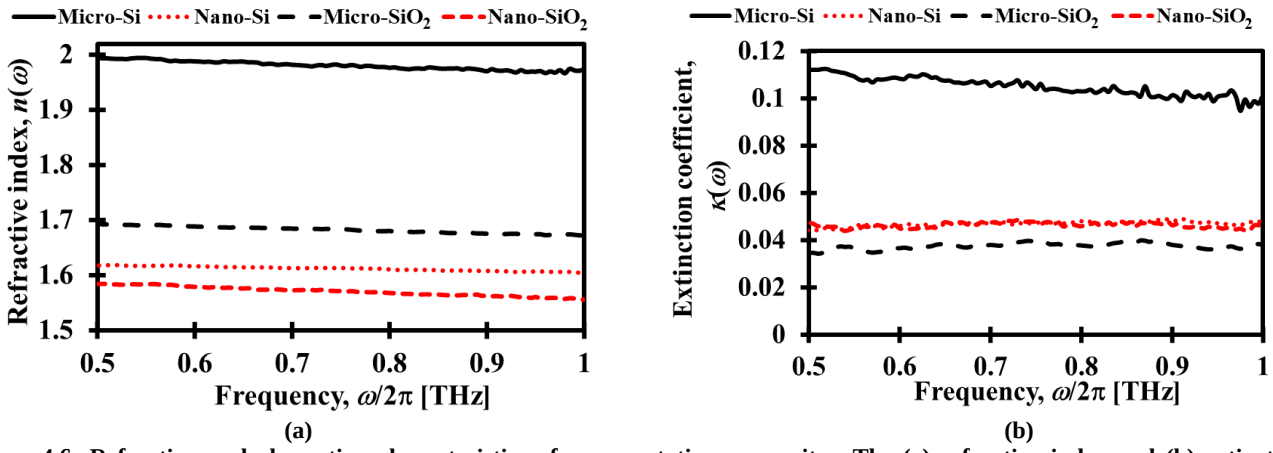

Figure 4.6: Refraction and absorption characteristics of representative composites. The (a) refractive index and (b) extinction coefficient is shown for a nano-SiO_2 composite with a volumetric fraction of V = 6.4% (short dashed red line), a micro-SiO_2 composite with a volumetric fraction of V = 25.9% (long dashed black line), a nano-Si composite with a volumetric fraction of V = 4.8% (dotted red line), and a micro-Si composite with a volumetric fraction of V = 20.3% (solid black line). Adapted from [124], with the permission of AIP Publishing.

The refraction and absorption characteristics for the composite samples are shown in Figure 4.7 as a function of volumetric fraction. Here, the displayed data points denote mean values across the frequency range of 500 GHz to 1 THz, and the displayed error bars show the root mean squared error in the measurements arising from inaccuracies in sample thickness and homogeneity. Error bars are only shown for the micro-Si and micro-SiO_2 composite data as the nano-Si and nano-SiO_2 composite data had error bars that were smaller than the markers. Experimental results for the refractive index, $n(\omega)$, and extinction coefficient, $\kappa(\omega)$, are shown in Figure 4.7a and Figure 4.7b for the nano-SiO_2 composites (as open red circles) and micro-SiO_2 composites (as solid black circles), respectively. Experimental results for the refractive index, $n(\omega)$, and extinction coefficient, $\kappa(\omega)$, are shown in Figure 4.7c and Figure 4.7d for the nano-Si composites (as open red circles) and micro-Si composites (as solid black circles), respectively. Theoretical results from the Bruggeman model are displayed in all the figures for the nano-SiO_2 and nano-Si composites (as solid red curves) and the micro-SiO_2 and micro-Si composites (as dashed black curves). The

theoretical results were generated by solving (2.1) for the complex dielectric constant of the composite, $\tilde{\varepsilon}_c(\omega)$, and computing its corresponding refractive index, $n(\omega)$, and extinction coefficient, $\kappa(\omega)$. The refractive index and extinction coefficient of PDMS used in the Bruggeman model were taken from the literature to be 1.55 and 0.045, respectively [27]. The refractive indices of SiO_2 and Si were taken from the literature to be 2.05, and 3.42, respectively [30]. Note that the refractive index of SiO_2 varies with crystallinity between 1.97 and 2.05, though the results given below validate the use of the higher value. The literature also gives extinction coefficients for SiO_2 and Si to be 2.8×10^{-4} and 2×10^{-4}, respectively [30]. However, these did not fit the experimental data so alternate values were used and the deviation from literature values will be discussed. All values for refractive index and extinction coefficient were taken to be independent of THz frequency over the measurement spectrum. The depolarization factor was used as a fitting parameter in all theoretical curves as discussed in Section 2.2.1.2. For the nanoparticle composites, the fitted depolarization factor was 1/3, which corroborates the spherical geometry of the nanoparticles seen in Figure 4.5a and Figure 4.5c. For the microparticle composites, the fitted depolarization factor was quite different at approximately 1/8. This corroborates the highly irregular geometry of the microparticles seen in Figure 4.5b and Figure 4.5d. The fitted depolarization factor was especially critical for the micro-Si composites due to the large difference in dielectric constant between the host and particles. These results show that the theoretical refractive index and extinction coefficient values for this much lower depolarization factor deviate significantly from theoretical values assuming spherical particles. An analysis was done using both a modified version of the Bruggeman model that incorporated elliptical particles and the Polder van Santen model. For both models, no ellipsoidal particle geometry was able to fit the experimental data for the micro-Si composites. Only by using the generalized Bruggeman model in (2.1) and allowing the depolarization factor to be a single, small value could the data be fit. This indicates that the highly irregular Si microparticles seen in Figure 4.6d cannot be approximated by ellipsoids. This was also true for the SiO_2 microparticles; however, the small dielectric contrast between the particles and the host mean that the theoretical curves have only minimal dependence on particle geometry. Each data point corresponds to the average refractive index or extinction coefficient spectrum between 500 GHz and 1 THz.

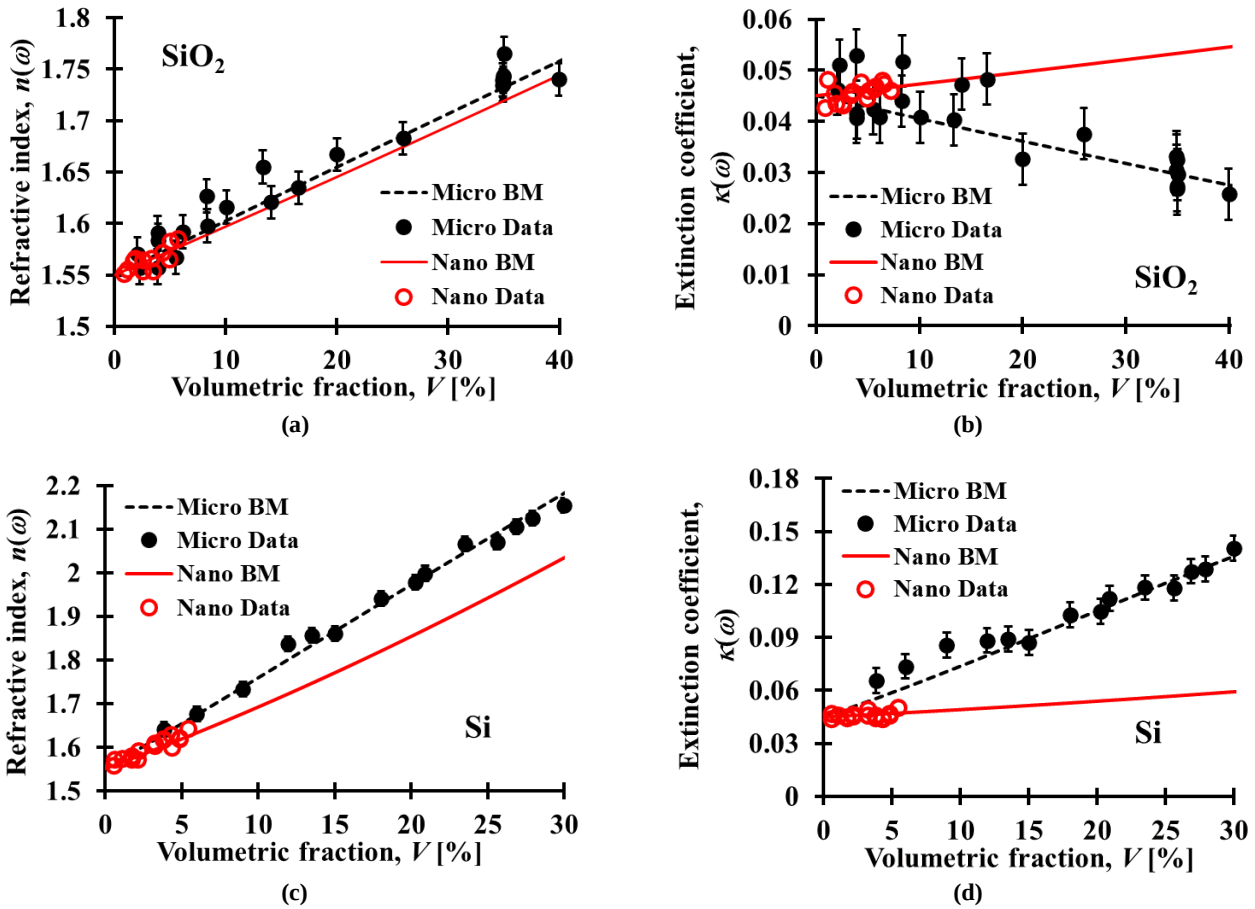

Figure 4.7: Refraction and absorption characteristics of composites comprised of SiO_2 and Si (roughly spherical) nanoparticles and (highly irregular) microparticles within a PDMS host. The experimental and theoretical results are shown for the (a) refractive index of the nano-SiO_2 and micro-SiO_2 composites, (b) extinction coefficient of the nano-SiO_2 and micro-SiO_2 composites, (c) refractive index of the nano-Si and micro-Si composites, and (d) extinction coefficient of the nano-Si and micro-Si composites. The experimental results for the nano-SiO2 and nano-Si composites are denoted by open red circles; the experimental results for the micro-SiO_2 and micro-Si composites are denoted by solid black circles. The theoretical results from the Bruggeman model for the nano-SiO_2 and nano-Si composites are denoted by dotted red curves, for a depolarization factor of N_d = 1/3; the theoretical results from the Bruggeman model for the micro-SiO_2 and micro-Si composites are denoted by dashed black curves, for a depolarization factor of N_d = 1/8. The displayed error bars correspond to the root mean squared error in the measurements arising from inaccuracies in sample thickness and homogeneity. Adapted from [124], with the permission of AIP Publishing.

Figure 4.7a shows theoretical and experimental results for the refractive index of the nano-SiO_2 and micro-SiO_2 composites. The experimental results show that increasing the content of SiO_2 increases the refractive index of the composite material as expected. The maximum refractive indices achievable before agglomeration are 1.61 for SiO_2 nano-SiO_2 composites and 1.75 for micro-SiO_2 composites. The theoretical results of the generalized Bruggeman model were obtained using the literature values for the refractive index of PDMS and SiO_2 and fit by varying the depolarization factor. A depolarization factor of 1/8 was used for the micro-SiO_2 composites and a depolarization factor of 1/3 was used for the nano-SiO_2 composites. With these depolarization factors, the theoretical fit shows

good agreement with the experimental results. These depolarization factors also agree with morphology of the particles seen in Figure 4.5. The results for the nano-SiO_2 and micro-SiO_2 composites show good agreement between the theory and experiment, with root mean squared errors of 0.008 and 0.016, respectively. Finally, the results suggest that depolarization is of little consequence in composites having a low dielectric contrast between the particles and host—as is the case for these SiO_2 nanoparticles and microparticles in PDMS.

Figure 4.7b shows theoretical and experimental results for the extinction coefficient of the nano-SiO_2 and micro-SiO_2 composites. The depolarization factors used in the theoretical fit are the same as for the SiO_2 refractive index, 1/8 for micro-SiO_2 composites and 1/3 for nano-SiO_2 composites. Here the results become less intuitive. Increasing the volumetric fraction of particles results in an increase in extinction coefficient for nano-SiO_2 composites, yet it also results in a decrease in extinction coefficient for micro-SiO_2 composites. This indicates that the SiO_2 microparticles have a lower extinction coefficient than the PDMS, while the SiO_2 nanoparticles have a higher extinction coefficient than PDMS. More interestingly, neither of the fitted extinction coefficients of 0.005 for microparticles and 0.07 for nanoparticles match the extinction coefficient of 2.8×10^{-4} given for quartz in the literature. Looking back at Table 2.3, the SiO_2 microparticle extinction coefficient falls within the range of known values for fused silica. Therefore, it can be assumed that the SiO_2 particles used in this work are not pure quartz, but rather fused silica. The nanoparticle extinction coefficient is much too high to be either quartz or fused silica. Interestingly though, others have noted that nanoparticles have anomalous extinction coefficients due to their especially high surface-to-volume ratio [126]. This dense manifold of surface states can exhibit absorption well beyond that of crystalline or amorphous bulk materials. With the correctly fitted values for extinction coefficient, the results for the nano-SiO_2 and micro-SiO_2 composites show decent agreement between the theory and experiment, with root mean squared errors of 0.002 and 0.005, respectively.

Figure 4.7c shows theoretical and experimental results for the refractive index of the nano-Si and micro-Si composites. The experimental results show that increasing the content of Si increases the refractive index of the composite material as expected. The maximum refractive indices achievable before agglomeration are 1.65 for nano-Si composites and 2.2 for micro-Si composites. The refractive index of 2.2 for micro-Si composites is

particularly encouraging as it shows that composite materials can achieve predictable refractive indices around 1.8, which is required for spherical THz retroreflectors. As with the previous figures, the depolarization factors used in the theoretical fits are 1/8 for micro-Si composites and 1/3 for nano-Si composites. The fact that these depolarization factors are identical to the SiO_2 depolarization factors is a satisfying finding seeing as the morphologies of the micro and nanoparticles are the same for both materials in Figure 4.5. However, unlike the micro-SiO_2 and nano-SiO_2 composites, it is seen that the differing depolarization factors of the nanoparticles and microparticles yield a significant difference in the refractive index. Figure 4.7c shows the dotted red curve for the nano-Si composites is well below the dashed black curve for the micro-Si composites. This suggests that depolarization is a noteworthy consideration in composites having a high dielectric contrast between the particles and host—as is the case for these Si nanoparticles and microparticles in PDMS. Overall, the results for the nano-Si and micro-Si composites show good agreement between the theory and experiment, with root mean squared errors of 0.013 for the nano-Si composites and 0.017 for the micro-Si composites.

Figure 4.7d shows theoretical and experimental results for the extinction coefficient of the nano-Si and micro-Si composites. The depolarization factors used in the theoretical fit are the same as for the Si refractive index, 1/8 for micro-Si composites and 1/3 for nano-Si composites. Like with the SiO_2 composites, interpreting the extinction coefficient data for Si composites is nuanced. The extinction coefficients for both the nano-Si and micro-Si composites rise with increasing volumetric fraction of particles. This is counterintuitive since the extinction of Si is virtually zero in the literature and there is a large discrepancy between the fitted extinction coefficients for the nano-Si and micro-Si composites. The extinction coefficient for the micro-Si composites is approximately 0.3, which is orders of magnitude larger than the 2×10^{-4} noted in the literature for intrinsic silicon. It will be shown in Section 4.2.3 that the extinction present in the Si microparticles is due to significant Drude free carrier absorption. The measured extinction coefficient for the Si nanoparticles is somewhat lower than for Si microparticles at 0.1. The larger extinction coefficient in the case of the Si nanoparticles than what is expected from intrinsic Si is attributed to the especially high surface-to-volume ratio found in nanoparticles [126], which alters the extinction coefficient. Interestingly, the extinction coefficient measured for the Si nanoparticles is quite similar to the extinction coefficient

measured for the SiO_2 nanoparticles, lending credence to the hypothesis that the elevated extinction in both cases is due to particle size effects. Unfortunately, the low volumetric fraction limitation of nano-Si composites makes it difficult to discern if Drude-like losses appear in the extinction coefficient spectrum, as this spectrum is dominated by the extinction of PDMS. Ultimately, the results for the nano-Si and micro-Si composites show good agreement between the theory and experiment, with root mean squared errors of 0.002 for the nano-Si composites and 0.007 for the micro-Si composites.

The results from this analysis are promising, but significant improvements to the composite materials are required before implementation as a spherical retroreflector. There are two promising findings. First, the refractive index modelling used in this set of experiments provides very good agreement with the experimental data, and the error in the refractive indices is small. This indicates that a composite material with a predictable refractive index could be fabricated using the method from these experiments. Second, refractive indices around 1.8, the ideal refractive indices for spherical retroreflectors in the THz spectrum, were demonstrated using micro-Si composites. This indicates that polymer composites are a potential material candidate for spherical THz retroreflectors. However, these experiments also uncovered one significant challenge, extinction coefficient. A spherical THz retroreflector requires an extinction coefficient on the order of 3×10^{-3} or less to prevent excessive material loss in the sphere. Disappointingly, the only material that comes close to meeting that criteria is the SiO_2 microparticles, yet the micro-SiO_2 composites were limited to refractive indices below 1.75 due to agglomeration, and still had high extinction due to the PDMS. The large, unpredictable extinction coefficient of the nanoparticles show that any eventual composites should be fabricated using microparticles with low extinction. The next section will look at potential candidate host and particle materials for low-loss THz composites.

4.2.2 Low-loss Host Materials

The large measured extinction coefficients in the previous set of experiments can be primarily attributed to the high extinction coefficient of the PDMS host material. By replacing PDMS with a lower loss material, the overall loss of the composite can be reduced significantly. However, most low-loss polymers in the THz range are challenging materials to make into a liquid form so that they can be mixed with particles to form a composite. Strictly from an

extinction coefficient perspective, the two materials that hold the most promise to serve as a host in THz composites are HDPE and COC. Both materials have refractive indices near 1.5 and extinction coefficients below 3×10^{-3} for frequencies up to 1 THz. However, both materials are solid at room temperature so mixing them with particles is challenging. Nonetheless, two methods were explored in an attempt to mix these polymers with microparticles. The first method was to chemically dissolve the polymers using a solvent. Once dissolved, the polymers could be easily mixed with particles and the solvent could be left to evaporate out of the composite. The second method was to find polymer microparticles that could be dry mixed with the semiconductor or oxide microparticles creating a powder mixture. Then, using a hot press, the powder mixture could be fused into a solid sample. The following sections will discuss these two methods in detail.

The first method, chemical dissolution, was tested for COC since it dissolves in some common non-polar solvents. In this case, toluene was used as the solvent. This method of dissolving COC in toluene has been used in the literature to create a liquid form of COC that could be spin coated in microfabrication applications [127]. A mixture of toluene and COC pellets was prepared and poured into several molds to produce pure COC samples for spectroscopy. The molds were heated to evaporate the toluene leaving behind only COC. This however proved challenging as the toluene was slow to evaporate and left voids in thicker samples due to the large amount of toluene required to dissolve the COC pellets. The most uniform samples were those poured onto a large flat surface creating samples that were around 1 mm thick. This low thickness introduces significant noise into any measured extinction coefficients. To obtain thicker samples, an injection molding machine was used to make discs that were 2-3 mm thick. Two samples were made and measured using THz TDS. The first was a thinner sample made from dissolved COC with a thickness of 1.5 mm and the second was a thicker sample fabricated using injection molding with a thickness of 2.2 mm. The spectroscopy results for both the thin samples, solid black lines, and thick samples, dashed red lines, are shown in Figure 4.8. The refractive indices are shown in Figure 4.8a and the extinction coefficients are shown in Figure 4.8b.

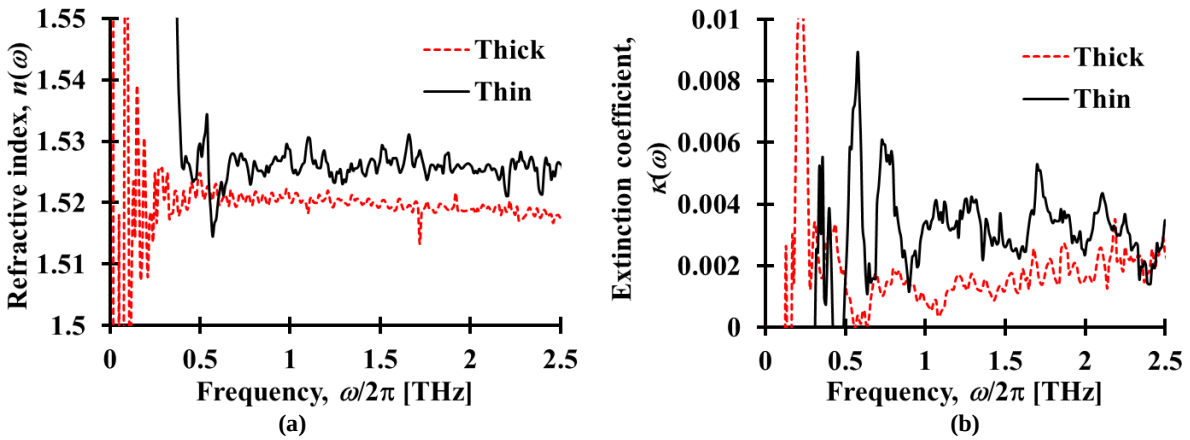

Figure 4.8: The refractive index (a) and extinction coefficient (b) of thick and thin COC samples are shown. The thick sample was injection molded, and its data is shown as the red dashed lines. The thin sample was dissolved and poured, and its data is shown as solid black lines.

The results confirm that COC does indeed have very low extinction and a similar refractive index to other polymers. The measured refractive index is around 1.52 for the injection molded sample and closer to 1.53 for the dissolved sample, which agrees with literature values [128]. The slightly lower refractive index seen for the injection molded sample may have been due to small gas voids trapped within the sample, which were commonly present when injection molding. These voids resulted both from air being mixed into the molten COC during injection and off-gassing of the COC when heated. While noisy, the extinction spectra for both samples are very promising. The injection molded sample had a slightly lower extinction coefficient around 2×10^{-3}, while the dissolved sample had an extinction coefficient of about 4×10^{-3}. Both of these values fall around the target extinction coefficient for spherical retroreflectors of 3×10^{-3}. Equation (4.7) indicates that thinner samples will have a higher extinction coefficient noise floor, which is seen in these results. Unfortunately, both fabrication methods do not lend themselves well to creating thick composite materials. Creating a thick piece of COC would be technically possible by pouring many layers of dissolved COC, although this method would be slow, and each additional layer may inject toluene solvent into the layers below. On the other hand, the injection molding machine had poor reproducibility and was extremely difficult to clean making it a poor candidate for fabricating small runs of polymer composites at varying refractive indices. Additionally, composite pellets would need to be prefabricated and fed into the injection molding machine, which does not solve the mixing challenge.

Before moving on from COC, two composite samples were fabricated using microparticles in dissolved COC. These samples were poured as thin sheets and measured using THz TDS to determine if the process is feasible for future application requiring thin layers. Since the dissolving and curing process is rather arduous, only one high volumetric fraction was fabricated for each of the Si and SiO_2 microparticles used in the previous set of experiments. The micro-Si composite sample was 0.52 mm thick and had a volumetric fraction of 21%. The micro-SiO_2 composite sample was 0.94 mm thick and had a volumetric fraction of 34%. The THz TDS results are shown in Figure 4.9 with the refractive index in Figure 4.9a and the extinction coefficient in Figure 4.9b. The micro-Si composites are shown as black dashed line and the micro-SiO_2 composites are shown as the solid red lines.

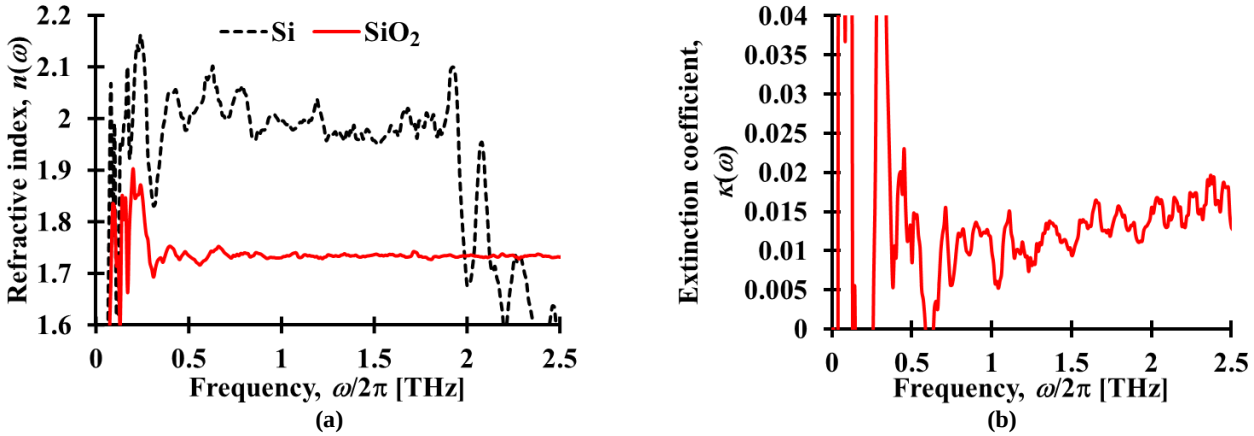

Figure 4.9: The refractive index (a) and extinction coefficient (b) of two COC composite materials are shown. The first sample was made using Si microparticles, shown as the dashed black line. The extinction coefficient of this sample was so high that it is not shown here. The second sample was made using SiO_2 microparticles and its data is shown using the solid red lines. Both samples were dissolved in toluene and poured into thin sheets.

The results show that thin composite materials with a tunable refractive index are indeed possible to fabricate using dissolved COC. The average refractive index of the composite fabricated using silicon microparticles was an impressive 2.0 around 1 THz. However, these silicon microparticles were the same ones used in the PDMS composite experiments and had very high extinction due to Drude losses. This high extinction degraded the SNR of the measurements introducing significant error in the refractive index. The average extinction coefficient between 500 GHz and 1.5 THz was approximately 0.16, which is extremely high, and so it was not plotted in Figure 4.9b. The results for composites fabricated using SiO_2 show somewhat more promising results. A much more constant refractive index of 1.73 was measured over a bandwidth of 500 GHz to 2.5 THz. However, the extinction coefficient

was much higher than anticipated at 1.2×10^{-2}, which surpasses the extinction coefficient of both the COC measured in this section and the SiO_2 microparticles measured in the previous section. Again, the thin sample introduces the possibility that this high extinction coefficient is simply due to measurement noise according to (4.7). In summary, an experimental demonstration of COC composite materials with tunable refractive indices was carried out. These composite sheets could have future applications in multilayer structures such as dielectric mirrors or filters.

The second method, dry mixing, was tested for HDPE as it was reasonable to find HDPE microparticles. This method has been demonstrated to be effective by several other groups in the literature [19], [89]. Two different grades of HDPE were used. The first was an ultra-high molecular weight polyethylene (UHMWPE) powder with a particle diameter of approximately 45 μm. The second was an HDPE wax with a particle diameter of approximately 4 μm. The two powders had fairly different thermal properties and so needed to be pressed at different temperatures and pressures. The HDPE wax was much softer and required pressing at 83°C under less than 10 MPa of pressure. It was found that pressing the HDPE wax for an extended period of time (>30 minutes) was required for the powder to fully fuse into a solid sample. The UHMWPE was much more mechanically robust and required pressing at 155°C under 20 MPa of pressure. Again, it was found that pressing these samples for an extended period of time was necessary for the samples to fully fuse. The first test of both materials was to fabricate pure samples (i.e., no particles) to verify their low extinction when using this method. Figure 4.10 below shows THz TDS spectroscopy results using system two for both pure HDPE wax, red dashed line, and pure UHMWPE, solid black lines, samples. The refractive index for both samples is shown in Figure 4.10a and the extinction coefficient is shown in Figure 4.10b.

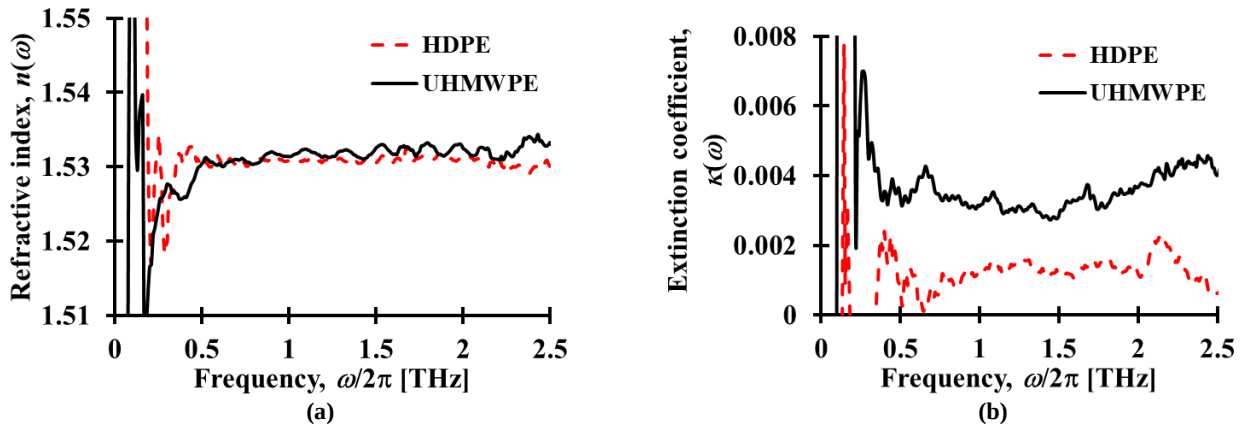

Figure 4.10: The refractive index (a) and extinction coefficient (b) of HDPE wax and UHMWPE are shown as a function of THz frequency. The HDPE wax data is shown as red dashed lines and the UHMWPE data is shown as solid black lines.

The results confirm that both forms of polyethylene are viable host materials for low-loss THz composites. Both materials have a refractive index of 1.53, which is common for polymers and agrees with the literature [129]. The refractive index is also virtually constant over a THz frequency range of 500 GHz to 2.5 THz. The more critical parameter that qualifies these two polymers as viable THz spherical retroreflector candidates is their low extinction. The UHMWPE sample had an average extinction coefficient of 3.5×10^{-3}, while the HDPE wax had an even lower extinction coefficient of 1.3×10^{-3}. There is one other point about the measured data that is worth mentioning related to repeatability. While only one representative sample is shown in Figure 4.10 for each polymer, many samples were fabricated and tested. The extinction coefficient for all samples was within about ±50% of the measurements shown here, due to fabrication inconsistencies as well as experimental noise. Nonetheless, the measured extinction coefficients are still low enough to conclude that these polymers are suitable composite hosts. The refractive index for both polymers deviated by up to ±0.01. Many measurements of the same sample do not show this level of deviation, especially for the refractive index. The deviations between samples are likely due to the fabrication procedure itself, which will be discussed presently. It has also been well established that the refraction and extinction properties of many materials in the THz frequency spectrum change with microscopic material structure, i.e., crystallinity, which will be discussed in the next section. Regardless, pressed polyethylene powders are viable host materials for low-loss THz composites and their use will be explored further.

The hot-pressing procedure to fabricate the polymer samples used in this work had a significant effect on the measured extinction coefficient, especially for composite samples. To investigate the effects of hot-pressing procedure on extinction coefficient, micro-SiO_2 composite samples were fabricated using the same SiO_2 microparticles used in the PDMS composites. Two sets of samples were made, one with UHMWPE as the host polymer and one with HDPE wax as the host polymer. Both sample sets were made for volumetric fractions up to 25% and were modelled using the Bruggeman model with a depolarization factor of 1/8. To ensure that the fabrication process did not have an effect on refractive index, results for the refractive index for both sets of polymer composites are given in Figure 4.11. The refractive index is shown for HDPE wax composites in Figure 4.11a and UHMWPE composites Figure 4.11b. All data points were obtained by averaging the measured refractive index and extinction spectra between 500 GHz and 1.5 THz.

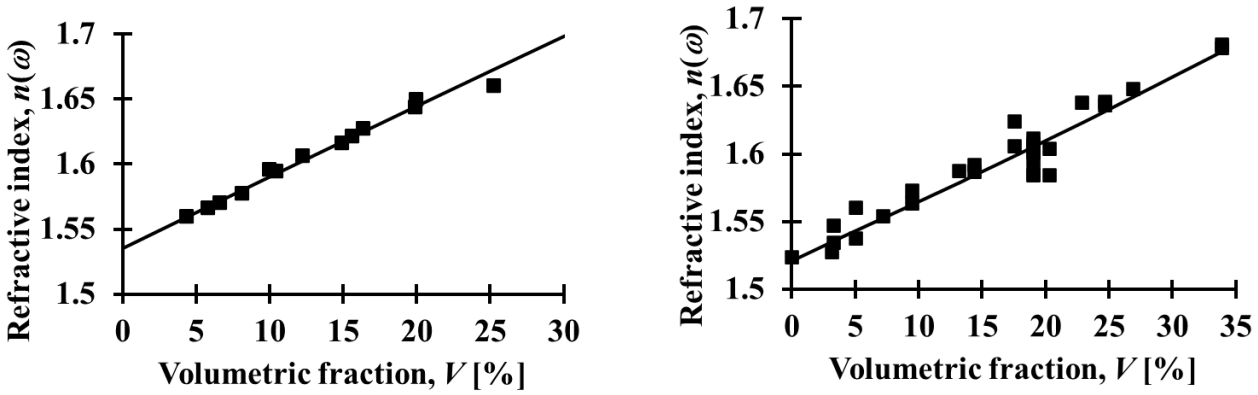

Figure 4.11: The refractive indices of composite materials comprised of SiO_2 microparticles and HDPE wax (a) or UHMWPE (b) as the host are shown as a function of volumetric fraction. All composites were fabricated by hot pressing a dry mixture of host particles and microparticles.

The refractive index results show that these composites behave as the Bruggeman model predicts. There were a few discrepancies in the parameters used to fit these data sets to the Bruggeman model, however. The first discrepancy is the refractive index of the polyethylene, which was 1.54 for the HDPE wax and 1.52 for the UHMWPE, which deviate from their previously measured value of 1.53. These minor deviations were common between background samples for not only the polyethylene powders, but also for PDMS. The other discrepancy is that the fitted refractive index for SiO_2 in the UHMWPE results is 2.0, which is lower than the 2.04 measured previously with PDMS. This could be due to inaccuracies in the PDMS measurements or the fact that the UHMWPE host particles are much

larger than the SiO_2 particles causing the SiO_2 to cluster in roughly spherical groups. Setting the depolarization factor of the particles in the UHMWPE results to 1/3, which correspond to spherical particles, produces a fitted SiO_2 refractive index of 2.04. Nonetheless, the measured refractive indices agree well with the Bruggeman model, especially for the HDPE wax samples. However, the measured extinction coefficients show a significant dependence on fabrication procedure. Several extinction coefficient spectra are shown in Figure 4.12 for HDPE wax composites of varying volumetric fractions. These samples were all pressed for the same time at the same temperature.

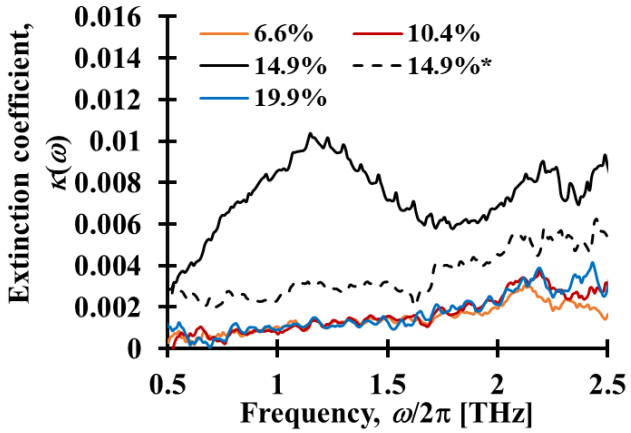

Figure 4.12: The extinction coefficient for HDPE SiO_2 composites is shown as a function of frequency for various volumetric fractions. The volumetric fractions are: 6.6% (orange line), 10.4% (red line), 14.9% (solid black line), and 19.9% (blue line). The sample with a volumetric fraction of 14.9%* was re-pressed and the extinction coefficient after re-pressing is shown as the dashed black line.

There are several interesting insights into hot pressing polymer composites from this set of results. First, three of the four samples had virtually identical extinction coefficient spectra, which indicates that the extinction coefficient of the SiO_2 microparticles is similar to that of the HDPE wax. The extinction coefficient was estimated to be around 0.005 in the PDMS results, though the large extinction in PDMS made this result unreliable. Here, the extinction is clearly shown to be on the order of 0.001 depending on THz frequency. This is promising for the fabrication of low-loss composite materials in the THz spectrum for refractive indices below 1.65. Second, there is an obvious deviation in measured extinction spectrum for the sample with a volumetric fraction of 14.9%. The measured extinction coefficient for this sample was nearly an order of magnitude larger than the other samples. Since this sample does not have the highest volumetric fraction, it can be concluded that this unexpectedly high extinction spectrum is not due to the material properties of the particles. It was found that this sample was improperly pressed

during fabrication leaving air voids in the sample. This was evidenced by both obvious visual discrepancies between this sample and the others, as well as a lower measured refractive index. Air voids, which typically are concentrated near the centre of the sample, result in differing propagation times for various portions of the measurement TDS pulse. This discrepancy causes interference in the measured signal, which manifests as higher loss after parameter extraction. Consequently, this sample was re-pressed, and its results are shown as the black dashed line in Figure 4.12. It can be clearly seen that re-pressing the sample reduced the extinction coefficient dramatically, though not low enough to conform with the other samples that were pressed correctly. In addition, the refractive index of the re-pressed sample increased giving it better agreement with predictions by the Bruggeman model. This indicates that the second pressing removed most of the air from the sample, though some manufacturing imperfections remain.

There was also an attempt made to fabricate HDPE wax micro-SiO_2 composites with very large volumetric fractions of SiO_2 microparticles. These samples were pressed for an additional hour to ensure heat was transferred through the entire material. The extinction coefficient results for these composites are shown in Figure 4.13 along with the previous result with 19.9% volumetric fraction for comparison.

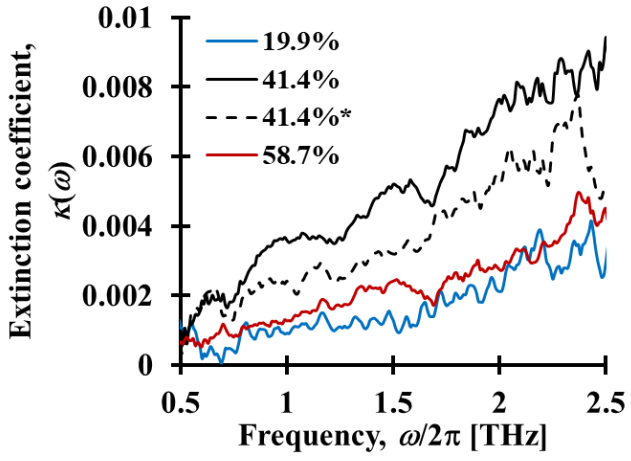

Figure 4.13: The extinction coefficient for HDPE SiO_2 composites is shown as a function of frequency for various volumetric fractions. The volumetric fractions are: 19.9% (blue line), 41.4% (solid black line), and 58.7% (red line). The sample with a volumetric fraction of 41.4% was re-pressed and the extinction coefficient after re-pressing is shown as the dashed black line.

The results for the extinction coefficient spectra of high volumetric fractions of SiO_2 in HDPE wax are encouraging. The sample with 41.4% volumetric fraction, denoted by the solid black line, shows modest extinction that was again due to improper pressing. This was partially remedied by re-pressing the sample, denoted by the dashed black line, bringing the extinction down by about 25%. The sample with 58.7% volumetric fraction, denoted by the red line, shows similar extinction to the 19.9% volumetric fraction sample, denoted by the blue line, indicating that this sample was properly pressed. Disappointingly, both of the high volumetric fraction samples had significant error in their refractive indices. The measured refractive indices for the 41.4% sample after re-pressing and 58.7% sample were 1.68 and 1.64, respectively. However, the Bruggeman model expects these refractive indices to be 1.74 and 1.83, respectively. While the source of this discrepancy was not fully explored, one possibility is that there is still air trapped in the sample between the SiO_2 particles. For lower volumetric fractions, the HDPE host particles all make contact with each other and will deform to fill any air voids when pressed. However, for high volumetric fractions, there may be clusters of SiO_2 particles that do not deform to fill voids under pressure. These clusters may be too large for the HDPE to deform into; thus, air voids remain in the sample despite the application of significant pressure during fabrication.

Overall, these results show that dry mixing and hot-pressing polyethylene powder is a viable method of fabricating polymer composites for THz applications. Special care must be taken to ensure that samples are correctly pressed and heated to minimize extinction coefficient, and the maximum volumetric fraction is limited to approximately 30% due to challenges pressing all the air out of the composite material. Micro-SiO_2 composites with extinction coefficients below 0.003 were successfully demonstrated. Unfortunately, a refractive index of 1.8 is not practical using SiO_2 microparticles due to the large required volumetric fraction, so an alternative particle must be sought.

4.2.3 Low-loss Particle Materials

To fabricate a spherical THz retroreflector, composite materials can be used so long as both the host and particle materials are low loss. The previous section indicated that polyethylene powders are a viable option for a host material, yet the SiO_2 microparticles used did not have a high enough refractive index for the composite materials to achieve a refractive index of 1.8. Therefore, the next task is to identify candidate materials to serve as particles.

These particles should have a high refractive index, ideally greater than 3.0, and similarly low loss to what is seen in polyethylene. Based on extinction coefficients published in the literature, there are two prospective particles: HRFZ Si, and Al_2O_3 (alumina). The HRFZ Si is similar to the Si microparticles used in the PDMS experiments, but with negligible Drude losses. Unfortunately, this material cannot be purchased in microparticle form, so a small batch was custom milled for preliminary experiments. The other potential candidate material is alumina, which has a refractive index of 3.2 and an extinction coefficient of 3×10^{-3} [30]. Spherical alumina microparticles were purchased with an average particle size of 0.8 μm from US Research Nanomaterials. Like with the SiO_2 and Si microparticles, these alumina microparticles are small enough that scattering losses will be negligible.

Similar to the host polymers, there are a few considerations to take into account when choosing particles for THz polymer composites. The first consideration that will be explored is particle crystallinity. The challenge so far when calculating material loss is the inability to accurately measure the particle extinction coefficients separately from the host polymer. This means that the values inserted into the Bruggeman model are typically from the literature. The issue with this method is that the literature tests large slabs of crystalline material [30], and not potentially polycrystalline or amorphous microparticles. The micro-SiO_2 composite extinction results have already shown that the fitted values for microparticles can be an order of magnitude different than the crystalline material extinction and conform more so to polycrystalline or amorphous material properties. The alumina microparticles to be used shortly in HDPE micro-Al_2O_3 composites were fabricated using a high temperature melt process to produce the spherical microparticles in liquid phase before they cooled into solid microparticles. This rapid heating and cooling likely resulted in the crystal structure of the alumina being polycrystalline with different material properties than those measured for crystalline alumina. It has been well established that solids with a lower degree of crystallinity tend to have much higher extinction in the THz spectrum than their perfectly crystalline counterparts [25]. The power absorption coefficient for various amorphous solids was shown decades ago to be approximately calculable using

$$n(\omega)\alpha(\omega) = k_\alpha(\hbar\omega)^\beta, \tag{4.8}$$

where k_α is a scaling constant and β is equal to two for most materials including oxides (though slightly less for other materials such as polymers) [25]. This simple calculation assumes that defect states in the crystalline structure give rise to the approximately quadratic relationship between photon energy ($\hbar\omega$) and power absorption. This relationship has been observed in other, more recent THz characterizations of polycrystalline and amorphous materials [32], [130].

To investigate the crystallinity of the spherical alumina microparticles used in this work, several composite materials were fabricated using these alumina microparticles in HDPE wax as a host. The THz refraction and extinction characteristics of these composites were tested in THz TDS system three. The results are shown in Figure 4.14. Each data point corresponds to the measured value at 1 THz.

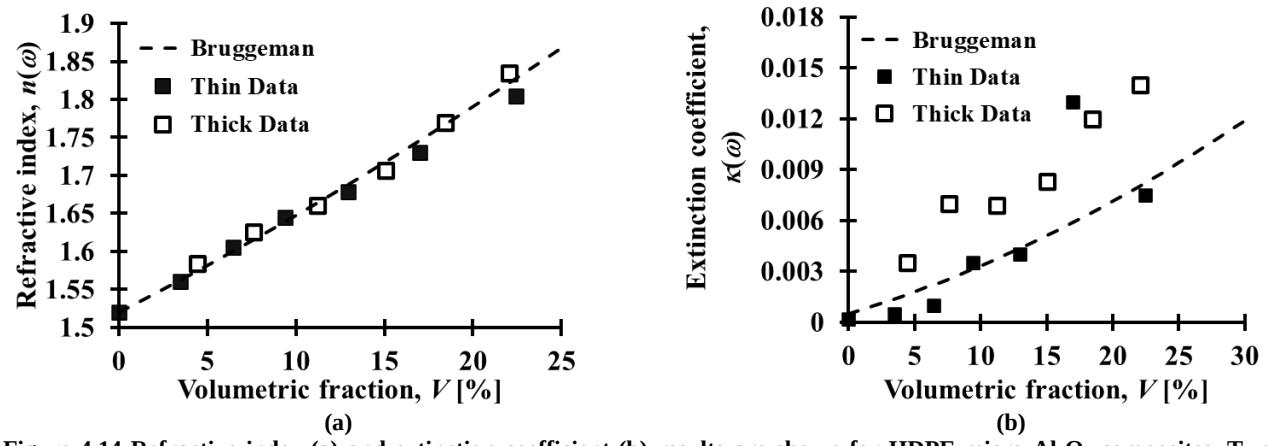

Figure 4.14 Refractive index (a) and extinction coefficient (b) results are shown for HDPE micro-Al_2O_3 composites. Two sets of samples, thick and thin, were fabricated. The thick samples are denoted by the hollow squares and the thin samples are denoted by the solid squares. A theoretical fit using the Bruggeman model is shown as the dashed line.

The figure shows results for two sets of data, which correspond to a set of thin samples (solid black squares) and a set of thick samples (hollow black squares). It is apparent from the results that the measured refractive index is entirely independent of the sample thickness, with both sets of samples agreeing well with the Bruggeman model for spherical particles, i.e., a depolarization factor of 1/3 (dashed line). The extinction coefficient for each set of data shows two distinct effects. First, the extinction coefficients of the thick samples are approximately double that of the thin samples indicating that the thick samples were improperly pressed. Their increased volume likely required longer pressing times to allow heat to penetrate into the sample. Interestingly, this has no effect on

refractive index, likely due to the fact that improper pressing results in scattering losses. Secondly, the extinction coefficient of the thinner samples, which are assumed to have been pressed correctly, is indicative of an extinction coefficient of 0.04, which is an order of magnitude larger than reported literature values for crystalline alumina [30].

To determine if this higher extinction coefficient is due to the alumina microparticles being polycrystalline, the measured extinction coefficients for three samples with volumetric fractions of 3.5%, 9.4%, and 22.4% are plotted in Figure 4.15. The measured extinction spectra were fitted with a Bruggeman model where the extinction coefficient of the alumina microparticles was assumed to follow (4.8) with $\beta = 2$ and $n(\omega) = 3.16$. The constant k_α was taken to be a fitting parameter and the power absorption coefficient was converted to an extinction coefficient. The extinction coefficient for HDPE wax was taken from a blank sample with a volumetric fraction of 0%. All samples were between 2 mm and 3 mm thick. The results are shown for frequencies above 0.5 THz as the noise floor in the measured extinction coefficient becomes large below this frequency.

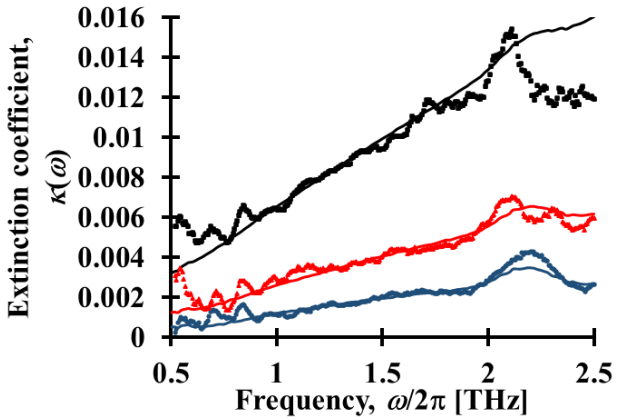

Figure 4.15: The theoretical and experimental extinction coefficients for the thin HDPE micro-Al_2O_3 composites are plotted as a function of THz frequency. Experimental data for composites with volumetric fractions of 3.5%, blue circles, 9.4%, red triangles, and 22.4%, black squares, is shown. This experimental data is fit with Bruggeman curves for volumetric fractions of 3.5%, blue line, 9.4%, red line, and 22.4%, black line.

The fitted extinction coefficient spectra agree well with the measured extinction coefficient spectra for THz frequencies between 500 GHz and 2 THz indicating that the quadratic relationship between frequency and power absorption coefficient is valid for polycrystalline alumina. The fitted constant k_α was approximately equal to 1×10^{46} $J^{-2}m^{-1}$, which is an order of magnitude greater than what was found for SiO_2 in [25]. Consider though that crystalline

SiO_2 has an extinction coefficient that is about an order of magnitude lower than crystalline alumina [30], and this result is very reasonable. Other groups have also fabricated micro-Al_2O_3 composites and reported the power absorption coefficient. Headland *et al*. fabricated micro-Al_2O_3 composites using PDMS as a host [90]. They found that the extinction coefficient of their micro-Al_2O_3 composites was virtually independent of the volumetric fraction of alumina indicating that the alumina microparticles used in their work has a very similar extinction coefficient to PDMS. They measured an average extinction coefficient of 0.043 over a frequency range of 300 GHz to 1 THz for their composites, which had volumetric fractions up to 9%. This agrees well with the extinction coefficients measured in this work of 0.045 for PDMS and 0.04 for alumina at 1 THz. Consequently, it can be concluded that the alumina microparticles used in this work are polycrystalline, and therefore have higher extinction then their crystalline counterparts.

Overall, the alumina composites could reach a refractive index of 1.8 with an extinction coefficient significantly lower than any seen in the PDMS composites. In particular, one of the thinner samples had a refractive index of about 1.8 and an extinction coefficient of 7×10^{-3}. While the extinction is somewhat larger than originally hoped, it is only about a factor of two greater and shows promise to fabricate THz spherical retroreflectors at lower frequencies.

The second consideration when choosing particles is free carrier density. As was seen in the PDMS micro-Si composite results, the free carrier density of the microparticles was catastrophic for extinction. To verify that these losses follow the Drude model, an HDPE wax composite sample was made with a very low concentration of the low resistivity silicon used in the PDMS composite experiments. The measured extinction coefficient of this composite was fitted using the Bruggeman model with experimental data for the HDPE wax dielectric constant and the Drude model for the particle dielectric constant. Figure 4.16 shows the extinction spectrum of a representative sample with 0.96% volumetric fraction of low resistivity silicon. The red squares are the experimentally measured extinction coefficient, while the black line is the theoretical fit using the Bruggeman model.

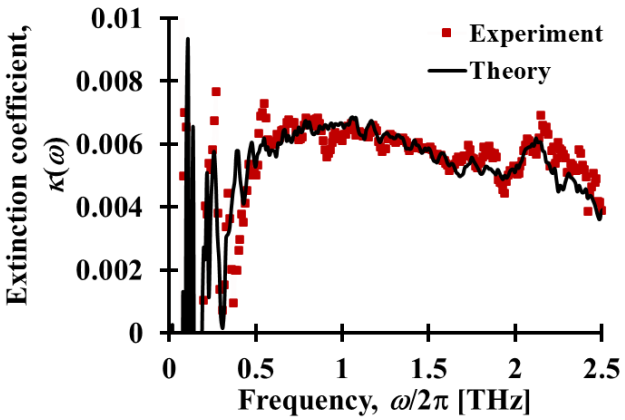

Figure 4.16: The extinction coefficient spectrum of a composite sample made of HDPE wax and low resistivity silicon microparticles is shown. Experimental data is shown as the red squares and theoretical data generated using the Bruggeman model, with other experimental data for the HDPE dielectric constant and the Drude model for the silicon microparticle dielectric constant, is shown as the black line.

There are a few interesting conclusions from this analysis. First, the theoretical Bruggeman curve fits the experiments data very well for a depolarization factor of 1/6, indicating that the losses can be definitively attributed to free carrier absorption. This depolarization factor in this fit was somewhat lower than for the PDMS composites, though this could be explained by the fact that dry mixing the particles leaves the possibility of the multiple silicon particles clustering into a slightly more spherical particle. The depolarization factor still varies significantly from the case of spherical particles. The second interesting conclusion from these results is the fact that both the theory and the experimental data show that composite extinction coefficient is effectively zero at low THz frequencies, rises rapidly until about 500 GHz, plateaus around 750 GHz, and slowly decreases for higher frequencies. This is counterintuitive since, as will be seen in Section 5.3, a pure material exhibiting free carrier absorption should have infinite extinction at low frequencies and extinction should decrease approximately with $1/\omega$. Simply summing the extinction introduced by free carrier absorption in the silicon microparticles with the extinction of the HDPE wax should produce a concave curve with THz frequency. However, combining the dielectric constants of the host and particles using the Bruggeman model produces the opposite effect, a convex curve that peaks around 750 GHz. This is due to the fact that the imaginary component in the solution to the Bruggeman model becomes zero if the dielectric constant of one of the materials dominates over the other. Finally, several other samples were fabricated using HDPE wax and low resistivity silicon. These samples were fabricated with higher volumetric fractions (>4%), thus their losses were proportionally higher making them difficult to fit to the Drude model as their measurements were

only valid below 1 THz. However, they all showed the same rapid increase in extinction coefficient with frequency below 500 GHz followed by a leveling off the extinction coefficient around 750 GHz. The Drude fit in Figure 4.16 showed that the low resistivity silicon microparticles were *n*-type with an electron density of 4×10^{17} cm^{-3} and a carrier mobility of 1100 cm^2/Vs. These results clearly show the detrimental effects of free carrier absorption in the particles. The sample shown in Figure 4.16 had a volumetric fraction of particles that was less than 1%, yet extinction was still dominated by the particles for frequencies below 1.5 THz. For useful volumetric fractions (i.e., $V > 15\%$), the losses from these particles is catastrophic due to free carrier absorption for thick samples.

To remedy this, HRFZ Si can be used as the particles due to its low free carrier density. Unfortunately, these microparticles cannot be purchased as they are expensive to produce and find little use in other industries. Therefore, several thick wafers of HRFZ Si were purchased and ground into microparticles. The microparticle fabrication was done in two steps. First, the HRFZ Si wafers were crushed using a mortar and pestle to produce particles that varied in size between 50 μm and 2 mm. Since these particles are still an order of magnitude larger than what is required for composites, the particles were further broken up using a high energy planetary ball mill. The powdered HRFZ Si was cooled using liquid nitrogen to make the particles more brittle before ball milling. The resulting microparticles after ball milling were filtered using a 45 μm stainless steel mesh filter to remove any large particles that may not have been ground sufficiently. The particle size distributions after grinding, milling, and filtering are shown in Figure 4.17a, and an SEM image of the particles after grinding and filtering is shown in Figure 4.17b. Approximately 6 grams of milled, filtered HRFZ Si was fabricated.

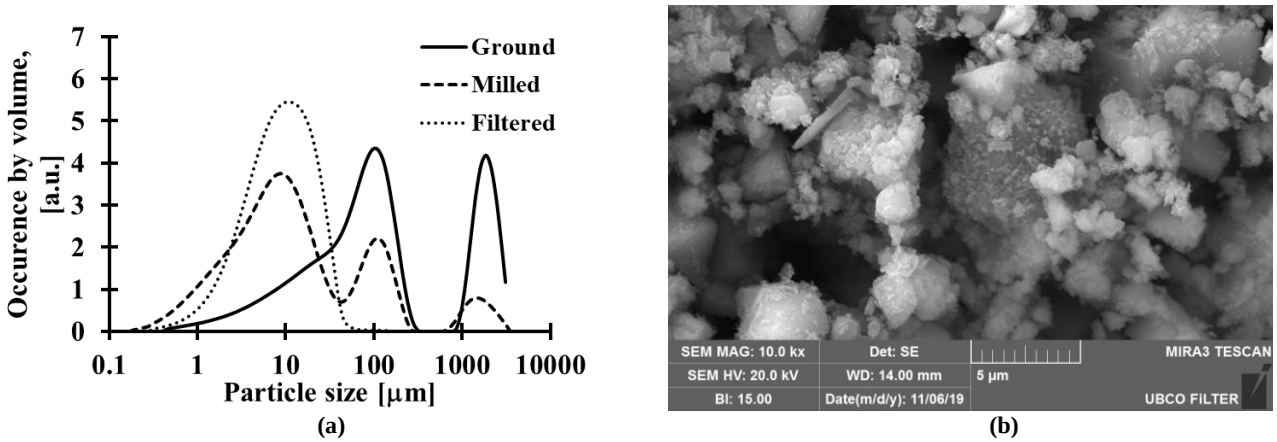

(a) (b)

Figure 4.17: Particle size distributions of the ground, milled, and filtered HRFZ Si particles are shown in (a). The solid line corresponds to the particle size distribution after grinding, the dashed line corresponds to the particle size distribution after milling, and the dotted line corresponds to the particle size distribution after filtering the milled particles. The vertical axis corresponds to the volumetric occurrence of particles at a particular size. An SEM image of the particles after grinding and filtering is shown in (b).

Clearly, simply grinding the particles produces an average particle size of 100 μm, which is far too large to be used in THz composite materials. Grinding the particles in the planetary ball mill produced a significant volume of particles that were around 10 μm, though a few larger particles remained. Note that a number of particles that remained above 1 mm after grinding were manually removed before milling. After filtering, only particles small enough to fit through the 45 μm mesh remained giving an average final particle size of 9.43 μm with 90% of the particles falling below 26 μm.

These particles were used to fabricate a few micro-HRFZ Si composite samples, using UHMWPE as a host, with varying volumetric fractions. The refractive index and extinction coefficient results are shown in Figure 4.18. Scanning electron microscope images of the samples are shown in Figure 4.17b. These images were taken to see whether the HRFZ Si microparticles were roughly spherical, like the alumina microparticles, or highly irregular, like the Si and SiO_2 microparticles. Each data point corresponds to the average refractive index or extinction coefficient spectrum between 500 GHz and 1 THz.

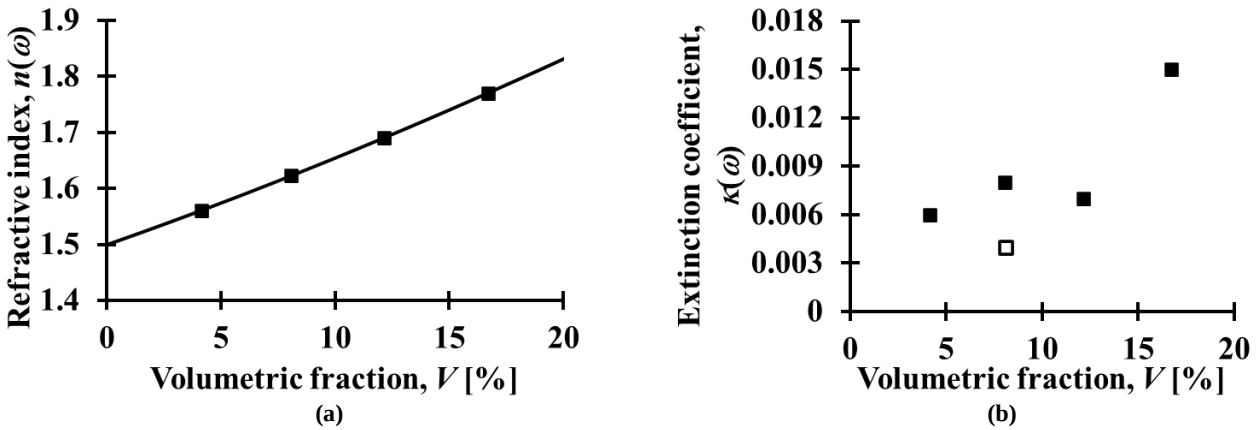

Figure 4.18: The refractive index (a) and extinction coefficient (b) for composites made using UHMWPE and HRFZ Si are shown as a function of volumetric fraction. The black squares correspond to the experimental data, while the black line corresponds to the Bruggeman model fit. The hollow black square in (b) corresponds to the extinction coefficient of one of the samples after re-pressing.

The results for refractive index show almost perfect agreement with the Bruggeman model with a depolarization factor of 0.286 or 1/3.5. This indicates that the HRFZ Si particles are roughly spherical, though with some irregularities. This corroborates the particles seen in Figure 4.17b, which show the HRFZ Si particles as roughly spherical. The fitted refractive index for UHMWPE was somewhat lower than in previous composites at 1.5, though this could be a result of a small amount of air remaining trapped in the samples. A refractive index of 1.77 is observed for a volumetric fraction of 16.7%, again confirming the silicon is a good choice of particle from a refractive index standpoint. The extinction coefficient results are somewhat less encouraging. The black squares are the experimentally measured extinction coefficient from the original pressing of the composite samples. These results show significant extinction in the composite samples with an estimated extinction coefficient for the HRFZ Si microparticles of approximately 0.1. This was largely due to improper pressing, as evidenced by the significantly lower extinction for the sample with a volumetric fraction of 12.1%, so two samples were re-pressed. The result for the sample with a volumetric fraction of 8.1% is shown as the hollow square in Figure 4.18b. Unfortunately, the sample with a volumetric fraction of 4.1% was damaged during re-pressing and the sample with a volumetric fraction of 16.7% was destroyed to investigate its internal structure by SEM, though this analysis did not yield any useful insights. Clearly the extinction coefficient goes down after re-pressing, though it remains significantly higher than the UHMWPE host and even somewhat higher than the alumina particles. It is unclear whether this high extinction is entirely due to the manufacturing process, since re-pressing other samples did not entirely eliminate

the excess extinction from poor fabrication, or whether the Si microparticles themselves had a higher extinction coefficient than expected. It is entirely possible that the Si microparticles have an increased extinction coefficient due to their fabrication. The high energy ball milling process may have modified the crystal structure of the crystalline Si wafer to be somewhat polycrystalline, since the ball milling process generated a significant amount of heat, which would allow grain fractures to occur without the entire microparticle breaking apart. An alternative possibility is the presence of impurities from the milling and filtering process. These could be alumina microparticles from the milling balls and cup, or silicon dioxide from the stone mortar and pestle. However, the number of uncontrolled variables in the fabrication of the Si microparticles indicate that more experimentation is unlikely to yield more conclusive results. Therefore, micro-HRFZ Si composites made from milled HRFZ Si microparticles are poorly suited to fabricate spherical THz retroreflectors.

In summary, fabricating spherical retroreflectors for THz applications is challenging due to material loss. An appropriate refractive index can be easily obtained by making composite materials with high refractive index particles. Unfortunately, all the particles investigated in this work had unacceptably high extinction. This means that any spherical retroreflector fabricated using these composite materials would absorb most of the retromodulated signal, reducing retroreflection efficiency to an unusable level. If composites with lower loss particles could be demonstrated in for THz spectrum, it may still be possible to implement a spherical THz retroreflector at that point.

Chapter 5: Terahertz Modulators

The previous chapter designed and characterised THz retroreflectors. The other half of a THz retromodulator, the modulator, will be designed and characterised in this chapter. The characterisations are compared to the theoretical predictions in Chapter 3. This chapter will deal exclusively with optical modulators comprised of a long-lifetime semiconductor as these are the simplest to fabricate and produce deep, broadband modulation. It is found that these modulators are capable of nearly 100% modulation efficiency, though at low modulation rates.

5.1 Optical Modulator Measurement Configurations

The optical modulator investigated in this thesis is an intrinsic germanium wafer. Intrinsic germanium was selected as an optical modulator for the THz spectrum primarily due to its long charge carrier lifetime, which allows for high modulation efficiencies. However, as will be shown later, this comes at the expense of modulation rates. Analysis of the intrinsic germanium modulator was divided into four parts. First, the charge carrier dynamics of the germanium modulator were modelled using the Drude model, extended to include both the charge carrier generation and THz detection mechanics. Second, the intrinsic germanium modulator was measured in a THz TDS system and the results were compared to the models to extract various material parameters such as charge carrier density and charge carrier scattering time. Third the charge carrier lifetime of the germanium modulator was measured, then reduced by modifying the modulator's surface characteristics to obtain higher modulation rates. Over an order of magnitude increase in modulation rate is observed, though at the cost of modulation efficiency. Finally, the experimental results for the modulation efficiency and insertion efficiency of the unmodified modulator are compared to the modulation efficiency and insertion efficiency expressions from the link budget analysis in Chapter 3.

Much of the analysis in this section is based off a modified version of THz TDS system three, described in Chapter 4. The primary modification is the introduction of a CW NIR pump laser whose beam is coincident with the focus between the second and third parabolic mirrors of THz TDS system three. The CW NIR pump beam photo-generates charge carriers in the germanium modulator, which is placed at the focus of the parabolic mirrors. Now the THz

radiation passing through the germanium sample, which will be referred to as the probe beam, is subject to the photo-induced charge carriers. The THz probe beam simulates the active downlink signal being modulated and has a larger beam diameter than the THz beam so that uniform illumination of the modulator can be assumed. Figure 5.1 shows a diagram of the modified experimental setup. The intrinsically doped germanium modulator has an orientation of (111), a thickness of $\delta = 325$ μm, and a resistivity of 50 Ω·cm (corresponding to an intrinsic carrier density of 2×10^{13} cm^{-3} for both electrons and holes). Placing the germanium modulator in the focused beam allows measurements to be made with a greater SNR, though it should be noted that the focal depth of THz TDS system three is long enough that the THz modulator is effectively in a collimated beam. The CW NIR pump laser (Newport, LQD980-220E) outputs a maximum power of 220 mW at 980 nm at a maximum modulation frequency of 100 MHz, shown as the purple beam in Figure 5.1.

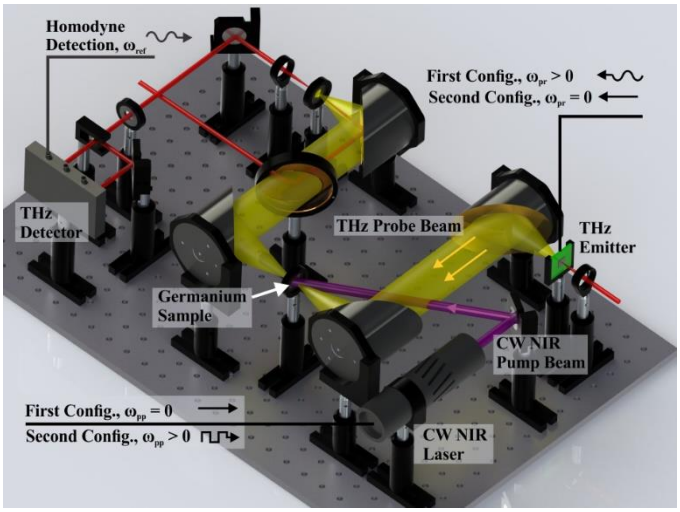

Figure 5.1: A schematic of the experimental setup is shown. The THz emitter and detector, the CW NIR pump laser, and the sample are denoted. The red beam incident on the THz emitter and detector is a 100 fs, 780 nm pulsed beam, the yellow beam is the broadband THz pulse, and the purple beam is the 980 nm CW NIR pump beam. In the first configuration, which is for ultrafast measurements, the yellow THz beam is directly modulated at an angular frequency of ω_{pr}, while the purple CW NIR pump beam is unmodulated, i.e., $\omega_{pp} = 0$. In the second configuration, which is for quasi-static measurements, the purple CW NIR pump beam is directly modulated at an angular frequency of ω_{pp}, while the yellow THz beam is unmodulated by the emitter, i.e., $\omega_{pr} = 0$, but is externally modulated by effects induced in the germanium sample by the CW NIR pump beam. Figure reproduced with permission from [50] © 2021 IEEE.

The detected signal can be modelled by allowing the THz probe beam to propagate through the experimental setup including propagation through the modulator. Much of this modelling was done in Section 3.4.4, so this analysis will begin with the equation for transmission through a THz modulator (3.7). In the experimental setup, the

amplitude of the THz probe beam can be modulated by the THz emitter at an angular frequency of ω_{pr}, i.e., the yellow beam in the figure is directly modulated by the green THz emitter, giving the transmitted electric field amplitude to be

$$E_t(\omega) = E_0(\omega)\cos(\omega_{pr}t)t_{in}(\omega)t_{out}(\omega)\frac{e^{-k_0\kappa(\omega)\delta}e^{-j(k_0 n(\omega)\delta-\omega t)}}{1-r(\omega)^2 e^{-2k_0\kappa(\omega)\delta}e^{-j2k_0 n(\omega)\delta}}. \quad (5.1)$$

The amplitude of the THz probe beam is not the only quantity that is modulated. As will be discussed later, the secondary probe beam perturbs the modulator refractive index and extinction coefficient through the electrical susceptibility of the modulator described by the Drude model. For now, the refractive index and extinction coefficient in (5.1) can be written as the sum of the intrinsic and perturbed values giving

$$E_t(\omega) = E_0(\omega)\cos(\omega_{pr}t)t_{in}(\omega)t_{out}(\omega)\frac{e^{-k_0(\kappa(\omega)+\Delta\kappa(\omega))\delta}e^{-j(k_0(n(\omega)+\Delta n(\omega))\delta-\omega t)}}{1-r(\omega)^2 e^{-2k_0(\kappa(\omega)+\Delta\kappa(\omega))\delta}e^{-j2k_0(n(\omega)+\Delta n(\omega))\delta}}. \quad (5.2)$$

This equation describes the electric field of THz probe beam as it arrives at the electro-optic detector. Converting the electric field in the ZnTe crystal to a voltage measurement from the differential detector produces

$$V_d(\omega,t) = V_0(\omega)\cos(\omega_{pr}t)t_{in}(\omega)t_{out}(\omega)e^{j\omega\tau_d}\frac{e^{-k_0(\kappa(\omega)+\Delta\kappa(\omega))\delta}e^{-jk_0(n(\omega)+\Delta n(\omega))\delta}}{1-r(\omega)^2 e^{-2k_0(\kappa(\omega)+\Delta\kappa(\omega))\delta}e^{-j2k_0(n(\omega)+\Delta n(\omega))\delta}}, \quad (5.3)$$

where V_0 is a combination of the electric field amplitude and the detector gain/conversion constants, and τ_d is the time delay between the probe pulse and the THz pulse. Finally, the homodyne detector mixes the detected voltage signal with a local oscillator at ω_{ref} and applies a lowpass filter to the output. After mixing and lowpass filtering, the detected voltage signal will be

$$V_d(\omega) = V_0(\omega)\frac{t_{in}(\omega)t_{out}(\omega)}{T_p}e^{j\omega\tau_d}\int_0^{T_p}\cos(\omega_{ref}t)\cos(\omega_{pr}t)\frac{e^{-k_0(\kappa(\omega)+\Delta\kappa(\omega))\delta}e^{-jk_0(n(\omega)+\Delta n(\omega))\delta}}{1-r(\omega)^2 e^{-2k_0(\kappa(\omega)+\Delta\kappa(\omega))\delta}e^{-j2k_0(n(\omega)+\Delta n(\omega))\delta}}dt, \quad (5.4)$$

where T_p is the period of the reference sinusoid. All the analysis done in this thesis will be done in the frequency

domain with respect to the THz signal. Therefore, the Fourier transform of (5.4) must be taken with respect to τ_r. Doing so gives the THz spectrum for each time-domain scan to be

$$V_d(\omega) = V_0(\omega)\frac{t_{in}(\omega)t_{out}(\omega)}{T_p}\int_0^{T_p}\cos(\omega_{ref}t)\cos(\omega_{pr}t)\frac{e^{-k_0(\kappa(\omega)+\Delta\kappa(\omega))\delta}e^{-jk_0(n(\omega)+\Delta n(\omega))\delta}}{1-r(\omega)^2e^{-2k_0(\kappa(\omega)+\Delta\kappa(\omega))\delta}e^{-j2k_0(n(\omega)+\Delta n(\omega))\delta}}dt\,. \qquad (5.5)$$

The THz TDS measurement system operates in one of two configurations depending on what is being measured. The first configuration is used to measure the ultrafast (femtosecond) material parameters of the germanium modulator, while the second configuration measures the quasi-static (microsecond) charge carrier lifetime of the germanium modulator, which is related to its modulation rate. In the first configuration, which is for ultrafast measurements, the THz probe beam is modulated directly by modulating the THz emitter at an angular frequency of ω_{pr} and the CW NIR pump beam unmodulated with $\omega_{pp} = 0$. In this configuration, the frequency selective homodyne detection system measures at the angular frequency of the THz probe beam. This effectively gives a THz TDS measurement of the modulator at various modulation efficiency based on the intensity of the CW NIR beam. Two measurements are required to determine ultrafast material properties of the modulator, one with and one without the CW NIR pump beam incident on the modulator.

In the second configuration, which is for quasi-static charge carrier lifetime measurements, the THz probe beam is unmodulated with $\omega_{pr} = 0$ and the CW NIR pump beam modulated at an angular frequency of ω_{pp}, i.e., the purple beam in the figure is directly modulated and the yellow beam is indirectly modulated by the purple beam after the modulator. In this configuration, the frequency selective homodyne detection system measures at the angular frequency of the CW NIR pump beam. This effectively measures the modulation in THz signal induced by the CW NIR pump beam. The modulation efficiency is dependent on the angular frequency of the CW NIR pump beam and decreases with increasing frequency. Table 5.1 summarizes the corresponding frequencies and measured parameters used for each configuration. The ultrafast measurements include electron scatter time, $\tau_{s,e}$, hole scatter time, $\tau_{s,h}$, and charge carrier density, N. The quasi-static measurements are used to determine charge carrier lifetime, τ_r, and surface recombination velocity, S. It should be noted that the homodyne detection described here requires that the

repetition rate of the ultrafast pulsed laser be much faster than the reference frequency to simplify the separation of these two effects by filtering during detection. Otherwise, narrow-band filtering is required to separate effects from the ultrafast pulsed laser and the reference frequency when both are on the same order of magnitude. While this experimental setup is used in this thesis to measure the properties of a germanium modulator, it can also be used to measure other semiconductor materials with ultrafast scatter times and quasi-static charge carrier recombination times, such as intrinsic silicon.

Table 5.1: Frequencies and measured quantities for each measurement configuration

	Ultrafast configuration	Quasi-static configuration
CW NIR pump frequency, $\omega_{pp}/(2\pi)$	DC	500 Hz – 500 kHz
THz probe frequency, $\omega_{pr}/(2\pi)$	40 kHz	DC
Reference frequency, $\omega_{ref}/(2\pi)$	40 kHz	500 Hz – 500 kHz
Measurements	$\tau_{s,e}$, $\tau_{s,h}$, N	τ_r, S

It must be emphasized here that this measurement system only measures relaxed charge carriers due to the continuous nature of the CW NIR pump beam. As a result, the ultrafast scatter times measured in the first configuration are for electrons at the bottom of the L valley and holes at the top of the heavy and light hole bands in the valence band. Although the CW NIR pump beam excites charge carriers with excess kinetic energy, these carriers relax within a few picoseconds [131] and remain in their relaxed state until recombination occurs several hundred microseconds later. Consequently, the density of hot carriers is negligible compared to density of relaxed carriers, and the results in this work reflect the dynamics of relaxed charge carriers.

5.2 Charge Carrier Dynamics Modelling in Germanium

Each model for detected THz signal in (5.5) for each configuration will now be evaluated. The first step is to model the charge carrier density in the modulator generated by the CW NIR pump beam. These charge carriers subsequently affect the phase and absorption of the THz electric field co-incident on the modulator regardless of configuration. The charge carrier density is defined by

$$\frac{dN(t)}{dt} = \frac{G_{op}}{A_\phi \delta}\left(1 + \sum_{i=1}^{\infty} \frac{4\sin(\omega_{pp}(2i-1)t)}{\pi(2i-1)}\right) - \frac{N(t)}{\tau_r}. \tag{5.6}$$

This equation states that the rate of change in the charge carrier density in the modulator is the rate at which carriers are optically excited minus the rate at which charge carriers recombine. In the optical excitation term, G_{op} is the optical generation rate in electron-hole pairs per unit time, δ is the thickness of the germanium modulator, which is assumed to be much less than the diffusion length of the charge carriers, and A_ϕ is the effective (diffusion broadened) spot size of the charge carrier distribution. This spot size is assumed to be independent of the charge carrier density for simplicity, although others have done similar analyses including diffusion since they were interested in the spatial distribution of charge carriers [132]. This is a valid assumption since the spot size will be larger than the THz beam diameter. The optical excitation term is multiplied by an infinite series describing a square wave with angular frequency ω_{pp} and a mean value of one. The integer i is the index of the sum. In the first measurement configuration the pump beam is unmodulated, $\omega_{pp} = 0$, which has the sine term in the infinite series go to zero giving a constant optical excitation of $G_{op} / A_\phi \delta$. In the second measurement configuration the pump beam is modulated, $\omega_{pp} > 0$, which has the infinite series form a square wave with an amplitude of two and a frequency of ω_{pp}. The charge carrier recombination term contains the current charge carrier density and the charge carrier lifetime, τ_r. The steady state solution to the previous equation gives a charge carrier density of

$$N(t) = \frac{G_{op}\tau_r}{A_\phi \delta}\left(1 + \sum_{i=1}^{\infty} \frac{4}{\pi(2i-1)} \frac{\cos(\omega_{pp}(2i-1)t - \theta_i)}{\sqrt{1 + (\omega_{pp}(2i-1)\tau_r)^2}}\right), \tag{5.7}$$

where $\theta_i = \pi - \arctan(1/(\omega_{pp}\tau_r(2i-1))$ is the phase between the photo-generation and ensuing charge carrier density. The time varying charge carrier density shown in (5.7) induces a time varying electric susceptibility in the modulator. One very insightful conclusion can be drawn from the presence of the charge carrier lifetime as a multiplicative constant in (5.7). The charge carrier lifetime will directly affect the magnitude of the charge carrier density with shorter charge carrier lifetimes resulting in smaller charge carrier densities, which in turn result in lower modulation efficiencies. This is unfortunate since modulation rate is directly proportional to charge carrier

lifetime. Consequently, faster modulators will have lower modulation efficiencies. As shown in Section 3.4.4, time varying charge carrier density maps itself onto the time varying susceptibility, which finally manifests as a time varying change in refractive index, $\Delta n(\omega,t)$, and extinction coefficient, $\Delta\kappa(\omega,t)$, in the modulator. The next step is to model the detected signal for each configuration.

Configuration one, which is for ultrafast measurements, has the charge carrier density in the germanium modulator be constant during measurements. This removes any time dependence from the change in refractive index and the change in extinction coefficient. Additionally, setting $\omega_{ref} = \omega_{pr}$ simplifies the measurement spectrum to

$$V_d(\omega) = V_0(\omega)\frac{t_{in}(\omega)t_{out}(\omega)}{2}\frac{e^{-k_0(\kappa(\omega)+\Delta\kappa(\omega))\delta}e^{-jk_0(n(\omega)+\Delta n(\omega))\delta}}{1-r(\omega)^2e^{-2k_0(\kappa(\omega)+\Delta\kappa(\omega))\delta}e^{-j2k_0(n(\omega)+\Delta n(\omega))\delta}}. \tag{5.8}$$

The challenge in solving this equation lies in the fact that $V_0(\omega)$, which is the spectral power at each THz frequency coming from the emitter, is unknown. However, taking two measurements and dividing the output spectra results in $V_0(\omega)$ cancelling out. Therefore, two measurements must be taken: one with the pump beam off ($\Delta\kappa(\omega) = \Delta n(\omega) = 0$) and one with the pump beam on ($\Delta\kappa(\omega) \neq 0$ and $\Delta n(\omega) \neq 0$). Dividing (5.8) with the beam on by (5.8) with the beam off gives the measured spectrum for configuration one, $V_1(\omega)$, to be

$$V_1(\omega) = e^{-k_0\Delta\kappa(\omega)\delta}e^{-jk_0\Delta n(\omega)\delta}\frac{1-r(\omega)^2e^{-2k_0\kappa(\omega)\delta}e^{-j2k_0n(\omega)\delta}}{1-r(\omega)^2e^{-2k_0(\kappa(\omega)+\Delta\kappa(\omega))\delta}e^{-j2k_0(n(\omega)+\Delta n(\omega))\delta}}. \tag{5.9}$$

The measured spectrum for $V_1(\omega)$ is used to extract the changes in refractive index, $\Delta n(\omega)$, and extinction coefficient, $\Delta\kappa(\omega)$, and these results are fit to the Drude model via (2.2), (2.3), (2.4), and (5.7). The fitting yields values for the volume of the charge carrier distribution, $A_\phi\delta$, charge carrier lifetime, τ_r, and scatter times of electrons and holes, $\tau_{s,e}$ and $\tau_{s,h}$, with corresponding mobilities of electrons and holes being $\mu_e = q\tau_{s,e}/m_e^*$ and $\mu_h = q\tau_{s,h}/m_h^*$, respectively.

Configuration two, which is for quasi-static measurements, has the charge carrier density in the germanium modulator be modulated with a square wave during measurements and the amplitude of the incident THz electric field be constant over time. The reference frequency in this configuration is set to $\omega_{\text{ref}} = \omega_{\text{pp}}$. This simplifies (5.5), giving the measured spectrum for configuration two, $V_2(\omega)$, to be

$$V_{\text{d}}(\omega) = V_0(\omega)\frac{t_{\text{in}}(\omega)t_{\text{out}}(\omega)}{T_{\text{p}}}\int_0^{T_{\text{p}}}\cos(\omega_{\text{ref}}t)\frac{e^{-k_0(\kappa(\omega)+\Delta\kappa(\omega,t))\delta}e^{-\text{j}k_0(n(\omega)+\Delta n(\omega,t))\delta}}{1-r(\omega)^2e^{-2k_0(\kappa(\omega)+\Delta\kappa(\omega,t))\delta}e^{-\text{j}2k_0(n(\omega)+\Delta n(\omega,t))\delta}}dt\,. \qquad (5.10)$$

The challenge now is that the change in refractive index and extinction coefficient in the exponential terms are modulated with a square wave. This is a non-linear process, compounded by the internal reflections. While it is possible to solve this equation numerically, a simpler analytical solution may still provide useful insight. Of particular interest is finding the THz spectrum amplitude's dependence on pump frequency, ω_{pp}, as this should show the charge carrier lifetime, τ_{r}. To obtain a simple expression for this, the following assumption are made:

1. Ignore all internal reflections. This was verified to only introduce a scalar amplitude error and no error to the pump frequency dependence.
2. Assume that $\tilde{\chi}_{\text{e}}(\omega,t)$ and $\tilde{\chi}_{\text{h}}(\omega,t)$ are much less than $n(\omega)^2$. This allows (2.3) to be linearized using the Taylor series.
3. Assume that the square wave modulation can be approximated by its first term. The process of mixing with the reference frequency and applying the lowpass filter will remove most of the higher order terms regardless.
4. Assume that $k_0\Delta\kappa(\omega,t)\delta$ is much less than one. This allows the linearization of one of the exponential terms in (5.10) using the Taylor series. This assumption is valid to a first order approximation for all pump fluences used in this work, though it breaks down for higher pump fluences.
5. Assume that $\kappa(\omega) = 0$ and $n(\omega) >> \Delta n(\omega,t)$, which is particularly valid for germanium and the pump fluences in this work.

Applying these assumptions and simplifying gives,

$$V_2(\omega) = -\frac{V_0(\omega)t_{\text{in}}(\omega)t_{\text{out}}(\omega)k_0\Delta\kappa(\omega)\delta}{\sqrt{1+(\omega_{\text{pp}}\tau_{\text{r}})^2}}\cos(\theta_1)e^{-\text{j}k_0 n(\omega)\delta}. \tag{5.11}$$

A more detailed derivation is given in Appendix C. Clearly, the THz spectrum amplitude will be constant when $\omega_{\text{pp}}\tau_{\text{r}} < 1$ and will roll off with the inverse of the pump frequency when $\omega_{\text{pp}}\tau_{\text{r}} > 1$. At the critical point $\omega_{\text{pp}}\tau_{\text{r}} = 1$, the amplitude of the THz spectra will have fallen to $1/\sqrt{2}$ of its zero-frequency value. Therefore, the THz spectral amplitudes can be plotted as a function of pump frequency and then fit to this roll-off to determine the charge carrier lifetime. To determine the error introduced by the assumptions used to obtain this result, (5.10) and (5.11) were coded into MATLAB and plotted together as a function of the pump frequency for a THz frequency of 1 THz and a charge carrier lifetime of 50 μs/rad or about 314 μs. The simulation of the full equation (5.10) still neglects internal reflections, as these only apply a multiplicative factor to the results. It should be noted that homodyne detection measurements for all configurations are carried out using a vector lock-in amplifier, which splits the input signal from the detector into two channels and mixes one channel with sine and the other with cosine. The advantage of this is that when the reference frequency is out of phase with the detected signal in one of the channels, it will be perfectly in phase with the other channel. This is important for the second configuration since the phase of the charge carrier density oscillations vary with ω_{pp} as seen by the inclusion of the $\cos(\theta_1)$ term. The simulated measurements are the quadrature sum of two forms of (5.10), one where the equation is as shown (in phase), and one where $\cos(\omega_{\text{pp}}t)$ is replaced by $\sin(\omega_{\text{pp}}t)$ (quadrature). Figure 5.2 shows the output of both the in phase and quadrature channels individually as well as the sum and the simplified approximation at a THz frequency of 1 THz.

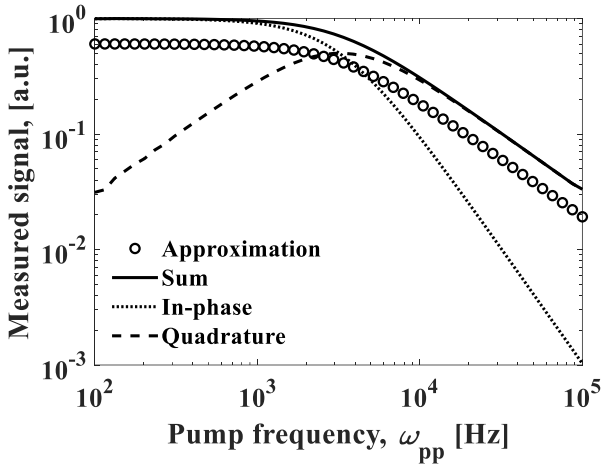

Figure 5.2: Simulated pump frequency dependence of the lock-in amplifier output amplitude for various approximations of configuration two. The full expression in (5.10) with no approximations, other than no internal reflections, is shown as the solid black line. This is the sum of the lock-in amplifier's in-phase, dotted line, and quadrature, dashed line, components. The simplified approximation in (5.11) is shown as the hollow circles.

The figure clearly shows that the phase of the charge carrier density shifts the detected signal from the in-phase channel (dotted line) to the quadrature channel (dashed line). Note that the signal from each channel is equal at the inverse charge carrier lifetime. In addition, the shape of the quadrature sum (solid line) agrees very well with the approximation (circles) to a multiplicative factor. This indicates that the measured THz spectra can be normalized and compared to the approximate equation to extract charge carrier lifetime.

5.3 Ultrafast Germanium Modulator Measurements

The characterization of ultrafast charge carrier scattering in the intrinsic germanium modulator was carried out using the first measurement configuration. The CW NIR pump beam was unmodulated, $\omega_{pp} = 0$, and the THz probe beam modulated at a frequency of $\omega_{pr}/2\pi = 40$ kHz, which was locked to by the homodyne detection system. Figure 5.3a shows the resulting THz TDS time-domain waveforms with the CW NIR pump beam off, on at low intensity, and on at high intensity. All three waveforms were Fourier transformed and the two spectra with the CW NIR pump beam on were each divided by the spectrum when the CW NIR pump beam was off for fitting to the theory in Section 5.2. The amplitude spectrum ratios are plotted along with the fitted model in Figure 5.3b. In addition, Figure 5.3c and Figure 5.3d plot the refractive index and extinction coefficient, respectively, for the high and low CW NIR pump beam intensities. These values more intuitively show the effects of CW NIR pump beam intensity on the optical germanium modulator. In all plots, experimental data for the high-intensity ratio is shown by black circles,

the experimental data for the low-intensity ratio is shown as black triangles, the theoretical data for the high-intensity ratio is shown as an orange dashed line, and the theoretical data for the high-intensity ratio is shown as a solid orange line. In all theoretical fits, the intrinsic refractive index and extinction coefficient were taken to be $n(\omega) = 4$ and $\kappa(\omega) = 1\times10^{-3}$, respectively. It is interesting to note that modulation is so deep in Figure 5.3b for frequencies below 1 THz when the CW NIR laser's intensity is high, that experimental data in this region lies outside of the dynamic range of the measurement system and is unreliable, see Chapter 4. However, the remaining bandwidth up to 2.5 THz is reliable.

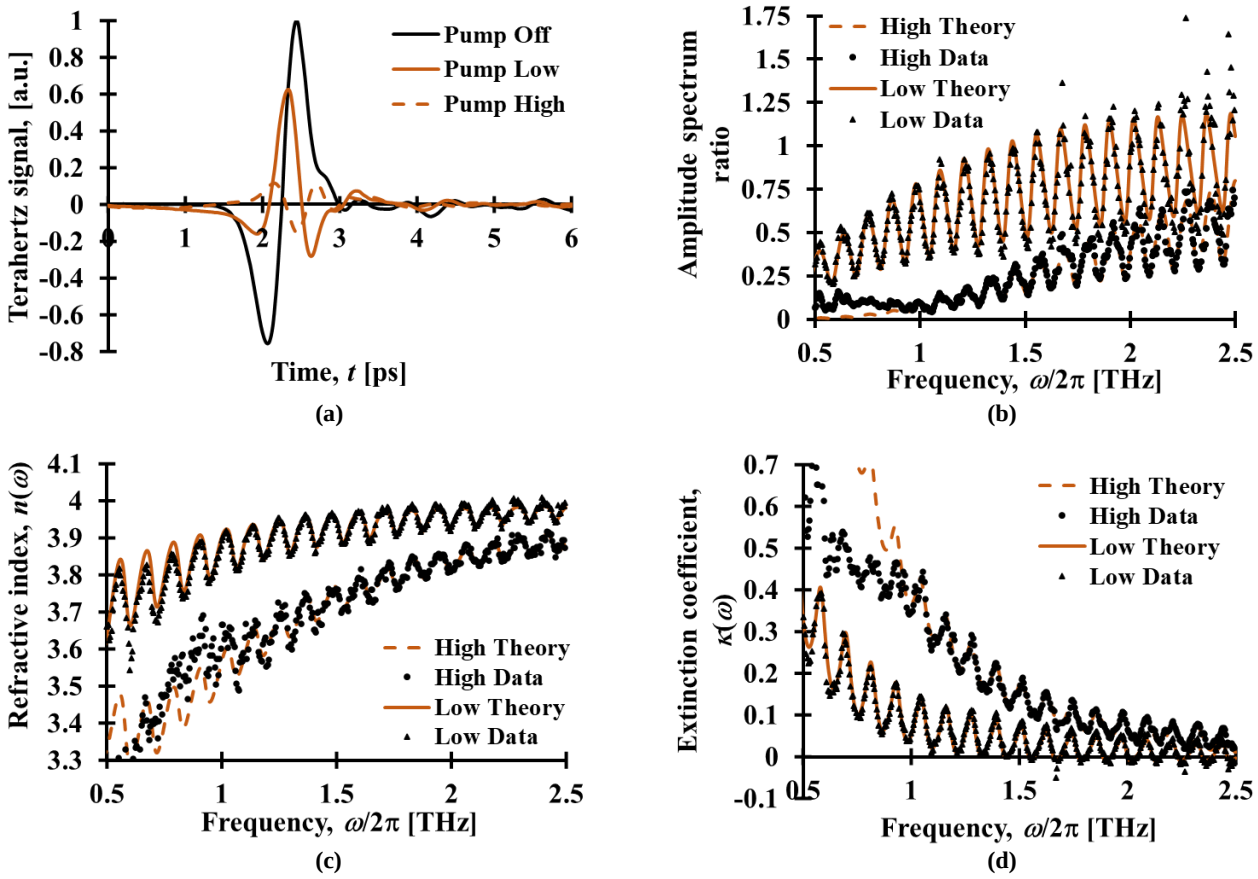

Figure 5.3: The ultrafast characterization of the intrinsic germanium modulator using THz TDS system three in configuration one is shown. The time domain signals for the modulator with the CW NIR pump beam off (solid black line), at low intensity (solid orange line), and at high intensity (dashed orange line) are shown in (a). The measured amplitude spectrum ratios (b), refractive index (c), and extinction coefficient (d) for low intensity and high intensity are also shown. In figures (b)-(d), theoretical curves are denoted by the solid orange line for low intensity data and the dashed orange line for high intensity data. The experimental data itself is denoted by the black triangles for low intensity and the black circles for high intensity.

The figure shows good agreement between the theoretical values and experimental measurements. The theory in (5.9) is fitted to the experimental data in Figure 5.3, yielding a charge carrier density of $N(\omega) = 5.6\times10^{15}$ cm^{-3} (which

is equal for both electrons and holes), a scatter time of $\tau_{s,e}$ = 210 fs for electrons, and a scatter time of $\tau_{s,h}$ = 180 fs for holes. These scatter times give mobility values of $\mu_e = q\tau_{s,e}/m_e^* = 3100$ cm^2/(V·s) for electrons and $\mu_h = q\tau_{s,h}/m_h^* = 1500$ cm^2/(V·s) for holes. These mobilities are somewhat lower than the literature mobility values of $\mu_e = q\tau_{s,e}/m_e^* = 3900$ cm^2/(V·s) for electrons and $\mu_h = q\tau_{s,h}/m_h^* = 1900$ cm^2/(V·s) for holes [30], [133], a discrepancy attributed to the presence of carrier-carrier scattering. The Drude model fits to the experimental data yield an equal carrier density for both electrons and holes of roughly 1.4×10^{15} cm^{-3}, with charge carrier scatter times of $\tau_{s,e}$ = 266 fs for electrons and $\tau_{s,h}$ = 227 fs for holes. These scatter times give mobility values of $\mu_e = q\tau_{s,e}/m_e^* = 3900$ cm^2/(V·s) for electrons and $\mu_h = q\tau_{s,h}/m_h^* = 1900$ cm^2/(V·s) for holes, which correlate with the mobilities found in the literature [30], [133]. While it is possible to attempt to measure the scatter time for various CW NIR pump beam intensities and quantify the dependence of carrier scatter time on charge carrier density, the uncertainty in the scatter times shown above is significant. As a result, any analysis of the charge carrier density dependence on scatter time would be challenging to assert with confidence. In addition, while the fitted charge carrier densities could be used in (5.7) to estimate the charge carrier lifetime, τ_r, such a result would be unreliable. The charge carrier lifetime, τ_r, and effective (diffusion broadened) spot size, A_ϕ, appear as an unknown ratio in (5.7), making it necessary to assume a value for A_ϕ to calculate τ_r. To avoid this problem, the quasi-static characterization is applied next with controlled levels of diffusion.

5.4 Quasi-static Germanium Modulator Measurements

The characterization of quasi-static charge carrier recombination in germanium was carried out using the second measurement configuration. In this configuration, the CW NIR pump beam is modulated with a square-wave whose frequency is swept over $\omega_{pp}/2\pi$ = 100 Hz to 300 kHz. The THz probe beam was unmodulated, $\omega_{pr} = 0$. The reference for homodyne detection is locked to the CW NIR pump beam, such that $\omega_{ref} = \omega_{pp}$. At each probe frequency, ω_{pp}, a THz TDS measurement is taken, and Fourier transformed to give a THz amplitude spectrum. Next, the THz amplitude spectra for various pump frequencies are compared to show the roll-off in THz amplitude at higher pump frequencies. The THz amplitude spectrum used in these measurements spans 500 GHz to 1 THz. The roll-off in

amplitude at each THz frequency is normalized to its largest amplitude at that frequency and plotted as a function of pump frequency. Roll-off plots from the entire range of THz frequencies are averaged to produce an aggregate charge carrier lifetime (the individual charge carrier lifetimes for each THz frequency are fairly consistent, though noisy). The averaged roll-off plot is then fit with the simplified model for configuration two in (5.11) and a charge carrier lifetime is extracted. Figure 5.4a shows the experimental magnitudes displayed as markers, versus the CW NIR pump beam modulation frequency, $\omega_{pp}/2\pi$, with theoretical curve-fits from (5.11) displayed as lines. Results are presented for an unmodified germanium wafer (solid black circles with a solid black line) and a modified germanium wafer that has been immersed in boiling water for several minutes to remove oxide buildup (solid black circles with a dashed black line). The curve-fits for the modified and unmodified germanium samples roll off to $1/\sqrt{2}$ of their zero-frequency values at $\omega_{pp}/(2\pi) = 1/(2\pi\tau_r) \approx 10.3$ kHz and 75.8 kHz, respectively, suggesting charge carrier lifetimes of $\tau_r \approx 97$ μs and 13.2 μs, respectively. The differing values of τ_r seen for the two samples, along with the fact that neither conform to the millisecond bulk charge carrier lifetime measured by others [132], [134], [135], [136], suggest that surface recombination is strongly impacting the charge carrier lifetimes. The effects of surface recombination can be simply modelled using the linear relation

$$1/\tau_r = 1/\tau_{r,b} + SR_{sv}, \tag{5.12}$$

where $\tau_{r,b}$ is the bulk charge carrier lifetime, S is the surface recombination velocity, and R_{sv} is the surface-area-to-volume ratio of the sample [137], [138]. The literature suggests that the unmodified wafer has a surface recombination velocity on the order of 10^3 cm/s [135], while the modified wafer has a surface recombination velocity of 10^4 cm/s [139]. Given the similar surface-area-to-volume ratios for both wafers, and negligible bulk recombination due to the millisecond bulk recombination time in germanium, the tenfold difference in surface recombination velocities for the two bulk wafers matches the nearly tenfold difference in measured charge carrier lifetime.

To more accurately quantify the relationship between charge carrier lifetime and surface recombination, intrinsic germanium samples were fabricated with micro-hole arrays and characterized in terms of their quasi-static charge

carrier recombination. The micro-holes were fabricated using a laser-micromilling machine (Oxford Lasers A-355), and were arranged as square arrays of micro-holes with a hole diameter, d_m, of 100 μm, and pitches between holes, a_m, of 240, 270, 320, 350, 400, 500, or 650 μm. Surface-area-to-volume ratio was calculated using $R_{sv} = \pi d_m/a_m^2$, giving values ranging from 7 to 55 cm^{-1}. All samples were immersed in boiling water to remove oxides from the laser micromill and so should correlate with measurements taken from the modified wafer. Figure 5.4a shows representative experimental and theoretical results for the normalized amplitude spectrum, $V_2(\omega)$, of three micro-hole arrays: an array with R_{sv} = 12.6 cm^{-1} (hollow red circles with a solid red line), an array with R_{sv} = 25.6 cm^{-1} (hollow red circles with a dashed red line), and an array with R_{sv} = 43.1 cm^{-1} (hollow red circles with a dotted red line). Fitting these curves to the simplified equation for configuration two in (5.12) gives the charge carrier lifetimes of these micro-hole arrays to be τ_r = 7.0, 3.2, and 1.5 μs, respectively. Charge carrier lifetime measurements are made for THz probe frequencies ranging from 500 GHz to 1 THz and the error bars in Figure 5.4a correspond to the standard deviation in the data over this range. Clearly, increasing the surface area of the micro-holes hastens surface recombination and decreases the charge carrier lifetime. To extract the surface recombination velocity of the modified germanium samples, the reciprocal of the charge carrier lifetime, $1/\tau_r$, is plotted in Figure 5.4(b) (hollow red circles) versus surface-area-to-volume ratio, R_{sv}, for these three samples and six additional samples. A representative scanning electron microscope image of laser micro-milled holes in germanium is shown in Figure 5.4c. The figure also shows a theoretical curve-fit (solid red line) for the linear relation in (5.12). The slope of the trendline in Figure 5.4b gives a surface recombination velocity of S = 14,200 cm/s. This velocity agrees with values seen in the literature for germanium surfaces treated with boiling water [139]. The error bars in Figure 5.4b correspond to the standard deviations in the measured charge carrier lifetimes and were consistently about ±16%. This leads to the more prominent error bars seen for larger reciprocal lifetimes. This standard deviation makes it challenging to identify an accurate value for the vertical axis intercept, which corresponds to the inverse bulk charge carrier lifetime. The bulk charge carrier lifetime could be assumed to be 13.2 μs, corresponding to the modified wafer charge carrier lifetime. However, this is over an order of magnitude shorter than literature values for bulk charge carrier lifetime in intrinsic germanium indicating that surface effects are still present in this sample.

Therefore, the inverse bulk charge carrier lifetime of the theoretical fit is set to zero, to better conform with the millisecond charge carrier lifetimes seen in the literature.

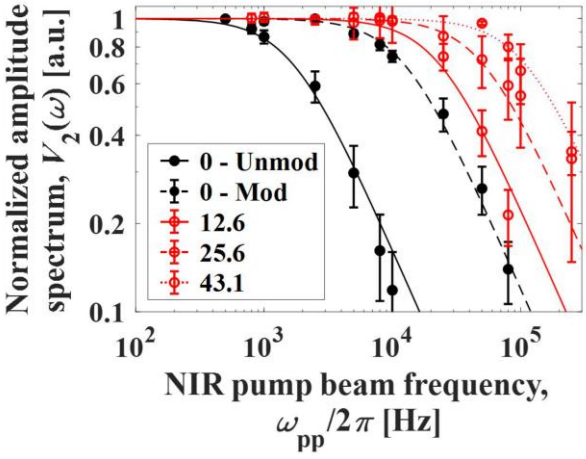

(a)

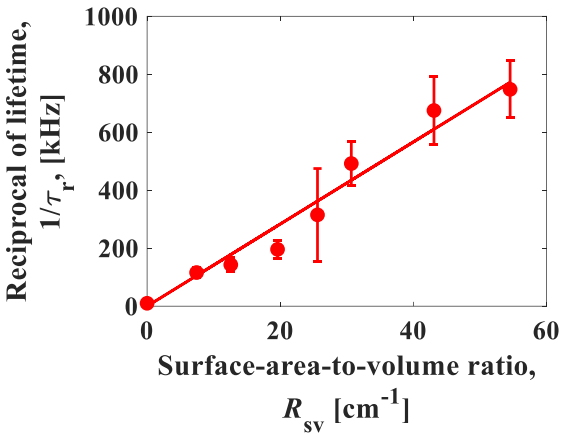

(b)

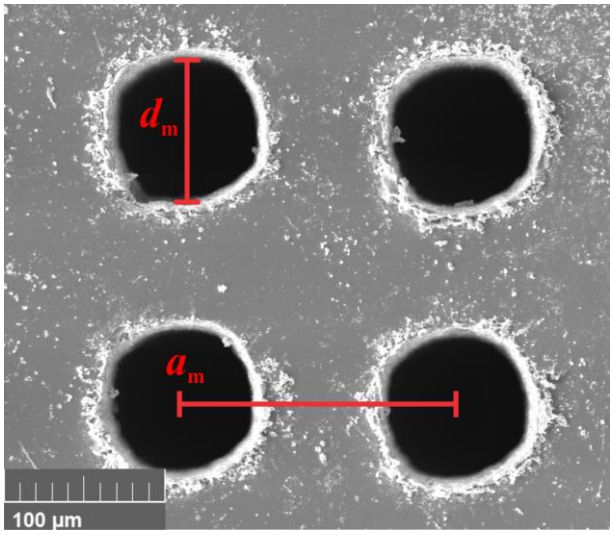

(c)

Figure 5.4: The quasi-static characterization of the intrinsic germanium modulator using THz TDS system three in configuration two is shown. The normalized amplitude spectra for various germanium samples are shown in (a). Experimental and theoretical results are shown for the unmodified germanium sample (solid black circles and a solid black line), the modified germanium sample (solid black circles and a dashed black line), a modified germanium sample with a micro-hole array having R_{sv} = 12.6 cm^{-1} (hollow red circles and a solid red line), a modified germanium sample with a micro-hole array having R_{sv} = 25.6 cm^{-1} (hollow red circles and a dashed red line), and a modified germanium sample with a micro-hole array having R_{sv} = 43.1 cm^{-1} (hollow red circles and a dotted red line). In (b), the reciprocal of the charge carrier lifetime, $1/\tau_r$, is plotted versus the surface-area-to-volume ratio, R_{sv}. Experiment results are shown as hollow red circles and theoretical results from the linear curve-fit are shown as a solid red line. A representative scanning electron microscope image of laser micro-milled holes in germanium with the hole pitch and diameter denoted is shown in (c). Portions of this figure were adapted with permission from [50] © 2021 IEEE.

5.5 Modulation Efficiency, Insertion Efficiency, and Germanium Modulator Summary

The final measurement to be made on the intrinsic germanium modulator is modulation efficiency. To quantify modulation efficiency, the measured THz spectrum ratio from Section 5.3 is taken and converted into modulation efficiency. To do so, the THz amplitude spectrum ratio must be squared to convert from electric field to intensity, then one minus this ratio squared is taken. The figures below show the experimental results for modulation efficiency for the high-intensity, Figure 5.5a, and low-intensity pump beam, Figure 5.5b, along with the theoretical fits from Section 5.2. Experimental data is shown as the black points and the theoretical fits are shown as the orange lines.

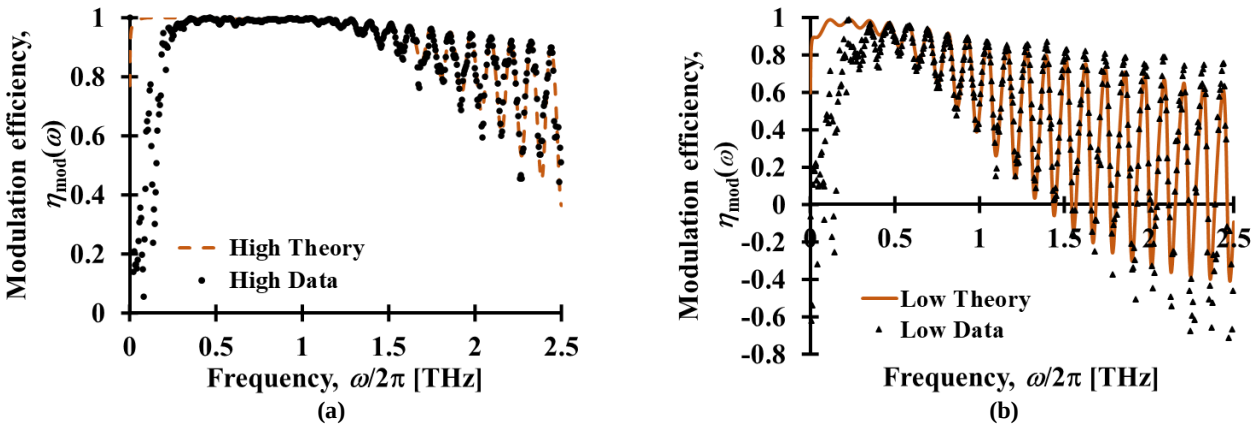

Figure 5.5: Modulation efficiency as a function of THz frequency is shown for a pump beam with high intensity (a) and low intensity (b) is shown. Theoretical results are shown as the dashed orange line in (a) and the solid orange line in (b). The experimental results are shown as the black circles in (a) and the black triangles in (b).

These results show a few interesting trends. First, the high-intensity pump beam has virtually 100% modulation efficiency between 400 GHz and 1.2 THz, making it an excellent broadband modulator. Broadband modulators such as this one are especially useful as they operate with the same modulation efficiency for glancing incident polar angles, which have the modulated THz beam take a longer path through the modulator than for normal incidence. This longer path shifts the etalon fringes, which are seen above 1.2 THz, producing an incident angle dependent modulation efficiency unless extinction in the modulator is large enough to eliminate the etalon fringes. Second, when the pump beam intensity decreases, as seen in Figure 5.5b, the modulation efficiency becomes extremely frequency dependent. While modulation efficiency above 80% exist in bands up to 1.5 THz, there are also bands above 1.5 THz where modulation efficiency goes negative. This presents an interesting design possibility

where modulation could manifest as an increase in transmission through the modulator as opposed to a decrease. This increase in transmission is caused by the optically induced change in refractive index shifting the etalon fringes enough that certain frequencies see destructive interference when the pump beam is off and constructive interference when the beam is on. The increase in signal strength caused by the change in interference is greater than the loss induced by the optically induced extinction coefficient. However, since negative modulation efficiency occurs for frequencies that normally see destructive interference, the overall transmitted signal will still be low. It is better to find a frequency where transmission is high due to constructive interference when the pump beam is off. In that case modulation is induced by both extinction and by a shift to destructive interference by the changing refractive index when the pump beam is on.

The final parameter that is required to quantify the intrinsic germanium optical modulator is its insertion efficiency. Two measurements were taken for the germanium modulator, one with the modulator in place, but without the pump beam on, and one with the modulator entirely removed from the testing setup. Dividing the spectra for these two measurements and squaring to convert to intensity gives insertion efficiency, which is plotted in Figure 5.6. In the figure, experimental data is shown as black circles and the theoretical curve from (3.10) is shown as the orange line.

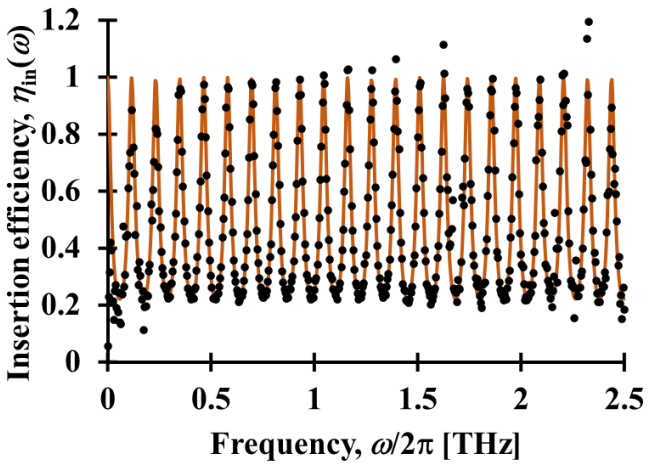

Figure 5.6: Insertion efficiency as a function of THz frequency is shown. The theoretical results are denoted by the solid orange line and the experimental results are denoted by the black dots.

The insertion efficiency is a stark reminder of the effects of interference on the transmission through the modulator. Both the theory and experimental data in Figure 5.6 show huge swings from 25% transmission through the modulator to 100% transmission over only about 50 GHz. This means that modulator performance is going to be extremely frequency dependent regardless of whether the modulation efficiency is frequency dependent since overall modulator performance is the product of insertion efficiency and modulation efficiency. Note that changing the thickness of the modulator will change the interference fringes significantly. To make performance more independent of frequency, the modulator can be made thinner, which will reduce the number of fringes and widen them.

Finally, the intrinsic germanium modulator can be specified for a few different frequencies and pump powers. Table 5.2 below is a summary of the performance specification of the modulator. Note that numbers were adjusted to correspond to the nearest resonance peak, since modulator thickness can be designed to place these peaks at any desired frequency and these peaks are wider than the 1 GHz bandwidth used for the SHM detector. Additionally, the resonance peaks in Figure 5.5 and Figure 5.6 lie at the same frequency, meaning that a frequency with peak insertion efficiency will also have peak modulation efficiency.

Table 5.2: Experimentally measured modulation efficiency and insertion efficiency for the intrinsic germanium modulator

Frequency (GHz)	Modulation efficiency (low/high)	Insertion efficiency
300	0.98/0.97	0.99
650	0.98/0.94	0.99
850	0.99/0.90	0.99

Chapter 6: Terahertz Retromodulators

The previous chapters have analysed the individual components of a THz retromodulator in depth and made recommendations on which retroreflector and modulator to use. The conclusions of their respective chapters recommend that a cornercube retroreflector should be used with an optical modulator made of a long lifetime semiconductor such as intrinsic germanium. This modulator will have a high retroreflection efficiency and significant modulation efficiency, though at the cost of slow modulation rate. This chapter will briefly describe the design of a prototype THz retromodulator then evaluate its performance for incident angle efficiency, modulation efficiency, insertion efficiency, and modulation rate. These experimental values will be used to carry out one final link budget analysis for the prototype THz retromodulator.

6.1 Retromodulator Design

The final THz retromodulator design uses the shutter architecture with an intrinsic germanium modulator placed over top of a cornercube retroreflector. This design takes advantage of the good retroreflection efficiency of the cornercube retroreflector and the significant modulation efficiency of optically pumped intrinsic germanium. The retroreflector used in the experimental setup was the same one quantified in Section 4.1 and the intrinsic germanium modulator was the unmodified modulator described in Chapter 5. The modulator was placed directly over top of the cornercube and the assembled prototype THz retromodulator is shown in the rendering in Figure 6.1. The intrinsic germanium modulator is mostly transparent in the rendering to show the cornercube underneath, though the modulator is opaque in reality.

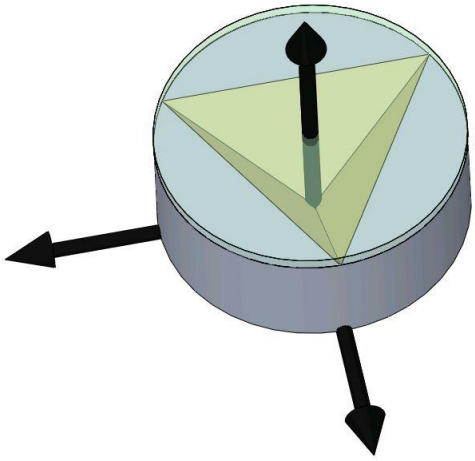

Figure 6.1: A modelled image of the prototype THz retromodulator with an affixed coordinate frame is shown here. The intrinsic germanium modulator is affixed overtop of the cornercube retroreflector shown in Figure 3.2d. For illustrative purposes, the intrinsic germanium modulator is shown to be mostly transparent.

The prototype THz retromodulator fits into a 2.5 cm diameter circular holder and has an effective retroreflection area of 0.87 cm^2 due to the retroreflection efficiency of the cornercube measured in Section 4.1. The modulator was pumped by the CW NIR pump laser described in Section 5.1 with a peak power of 220 mW.

6.2 Incident Angle Efficiency, Modulation Efficiency, Insertion Efficiency, and Modulation Rate

The prototype THz retromodulator was tested to determine its incident angle efficiency, modulation efficiency, insertion efficiency, and modulation rate. All measurements were carried out in THz TDS system four. As with the cornercube retroreflector, the incident angle efficiency of the prototype retromodulator was determined by making THz TDS measurements of the retroreflected signal at various incident polar angles. The TDS measurements were Fourier transformed and the average amplitude spectrum from 300 GHz to 1 THz was plotted for each incident angle. The results are shown in Figure 6.2, where the squares correspond to the experimental data and the solid line corresponds to the theory presented in Section 3.4.1. The error bars are the standard deviation of the experimental measurements over the averaged bandwidth.

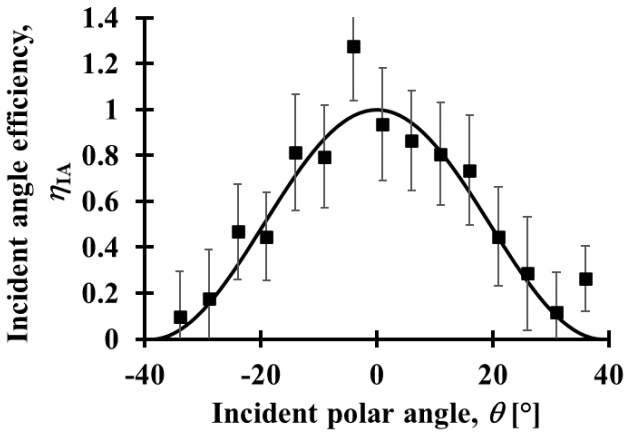

Figure 6.2: The incident angle efficiency results are shown as a function of incident polar angle for the prototype THz retromodulator. The experimental data is shown as the black squares, while the theoretical curve is shown as the solid black line. The error bars on the experimental data correspond to the standard deviation of the experimental data over the averaged bandwidth.

The results confirm that the prototype THz retromodulator has the same incident angle efficiency as the cornercube retroreflector it makes use of. In fact, artefacts such as the erroneously high value at θ = -4° are reproduced for the retromodulator. The poor SNR in TDS system four is the cause of the poorer fit of the data in general as well as the larger error bars in these results compared to the results presented in Figure 4.4. However, the overall incident angle efficiency trend remains the same. This is important since the free-space modulator used in a retromodulator cannot affect the retroreflection performance. The results here show that this is the case for the germanium optical modulator.

The modulation efficiency of the prototype THz retromodulator was measured by pumping the retromodulator in configuration one, as described in Section 5.1. In this configuration, the CW NIR pump beam is unmodulated, and the THz signal beam is sinusoidally modulated. Two measurement scans are taken: one with the CW NIR pump beam on, and one with the CW NIR pump beam off. The two measured time domain waveforms are Fourier transformed and their amplitude spectra are divided. Taking one minus the divided spectra gives the measured modulation efficiency as a function of frequency, which is shown in Figure 6.3.

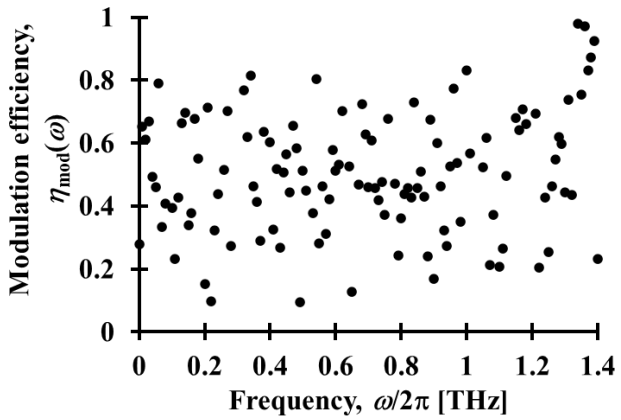

Figure 6.3: The modulation efficiency results are shown as a function of THz frequency for the prototype THz retromodulator.

The figure shows that the experimental modulation efficiency of the prototype THz retromodulator is significant, though noisy. The noise in the measurements is due to poor SNR in the THz TDS system due to the use of THz TDS system four and not to the retromodulator itself. While the plot appears to show random scatter, the associated time domain waveforms show clear modulation. The average modulation efficiency between 300 GHz and 1.3 THz is 48% ± 17%. These modulation efficiency results have been converted from the measured field quantities into intensity to match the retromodulation equation. The modulation efficiency of the measured electric field was around 30%. Note that this modulation efficiency is for two passes through the modulator. While it is technically possible to attempt to fit the modulation efficiency data shown here to a theoretical curve, such as the ones shown in Figure 5.5, little correlation would be present due to the error on the measurements. Therefore, no theoretical models were plotted in Figure 6.3.

The modulator insertion efficiency of the prototype THz retromodulator was determined by taking several THz TDS scans of the retromodulator with and without the modulator present. The retromodulator was at an incident polar angle of about 10° for all measurements. The experimental and theoretical results for insertion efficiency as a function of frequency are shown in Figure 6.4.

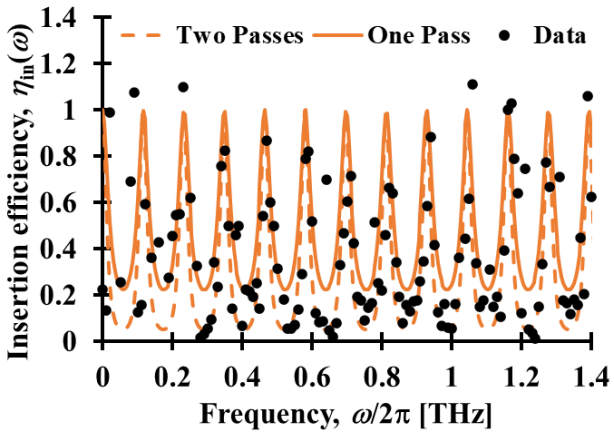

Figure 6.4: The insertion efficiency results are shown as a function of THz frequency for the prototype THz retromodulator. Experimental data is shown as the black circles, while the theoretical model for a single pass through the modulator is shown as the solid orange line and the theoretical model for two passes through the modulator is shown as the dashed orange line.

As with the modulation efficiency, the results for the prototype THz retromodulator insertion efficiency are quite noisy. Again, this is due to low SNR in THz TDS system four as opposed to an issue with the retromodulator. The experimental data for insertion efficiency, shown as the black circles in Figure 6.4, follows the same periodic trend seen in the insertion efficiency for the intrinsic germanium modulator alone in Section 5.5. The theoretical model for insertion efficiency is shown for both one pass though the modulator, solid orange line, and two passes through the modulator, dashed orange line. Strangely, the measured insertion efficiency does not seem to be correlated well with the solid line for one pass through the modulator as was seen in Figure 6.4. The measured insertion efficiency for the prototype retromodulator seems to be equally well correlated to the model predicting two passes through the modulator. The r squared values for the single pass and double pass models are 0.51 and 0.48, respectively. This is likely an artefact of the TDS measurement system. The reason insertion efficiency should only be applied to the incoming signal is the fact that all energy that enters the retromodulator will eventually be transmitted back out, though it may be reflected several times off the underside of the modulator first. Unfortunately, a TDS system only measures the THz waveform over a certain period of time. This period of time is likely too short to capture all the reflections between the cornercube and the underside of the modulator, so the retroreflected signal looks as if the insertion efficiency was applied one and a half times. While a longer TDS scan could be made, the decreasing amplitude of the THz pulse with each set of internal reflections inside the retromodulator along with the poor SNR of the system mean that it is unlikely that many reflections will be measured. The measurements used to generate

Figure 6.4 were able to capture one internal reflection with a useable SNR, which resulted in measured insertion efficiency values that were closer to the single pass model between 700 GHz and 1 THz.

The modulation rate of the prototype THz retromodulator was experimentally verified using measurement configuration two from Section 5.1 in the retroreflection TDS setup. In this configuration, the CW NIR pump beam was modulated with a square wave and the homodyne detection was locked onto its frequency. The results are shown in Figure 6.5. Charge carrier lifetime measurements are made for THz probe frequencies ranging from 400 GHz to 1 THz and the error bars correspond to the standard deviation in the data over this range.

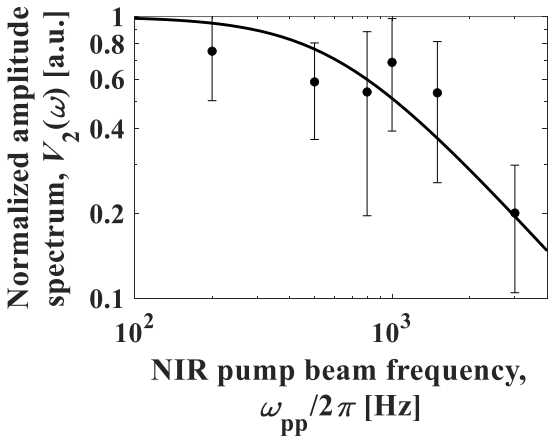

Figure 6.5: Normalized amplitude spectrum results are shown as a function of NIR pump beam frequency for the prototype THz retromodulator. The experimental data points, shown as the black circles, correspond to the average measured THz spectrum between 400 GHz and 1 THz at each CW NIR pump frequency. The error bars correspond to the standard deviation of the measurement spectra over this bandwidth. The solid black line is the fitted frequency roll-off to the experimental data.

The measured charge carrier lifetime for the prototype THz retromodulator is approximately 260 μs, which is somewhat longer than the 97 μs measured for the free-standing modulator. The longer lifetime can be attributed in part due in part to the poor SNR of the retroreflection measurement system, evidenced by the large error bars which denote the standard deviation of the measurements over a bandwidth of 400 GHz to 1 THz. The second pass through the modulator does not affect the charge carrier lifetime as two passes act as if the modulator was simply twice as thick.

6.3 Link Budget Analysis of an Experimental Retromodulator

The primary goal of this thesis is to answer the following question: is a practical THz retromodulation system feasible given current technology? This section will take the values for modulation efficiency, insertion efficiency, retroreflection efficiency, and incident angle efficiency measured from the prototype THz retromodulator (or its components in the case of retroreflection efficiency) and do one final link budget analysis to determine if the prototype THz retromodulator designed in this thesis is capable of operating in a practical THz retromodulation system. This link budget analysis will utilize the transmitters and detectors from systems 1, 3, 4, 5, and 6 in Section 3.4.5. The experimental values for the real retromodulator parameters of the prototype THz retromodulator are given in Table 6.1.

Table 6.1: Experimental values for the real retromodulation parameters of the prototype THz retromodulator

Insertion efficiency*	0 dB
Modulation efficiency	-3.2 dB
Retroreflection efficiency	-7.5 dB
Incident angle efficiency	$\cos^2(2.3\theta)$

*Assuming that the modulator thickness can be modified to have internal resonance correspond to the operating frequency.

The link budget results from Figure 3.5 are plotted in Figure 6.6 along with new results for the prototype THz retromodulator as the hollow black triangles. The device dimensions for the prototype THz retromodulator are identical to what is used in Section 3.4.5 (i.e., link length, detector aperture, etc.) with the exception of the retromodulator diameter, which is 2.5 cm.

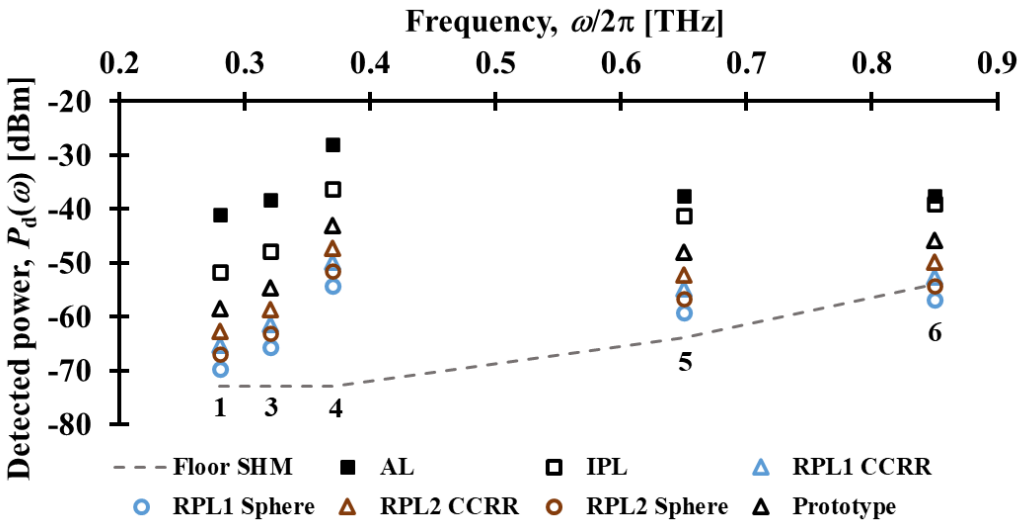

Figure 6.6: Real passive THz link budget results for the five viable systems shown in Figure 3.5 with the addition of experimental data from the prototype THz retromodulator is shown here. The number shown below each set of results corresponds to the respective system. The parameters for each of these systems were given in Table 2.1. The results shown here are identical to the ones in Figure 3.5 with the addition of results for the prototype THz retromodulator, denoted as the prototype data points. As was done in Figure 3.5, the results are for normal incidence, i.e., an incident polar angle of $\theta = 0°$.

The link budget analysis shows that the prototype THz retromodulator demonstrated in this thesis is superior to the theoretical retromodulators given in Section 3.4.5. This is largely due to the unity insertion efficiency and high modulation efficiency of the intrinsic germanium modulator, giving the prototype THz retromodulator a 4 dB advantage over the next best retromodulator. While the high modulation efficiency came at the expense of modulation rate, the unity insertion efficiency was a result of internal reflections within the modulator and can be applied to other, higher speed modulation techniques. The performance of the prototype THz retromodulator resulted in detected signal powers that were at least 10 dB above the noise floor for a SHM detector for all systems with the exception of system 6 at 850 GHz. Of particular importance is system 2, which was the commercially available HHG transmitter. This system was able to close the passive THz link with over 18 dB between the detected signal level and the noise floor. Consequently, this proves that a practical THz retromodulation system is feasible given current technology.

Chapter 7: Conclusion

The future of wireless communications will require an eventual transition from current wireless carrier frequencies in the low tens of gigahertz to hundreds of gigahertz and even low terahertz. This transition comes with a technological challenge since wireless transmitters for frequencies above 300 GHz are bulky and consume a significant amount of power. This limits their use to fixed installations and cannot be practically implemented for handheld mobile devices. This prevents handheld mobile devices from transmitting data with carrier frequencies over 300 GHz. This thesis proposed a novel solution to this challenge through the introduction of passive THz communication links. A passive THz link uses a retromodulator on a mobile device to return power transmitted by a fixed transceiver. This return power is encoded with data by the retromodulator enabling the mobile device to effectively transmit data at carrier frequencies above 300 GHz without needing an onboard THz transmitter. The goal of this thesis was to discover if a passive THz link was feasible given current technology for THz transmitters, detectors, and retromodulators. Theoretical predictions based on literature values were first presented, then a prototype THz retromodulator was designed and characterized to provide a true measure of the feasibility of passive uplinks. The results of a link budget analysis using the prototype THz retromodulator showed that passive THz uplinks are indeed possible given current technology, though there are still significant challenges to be overcome in the design of both the retroreflector and modulator. Improvements to modulation rate, retroreflection efficiency, and incident angle efficiency are required before this technology will be viable for commercial use. Nonetheless, this is the first demonstration of THz retromodulation, which will hopefully enable future low-power handheld mobile devices to operate in bidirectional wireless THz communication system without the need for a THz transmitter.

7.1 Summary of Conclusions and Contributions to the Literature

The body of the thesis, excluding introduction and conclusion, was divided into five chapters, each with their own contributions to overall body of knowledge in THz communication technology. Chapter 2 was a thorough literature review of current THz transmitter and detector technologies as well as a simple review of atmospheric loss in the

THz spectrum. Chapter 3 presented a comprehensive link budget analysis for both active and passive uplinks using both the data from the literature review in Chapter 2 as well as a theoretical model developed for passive links and the various non-idealities of these passive links. Chapter 4 was an experimental analysis of both cornercube and spherical retroreflectors, whose results were compared to the theoretical predictions from Chapter 3. Chapter 5 was an experimental analysis of optical modulators, whose results were compared to the theoretical predictions from Chapter 3. Chapter 6 was an experimental analysis of a prototype THz retromodulator comprised of a cornercube retroreflector and an optical modulator. The results of this analysis were compared to the theoretical results in Chapter 3 and the experimental results for each individual component in Chapter 4 and Chapter 5. Chapter 6 closed with one final link budget analysis using the characterisations of the prototype THz retromodulator in the real retromodulation equation. Specific details of the contributions found in each chapter are listed below.

Chapter 2 presented a thorough literature review of free-space THz communication technology, so no new work was presented in this chapter. The literature review included THz transmitters, THz detectors, atmospheric absorption in the THz spectrum, THz retroreflectors, and free-space THz modulators. Specific attention was given to technologies that have reached maturity as evidenced by commercial availability. The following are the major conclusions from this chapter:

- There are a wide range of THz transmitter and detector technologies both in the literature and commercially available. THz transmitters in particular have many competing technologies with their own advantages and drawbacks. Some transmitter technologies are capable of high-power output, while others are capable of extremely high data rates with complex modulation schemes. Unfortunately, no single technology delivers an ideal THz transmitter, so analyses of multiple different technologies was required. There were also many competing THz detector technologies; however, most of these technologies were unsuitable for wireless THz communication links due to cryogenic cooling requirements or low bandwidth. Only two THz detector technologies, both based on Schottky diodes, were found to be feasible.
- Atmospheric absorption can significantly limit the range of wireless THz communication links. Based on published data from others, water vapour absorption is the dominant atmospheric loss mechanism, though

only at certain resonance frequencies. At these resonance frequencies, wireless THz communication links of only a few metres will be rendered useless due to atmospheric absorption. Fortunately, away from these resonance frequencies atmospheric absorption is low enough to allow wireless THz communication links to operate over hundreds of metres before signal degradation becomes a significant challenge.

- While there have been many demonstrations of retroreflectors in the literature for optical and NIR frequencies, there has been virtually no work done on THz frequencies. This is a major hole in the literature as THz retroreflectors should be simple to fabricate and behave similarly to those for other spectra. There are two additional challenges that exist for THz retroreflectors that typically do not exist for other spectra: signal divergence over short distances, and power absorption when using a refractive retroreflector. A model from the literature is given for aperture diffraction due to the finite size of the THz retroreflector. Power absorption for various materials in the THz spectrum are given and as well as an effective medium theory to facilitate the fabrication of custom materials in the THz spectrum for spherical retroreflectors. These models were used in later chapters.
- Free-space THz modulator designs from the literature are given for both optical and electronic modulators. The Drude model is presented for free carrier absorption in optical modulators. It is found that most optical modulators can be simply modelled; however, the performance of electronic modulators is extremely design dependent and so design metrics were simply tabulated.

Chapter 3 presented a link budget analysis for wireless THz communication links based on active uplinks, ideal passive uplinks, and real passive uplinks. The following are the major conclusions and contributions to literature found in this chapter:

- Link budget equations are presented for active THz uplinks, ideal passive THz uplinks, and real passive THz uplinks. The link budget equation for active THz uplinks is a form of the Friis transmission equation, a common wireless communication link equation. The link budget equation for ideal passive THz uplinks was inspired by the radar range equation, though it was modified to be applicable for passive uplink systems. To the best of the author's knowledge, this equation has not been presented before for THz

retromodulation, though similar forms have been presented for optical retromodulation systems. The link budget equation for real passive THz uplinks is a modified version of the ideal passive THz uplink link budget equation that considers additional losses that occur due to the presence of a retromodulator. These include incident angle efficiency, modulation efficiency, modulator insertion efficiency, and retroreflection efficiency.

- The link budget equations for active and ideal passive THz uplinks are populated based on literature values for THz transmitters, detectors, and atmospheric absorption. This results in several candidate communication systems with various detector technologies, transmitter frequencies, transmitted power, device dimensions, and detector technologies. It is found that systems with low transmitted power, such as optical heterodyning systems, and systems with onerous implementations, such as quantum cascade lasers, are impractical. It is also found that subharmonic mixing detectors are significantly more sensitive than zero-bias detectors, and so only subharmonic mixing detectors should be considered going forward. This analysis concluded that ideal passive THz uplinks are feasible for short link lengths (~5m). To the best of the author's knowledge, a comprehensive link budget analysis of active and ideal passive THz uplinks does not exist in the literature.
- In order to populate the real retromodulation equation, a number of theoretical models needed to be established for retroreflectors and modulators. Ray tracing analyses were done to quantify the retroreflection efficiency and incident angle efficiency for both cornercube and spherical retroreflectors. The effective medium theories presented in Chapter 2 were used to estimate the power absorption of a THz spherical retroreflector, which was included in the retroreflection efficiency. Generalized modelling is only possible for optical modulators and expressions were derived for insertion efficiency and modulation efficiency based on multiple internal reflections in optical modulators along with representative values for free carrier absorption. This results in a highly frequency dependent modulation efficiency and incident angle efficiency, which is verified in Chapter 5.

- The real retromodulation equation is populated for the remaining feasible THz communication systems that came out of the first link budget analysis. Results for various retromodulator diameters, retroreflectors, and modulators are shown. It is apparent that the additional losses associated with real retromodulators result in significantly lower detected signals from real retromodulators when compared to ideal retromodulators. That said, real retromodulators can still close the link for short range communication systems over several metres. To the best of the author's knowledge, a comprehensive link budget analysis of real passive THz uplinks does not exist in the literature.

Chapter 4 presented results for THz retroreflectors. Both cornercube and spherical retroreflectors were considered. An experimental cornercube retroreflector was fabricated and tested. Several attempts were made at fabricating a spherical retroreflector; however, practical considerations prevented a proper spherical retroreflector from being fabricated. The following are the major conclusions and contributions to literature found in this chapter:

- A 2.5 cm diameter cornercube retroreflector was fabricated and tested for incident angle efficiency and retroreflection efficiency. The measured incident angle efficiency agrees well with the theoretical predictions in Chapter 3, though the measured retroreflection efficiency was noticeably lower than the theoretical predictions in Chapter 3. The lower retroreflection efficiency is likely due to imperfect manufacturing of the cornercube retroreflector. To the best of the author's knowledge, no experimental characterizations of cornercube retroreflectors in the THz spectrum have ever been made.
- To fabricate a spherical retroreflector, a material with the correct refractive index must be used. However, no pure material in the THz spectrum is suitable, so a number of polymer composite materials were fabricated using PDMS as a host material and either Si or SiO_2 microparticles or nanoparticles were used as particles. Composites with a wide variety of volumetric fractions were fabricated. Good agreement between the measured refractive indices of these composite samples and the Bruggeman model was observed when both the material dielectric constants and particle geometries were taken into account. This indicates that composite materials can be used to fabricate spherical retroreflectors from a refraction point

of view. However, the absorption loss in these polymer composites was too high to be useful in centimetre diameter spherical retroreflectors.

- Low-loss polymers and particles were pursued as potential candidates to fabricate composite materials for spherical THz retroreflectors. Both polyethylene and COC were considered as host materials, though fabrication challenges needed to be overcome since both polymers are solid at room temperature and could not be easily mixed with particles. The COC was dissolved in toluene and mixed with microparticles, then poured into molds and allowed to dry. This method was effective in producing lower loss composite materials for thin samples; however, thicker samples contained voids due to the significant amount of toluene that needed to evaporate. Since thick samples need to be fabricated for centimetre sized spherical retroreflectors, COC was abandoned as a potential low-loss polymer host. Polyethylene was found in microparticle form allowing it to be dry-mixed with particles and then hot pressed to fully fuse the sample. This method was capable of producing thick polymer composite samples with significantly lower material loss.
- The polyethylene composite fabrication revealed two additional considerations when attempting to fabricate a thick, low-loss polymer composite in the THz spectrum. The first was the effects of the material losses of the particles. Specifically, Drude losses in semiconductors and low degrees of crystallinity in insulators can increase the material losses of the particles by orders of magnitude over what has been observed for pure, crystalline materials. The second consideration was the effects of improper hot-pressing procedure as this potentially introduced significant losses. It was found that improper pressing leaves air voids that not only interfere with the refractive index, but also greatly increase extinction coefficient. This can be alleviated to some extent by re-pressing the samples for an extended period of time, bringing the material losses back down closer to their values predicted by the Bruggeman model.

Chapter 5 presented the results for an experimental optical modulator based on intrinsic germanium. The following are the major conclusions and contributions to literature found in this chapter:

- Measurements for the ultrafast and quasistatic material properties of intrinsic germanium needed to be made using a modified THz TDS setup. Derivations showing the relationship between the measured quantities and the desired material parameters were presented and applied in the remainder of the chapter. These derivations bear resemblance to the work of others, though they were independently derived.
- Ultrafast measurements of intrinsic germanium were made using the modified THz TDS system. The measured ultrafast material parameters corroborated the published values of other groups and showed that large extinction could be optically induced in germanium, which was later seen to result in high modulation efficiencies.
- Quasistatic measurements were made using the modified THz TDS system. The charge carrier lifetime of intrinsic germanium as measured, and it was found that surface recombination plays a significant role in the overall charge carrier lifetime due to the very long bulk lifetime for intrinsic germanium. The effects of surface chemical treatment on intrinsic germanium were briefly explored showing that surface recombination velocity is highly dependent on surface treatment. Next the effects of surface-area-to-volume ratio on charge carrier lifetime were investigated. This analysis showed an order of magnitude reduction in charge carrier lifetime due to increased surface-area-to-volume ratio allowing for the maximum modulation rate of the intrinsic germanium modulator to be engineered. However, decreasing charge carrier lifetime corresponds to a decrease in modulation efficiency limiting the usefulness of this method for optical modulation. The surface recombination velocity for intrinsic germanium treated with boiling water was also extracted and showed good agreement to literature values. While analyses of charge carrier lifetime dependence on surface treatment and surface-area-to-volume ratio have been explored in the literature, to the best of the author's knowledge, this dependence has not been probed using THz on intrinsic germanium.
- The measured results for the ultrafast and quasistatic material parameters of intrinsic germanium with no surface treatment were converted to modulation efficiency and insertion efficiency and compared to the models presented in Chapter 3 for these parameters. Excellent agreement was found between the theory and experimental data, with a modulation efficiency of effectively 100% and an insertion efficiency of

100% both predicted by the theory and observed in experiment. These impressive results, especially insertion efficiency, were highly frequency dependent due to internal reflections within the modulator. These results motivated the use of the intrinsic germanium optical modulator in the prototype retromodulator.

Chapter 6 presented the design and characterisation of a prototype THz retromodulator. The non-ideality parameters in the retromodulation equation were all measured for the prototype THz retromodulator and these values were used to create a link budget for this prototype THz retromodulator. To the best of the author's knowledge, this is the first demonstration of a THz retromodulator, so all of the content in Chapter 6 is novel and cannot be found elsewhere in the literature. The following are the major conclusions of this chapter:

- The design and fabrication of the prototype THz retromodulator is given. The retromodulator consists of a cornercube retroreflector and an intrinsic germanium optical modulator.
- The modulation efficiency, insertion efficiency, incident angle efficiency, and modulation rate are measured for the prototype THz retromodulator. The measured values for the prototype THz retromodulator were largely in line with the corresponding values measured for the cornercube retroreflector or intrinsic germanium optical modulator, though poor SNR in the measurement system resulted in larger experimental errors.
- The measured modulation efficiency, insertion efficiency, incident angle efficiency, and modulation rate were inserted into the real retromodulation equation and a link budget analysis was done for the prototype THz retromodulator. It was found that the prototype THz retromodulator performs better than the theoretical retromodulators in Chapter 3 largely due to significant modulation efficiency and an insertion efficiency of essentially unity. This indicates that passive THz uplinks are feasible given current technology.

7.2 Limitations

This section will give a brief discussion of the limitations of the work presented in this thesis. There are several major limitations of this work. The first is the size of the cornercube retromodulator. While a 2.5 cm diameter retromodulator is small in comparison with a conventional THz transmitter, it would still be somewhat unwieldy to integrate with current mobile devices. While a smaller retromodulator could be used, this will greatly reduce the retroreflected power, and thus will make the passive THz link more challenging to close. Additionally, integrated electronics are constantly being shrunk down to smaller sizes with lower power requirements. It is not unreasonable that the high harmonic generation transmitters may one day be small enough to fit in a mobile device and be efficient enough to run on a standard lithium-ion battery. The second limitation of the prototype THz retromodulator presented in this work is the link length. The link length used in all analyses was five metres, which is reasonable for small indoor environments, but too short for larger indoor spaces. Ideally, with additional transmitter power, the link lengths should be extended to a few tens of metres. Finally, the prototype THz retromodulator had an approximate bit rate of about one kilobit per second, which is extremely slow. For this technology to meet even modest wireless bandwidth expectations, this data rate needs closer to one gigabit per second. This could be achieved using electronic modulators, which would a natural continuation to the work presented in this thesis. Nonetheless, the work presented in this thesis is the first demonstration of passive THz uplink technology, which has the potential to open the door to a new class of low power devices operating in the THz spectrum.

7.3 Future Work

There are two major extensions and two minor extensions to the work presented in this thesis that would greatly benefit THz retromodulation technology. The first major extension is to move from optical modulators to electronic modulators based on frequency-selective surfaces. This would be a very involved project taking several years to complete. The objectives of this work would be as follows:

1. Design and fabricate a non-switchable frequency-selective surface for THz wavelengths. This would establish key fabrication capabilities and demonstrate that a broadband, polarization insensitive surface can reliably fabricated.

2. Design and fabricate a switchable THz frequency-selective surface based on the non-switchable frequency-selective surface from the previous objective. The switching would be brought about by lightly doping a surface layer of charges in a low-loss semiconductor for THz frequencies such as GaAs. By applying a voltage to the antenna array of the frequency-selective surface, charges would either be attracted to or repelled from the antennas altering their resonance frequency. This method has been shown in the literature to produce modulation rates of 10 kHz to 1 MHz.
3. Finally, to increase modulation rate, transistors would need to be embedded into gaps in the frequency-selective surface antennas. This would be challenging; however, it has been shown to be possible in the literature. Potentially, modulation rates of several MHz could be achieved. This modulator could be combined with the cornercube retroreflector shown in this work to demonstrate a prototype THz retromodulator capable of modulation rates high enough to be feasible.

The second major extension to the work presented in this thesis is to attempt to design and fabricate a cat's eye retroreflector for THz wavelengths. A cat's eye retroreflector uses two hemispheres of the same refractive index, but different radii to achieve retroreflection. This is motivated by the high losses present in the composite materials investigated in this work. Pure HDPE would be a viable material for a cat's eye retroreflector. The objectives for this work would be as follows:

1. Run FDTD simulations for a cat's eye retroreflector to determine the required hemisphere diameters for retroreflection. This has been carried out by other students working with the author's research group.
2. Fabricate several hemispheres to be used in the cat's eye retroreflector out of a low-loss polymer, such as HDPE, by either injection molding, hot pressing, or milling from a solid block. This work is currently underway.
3. Coat the appropriate hemispherical surfaces with metal and assemble the cat's eye retroreflector.
4. Test the assembled cat's eye retroreflector in the THz TDS system four to determine retroreflection performance.

The first minor extension is to enhance modulation efficiency of the existing modulators by integrating them into a 1D photonic crystal. The photonic crystal would need to be transparent to any optical pumping wavelength, though several different polymers and semiconductors could be viable photonic crystal layers. Polymer layers of arbitrary thickness and modestly tunable refractive index could be fabricated using dissolved COC composites. The objectives for this work would be as follows:

1. Design the refractive indices and layer thicknesses required for the photonic crystal using either closed form derivations or numerical simulations.
2. Fabricate thin single layers of various materials with high accuracy to ensure the photonic crystal can be fabricated with acceptable tolerances.
3. Fabricate a non-switchable photonic crystal to ensure that the fabricated structure agrees with the theory.
4. Fabricate and test a switchable photonic crystal using the germanium modulators presented in this thesis.

The second minor extension would be to attempt to improve the retromodulator design given in this thesis to be more compact and efficient. This could be done in several different ways as follows:

1. Trim the corners of the cornercube retroreflector and increase its size. It was shown in this thesis that the corners do not contribute appreciably to the retroreflected signal, yet they significantly reduce the size of cornercube that can fit into a holder. This would increase retroreflection efficiency and reduce beam divergence.
2. Make the internal surfaces of the cornercube out of germanium that can be modulated directly. If the back surfaces are germanium wafers with metallization on their back surface, degrade modulation efficiency will increase somewhat compared to the shutter architecture due to multiple passes through the modulating material. However, the larger surface area and surface reflection will hamper modulation efficiency.
3. Pump the retromodulator using LEDs as opposed to a laser. LEDs would be more than capable of operating at the kilohertz modulation rates and hundreds of milliwatts seen in this thesis. They could be inserted behind the modulator by cutting the corners of the retroreflector out, since these corners do not contribute

appreciably to retroreflection. This would provide a more monolithic retromodulator design where all the required components are mounted into a single block.

These potential future work projects show that, while the prototype retromodulator demonstrated in this thesis is an exciting development, there are many improvements that can be made to enhance the performance of passive THz uplinks.

Bibliography

[1] T. Kürner and S. Priebe, "Towards THz communications-status in research, standardization and regulation," *J. Infrared Millim. Terahertz Waves*, vol. 35, no. 1, pp. 53-62, Jan. 2014.

[2] I. F. Akyildiz, J. M. Jornet, and C. Han, "Terahertz band: Next frontier for wireless communications," *Phys. Commun.*, vol. 12, pp. 16-32, Sep. 2014.

[3] N. Yang, L. Wang, G. Geraci, M. Elkashlan, J. Yuan, and M. Di Renzo, "Safeguarding 5G wireless communication networks using physical layer security," *IEEE Commun. Mag.*, vol. 53, no. 4, pp. 20-27, Apr. 2015.

[4] Z. Pi, and F. Khan, "An introduction to millimeter-wave mobile broadband systems," *IEEE Commun. Mag.*, vol. 49, no. 6, pp. 101-107, Jun. 2011.

[5] X. Wu, G. V. Eleftheriades, and T. E. van Deventer-Perkins, "Design and characterization of single-and multiple-beam mm-wave circularly polarized substrate lens antennas for wireless communications," *IEEE Trans. Microw. Theory Tech.*, vol. 49, no. 3, pp. 431-441, Mar. 2001.

[6] T. S. Rappaport, G. R. MacCartney, M. K. Samimi, and S. Sun, "Wideband millimeter-wave propagation measurements and channel models for future wireless communication system design," *IEEE Trans. Commun.*, vol. 63, no. 9, pp. 3029-3056, Sep. 2015.

[7] M. Ogusu, K. Inagaki, and Y. Mizuguchi, "60 GHz millimeter-wave source using two-mode injection-locking of a Fabry-Perot slave laser," *IEEE Microw. Wireless Compone. Lett.*, vol. 11, no. 3, pp. 101-103, Mar. 2001.

[8] M. Achour, "Free-space optical communication by retromodulation: concept, technologies, and challenges" in *Advanced Free-Space Optical Communications Techniques and Technologies*, London, England, Dec. 2004, vol. 5614, pp. 52-64.

[9] J. E. Cunningham, J. E. Ford, W. Jan, and R. N. Pathak, "Reflectivity from multiple quantum well modulator with contrast ratio of 22:1 at 1.55 um," in *Integrated Optoelectronics*, Beijing, China, Sep. 1996, vol. 2891, pp. 61-71.

[10] J. P. de Carvalho, N. Marques, H. Veiga, C. R. Pacheco, and A. D. Reis, "Performance measurements of a 1550 nm Gbps FSO link at Covilhã City, Portugal," in *IEEE Int. Conf. Applied Electronics*, Pilsen, Czech Republic, Sep. 2010, pp. 1-5.

[11] A. Kanno, T. Kuri, I. Morohashi, I. Hosako, T. Kawanishi, Y. Yoshida, and K. I. Kitayama, "Coherent terahertz wireless signal transmission using advanced optical fiber communication technology," *J. Infrared Millim. Terahertz Waves*, vol. 36, no. 2, pp. 180-197, Feb. 2015.

[12] R. Lange, B. Smutny, B. Wandernoth, R. Czichy, and D. Giggenbach, "142 km, 5.625 Gbps free-space optical link based on homodyne BPSK modulation," in *Free-Space Laser Communication Technologies XVIII*, San Jose, CA, USA, Mar. 2006, vol. 6105, p. 61050A.

[13] *Safe use of lasers*, ANSI Z136.1-2014, 2014.

[14] P. Luo, M. Zhang, Y. Liu, D. Han, and Q. Li, "A moving average filter based method of performance improvement for ultraviolet communication system," in *IEEE Int. Symp. Communication Systems, Networks & Digital Signal Processing*, Poznan, Poland, Jul. 2012, pp. 1-4.

[15] G. A. Shaw, A. M. Siegel, J. Model, and D. Greisokh, "Recent progress in short-range ultraviolet communication," in *Unattended Ground Sensor Technologies and Applications VII*, Orlando, FL, USA, May 2005, vol. 5796, pp. 214-226.

[16] M. R. Hussein, "Ultraviolet radiation and skin cancer: molecular mechanisms," *J. Cutan. Pathol.*, vol. 32, no. 3, pp. 191-205, Mar. 2005.

[17] G. H. Sigel Jr, "Vacuum ultraviolet absorption in alkali doped fused silica and silicate glasses," *J. Phys. Chem. Solids*, vol. 32, no. 10, pp. 2373-2383, Jan. 1971.

[18] S. Jia, X. Yu, H. Hu, J. Yu, T. Morioka, P. U. Jepsen, and L. K. Oxenløwe, "THz wireless transmission systems based on photonic generation of highly pure beat-notes," *IEEE Photonics J.*, vol. 8, no. 5, pp. 1-8, Aug. 2016.

[19] B. Scherger, M. Scheller, C. Jansen, M. Koch, and K. Wiesauer, "Terahertz lenses made by compression molding of micropowders," *Appl. Opt.*, vol. 50, no. 15, pp. 2256-2262, May 2011.

[20] M. Wichmann, A. S. Mondol, N. Kocic, S. Lippert, T. Probst, M. Schwerdtfeger, S. Schumann, T. Hochrein, P. Heidemeyer, M. Bastian, and G. Bastian, "Terahertz plastic compound lenses," *Appl. Opt.*, vol. 52, no. 18, pp. 4186-4191, Jun. 2013.

[21] Virginia Diodes, www.vadiodes.com (accessed Jun. 8, 2020).

[22] Terasense, www.terasense.com (accessed Jun. 8, 2020).

[23] M. T. San, K. Ogura, K. Kubota, Y. Annaka, K. Yambe, and A. Sugawara, "Study on operation of oversized backward wave oscillator for broadband terahertz radiation," *IEEE T. Plasma Sci.*, vol. 46, no. 3, pp. 530-538, Feb. 2018.

[24] X. Wang, C. Shen, T. Jiang, Z. Zhan, Q. Deng, W. Li, W. Wu, N. Yang, W. Chu, and S. Duan, "High-power terahertz quantum cascade lasers with~ 0.23 W in continuous wave mode," *AIP Adv.*, vol. 6, no. 7, pp. 075210, Jul. 2016.

[25] U. Strom, J. R. Hendrickson, R. J. Wagner, and P. C. Taylor, "Disorder-induced far infrared absorption in amorphous materials," *Solid State Commun.*, vol. 15, no. 11-12, pp. 1871-1875, Dec. 1974.

[26] D. H. Auston, K. P. Cheung, and P. R. Smith, "Picosecond photoconducting Hertzian dipoles," *Appl. Phys. Lett.*, vol. 45, no. 3, pp. 284-286, Aug. 1984.

[27] A. Podzorov, and G. Gallot, "Density of states and vibrational modes of PDMS studied by terahertz time-domain spectroscopy," *Chem. Phys. Lett.*, 495, 46 (2010).

[28] S. Wietzke, C. Jansen, F. Rutz, D. M. Mittleman, and M. Koch, "Determination of additive content in polymeric compounds with terahertz time-domain spectroscopy," *Polym. Test.*, vol. 26, no. 5, pp. 614-618, Aug. 2007.

[29] A. Sengupta, A. Bandyopadhyay, B. F. Bowden, J. A. Harrington, and J. F. Federici, "Characterisation of olefin copolymers using terahertz spectroscopy," *Electron. Lett.*, vol. 42, no. 25, pp. 1477-1479, Dec. 2006.

[30] D. Grischkowsky, S. Keiding, M. Van Exter, and C. Fattinger, "Far-infrared time-domain spectroscopy with terahertz beams of dielectrics and semiconductors," *J. Opt. Soc. Am. B*, vol. 7, no. 10, pp. 2006-2015, Oct. 1990.

[31] S. Wietzke, C. Jansen, M. Reuter, T. Jung, D. Kraft, S. Chatterjee, B. M. Fischer, and M. Koch, "Terahertz spectroscopy on polymers: A review of morphological studies," *J. Mol. Struct.*, vol. 1006, no. 1-3, pp. 41-51, Dec. 2011.

[32] M. Naftaly, and R. E. Miles, "Terahertz time-domain spectroscopy for material characterization," *Proc. IEEE*, vol. 95, no. 8, pp. 1658-1665, Aug. 2007.

[33] N. Krumbholz, T. Hochrein, N. Vieweg, T. Hasek, K. Kretschmer, M. Bastian, M. Mikulics, and M. Koch, "Monitoring polymeric compounding processes inline with THz time-domain spectroscopy," *Polym. Test.*, vol. 28, no. 1, pp. 30-35, Feb. 2009.

[34] D. M. Mittleman, "Twenty years of terahertz imaging," Opt. Express, vol. 26, no. 8, pp. 9417-9431, Apr. 2018.

[35] H. Shams, K. Balakier, L. Gonzalez-Guerrero, M. J. Fice, L. Ponnampalam, C. S. Graham, C. C. Renaud, and A. J. Seeds, "Optical frequency tuning for coherent THz wireless signals," *J. Lightwave Technol.*, vol. 36, no. 19, pp. 4664-4670, Oct. 2018.

[36] H. Shams, M. J. Fice, L. Gonzalez-Guerrero, C. C. Renaud, F. van Dijk, and A. J. Seeds, "Sub-THz wireless over fiber for frequency band 220–280 GHz," *J. Lightwave Technol.*, vol. 34, no. 20, pp. 4786-4793, Apr. 2016.

[37] C. Jastrow, K. Mu, R. Piesiewicz, T. Ku, M. Koch, and T. Kleine-Ostmann, "300 GHz transmission system," *Electron. Lett.*, vol. 44, no. 3, pp. 213-214, Feb. 2008.

[38] B. Born, I. R. Hristovski, S. Geoffroy-Gagnon, and J. F. Holzman, "All-optical retro-modulation for free-space optical communication," *Opt. Express*, vol. 26, no. 4, pp. 5031-5042, Feb. 2018.

[39] C. M. Swenson, C. A. Steed, A. Imelda, and R. Q. Fugate, "Low-power FLC-based retromodulator communications system," in *Free-Space Laser Communication Technologies IX*, San Jose, CA, USA, Apr. 1997, pp. 296-310.

[40] X. Jin, B. A. Hristovski, C. M. Collier, S. Geoffroy-Gagnon, B. Born, and J. F. Holzman, "Ultrafast all-optical technologies for bidirectional optical wireless communications," *Opt. Lett.*, vol. 40, no. 7, pp. 1583-1586, Apr. 2015.

[41] X. Jin, C. M. Collier, J. J. Garbowski, B. Born, and J. F. Holzman, "Ultrafast transient responses of optical wireless communication detectors," *Appl. Opt.*, vol. 52, no. 20, pp. 5042-5049, Jul. 2013.

[42] X. Jin, J. E. Barg, and J. F. Holzman, "Retro-detective control structures for free-space optical communication links," *Opt. Express*, vol. 17, no. 26, pp. 23867-23872, Dec. 2009.

[43] J. A. Shaw, "Radiometry and the Friis transmission equation," *Am. J. Phys.*, vol. 81, no. 1, pp. 33-37, Jan. 2013.

[44] B. Born, J. D. Krupa, S. Geoffroy-Gagnon, and J. F. Holzman, "Integration of photonic nanojets and semiconductor nanoparticles for enhanced all-optical switching," *Nat. Commun.*, vol. 6, p. 8097, Aug, 2015.

[45] C. M. Collier, X. Jin, J. F. Holzman, and J. Cheng, "Omni-directional characteristics of composite retroreflectors," *J. Opt. A-Pure Appl. Opt.*, vol. 11, no. 8, p. 085404, May 2009.

[46] N. Gopalsami, and A. C. Raptis, "Millimeter-wave radar sensing of airborne chemicals," *IEEE Trans. Microw. Theory Tech.*, vol. 49, no. 4, pp. 646-653, Apr. 2001.

[47] R. J. Williams, "Frequency selective terahertz retroreflectors," PhD Dissertation, Department of Physics and Applied Physics, University of Massachusetts, Lowell, MA, USA, 2014.

[48] D. Desai, "Passive planar terahertz retroreflectors," M.S. thesis, New Jersey Institute of Technology, Newark, NJ, USA, 2018.

[49] H. T. Chen, J. F. O'hara, A. K. Azad, A. J. Taylor, R. D. Averitt, D. B. Shrekenhamer, and W. J. Padilla, "Experimental demonstration of frequency-agile terahertz metamaterials," *Nat. Photon.*, vol. 2, no. 5, p. 295, May 2008.

[50] M. H. Bergen and J. F. Holzman, "Terahertz time-domain spectroscopy for ultrafast and quasi-static characterizations of germanium," *IEEE T. THz Sci. Technol.*, vol. 11, no. 1, pp. 54-61, Jan. 2021.

[51] Q. Y. Wen, W. Tian, Q. Mao, Z. Chen, W. W. Liu, Q. H. Yang, M. Sanderson, and H. W. Zhang, "Graphene based all-optical spatial terahertz modulator," *Sci. Rep.*, vol. 4, pp. 7409, Dec. 2014.

[52] P. Weis, J. L. Garcia-Pomar, M. Hoh, B. Reinhard, A. Brodyanski, and M. Rahm, "Spectrally wide-band terahertz wave modulator based on optically tuned graphene," *ACS Nano*, vol. 6, no. 10, pp. 9118-9124, Oct. 2012.

[53] Y. Zhang, S. Qiao, S. Liang, Z. Wu, Z. Yang, Z, Feng, H. Sun, Y. Zhou, L. Sun, Z. Chen, and X. Zou, "Gbps terahertz external modulator based on a composite metamaterial with a double-channel heterostructure," *Nano Lett.*, vol. 15, no. 5, pp. 3501-3506, May 2015.

[54] O. Paul, C. Imhof, B. Lägel, S. Wolff, J. Heinrich, S. Höfling, A. Forchel, R. Zengerle, R. Beigang, and M. Rahm, "Polarization-independent active metamaterial for high-frequency terahertz modulation," *Opt. Express*, vol. 17, no. 2, pp. 819-827, Jan. 2009.

[55] Z. Zhou, S. Wang, Y. Yu, Y. Chen, and L. Feng, "High performance metamaterials-high electron mobility transistors integrated terahertz modulator," *Opt. Express*, vol. 25, no. 15, pp. 17832-17840, Jul 2017.

[56] H. T. Chen, W. J. Padilla, J. M. Zide, A. C. Gossard, A. J. Taylor, and R. D. Averitt, "Active terahertz metamaterial devices," *Nature*, vol. 444, no. 7119, pp. 597-600, Nov. 2006.

[57] R. A. Lewis, "A review of terahertz sources," *J. Phys. D Appl. Phys.*, vol. 47, no. 37, pp. 374001, Aug. 2014.

[58] R. A. Lewis "A review of terahertz detectors," *J. Phys. D Appl. Phys.*, vol. 52, no. 43, pp. 433001, Aug. 2019.

[59] H. Elayan, O. Amin, B. Shihada, R. M. Shubair, and M. S. Alouini, "Terahertz band: The last piece of RF spectrum puzzle for communication systems," *IEEE Open J. Commun. Soc.*, vol. 1, pp. 1-32, Nov. 2019.

[60] S. S. Dhillon, M. S. Vitiello, E. H. Linfield, A. G. Davies, M. C. Hoffmann, J. Booske, C. Paoloni, M. Gensch, P. Weightman, G. P. Williams, and E. Castro-Camus, "The 2017 terahertz science and technology roadmap," *J. Phys. D Appl. Phys.*, vol. 50, no. 4, pp. 043001, Jan. 2017.

[61] L. Bosco, M. Franckié, G. Scalari, M. Beck, A. Wacker, and J. Faist, "Thermoelectrically cooled THz quantum cascade laser operating up to 210 K," *Appl. Phys. Lett.*, vol. 115, no. 1, pp. 010601, Jul. 2019.

[62] C. A. Curwen, J. L. Reno, and B. S. Williams, "Broadband continuous single-mode tuning of a short-cavity quantum-cascade VECSEL," *Nat. Photon.*, vol. 13, no. 12, pp. 855-859, Dec. 2013.

[63] X. Xu, Y. Wei, F. Shen, H. Yin, J. Xu, Y. Gong, and W. Wang, "A watt-class 1-THz backward-wave oscillator based on sine waveguide," *Phys. Plasmas*, vol. 19, no. 1, pp. 013113, Jan. 2012.

[64] N. Alijabbari, M. F. Bauwens, and R. M. Weikle, "Design and characterization of integrated submillimeter-wave quasi-vertical Schottky diodes," *IEEE T. THz Sci. Technol.*, vol. 5, no. 1, pp. 73-80, Oct. 2014.

[65] I. Mehdi, J. V. Siles, C. Lee, and E. Schlecht, "THz diode technology: status, prospects, and applications," *P. IEEE*, vol. 105, no. 6, pp. 990-1007, Jan. 2017.

[66] X. Y. Zhang, L. A. Yang, Y. Ma, Y. C. Liu, W. L. Yang, X. H. Ma, and Y. Hao, "Noise characteristics of Ni/GaN Schottky barrier IMPATT diode based on polar-and nonpolar-oriented wurtzite GaN for terahertz application," *Superlattice Microst.*, vol. 139, pp. 106405, Jan. 2020.

[67] A. Khalid, G. M. Dunn, R. F. Macpherson, S. Thoms, D. Macintyre, C. Li, M. J. Steer, V. Papageorgiou, I. G. Thayne, M. Kuball, and C. H. Oxley, "Terahertz oscillations in an In0.53Ga0.47As submicron planar Gunn diode," *J. Appl. Phys.*, vol. 115, no. 11, pp. 114502, Mar. 2014.

[68] M. Rochat, J. Faist, M. Beck, U. Oesterle, and M. Ilegems, "Far-infrared (λ= 88 μ m) electroluminescence in a quantum cascade structure," *Appl. Phys. Lett.*, vol. 73, no. 25, pp. 3724-3726, Dec. 1998.

[69] A. Biswas, S. Sinha, A. Acharyya, A. Banerjee, S. Pal, H. Satoh, and H. Inokawa, "1.0 THz GaN IMPATT source: Effect of parasitic series resistance," *J. Infrared Millim. Terahertz Waves*, vol. 39, no. 10, pp. 954-974, Oct. 2018.

[70] S. P. Singh, G. A. Kumar, and B. Biswas, "Design and optimization of a tunable W-band subharmonic cavity based Gunn diode oscillator using computer-aided design technique," *Int. J. RF and Microw. C. E.*, vol. 29, no. 9, p. e21862, Sep. 2019.

[71] M. Urteaga, Z. Griffith, M. Seo, J. Hacker, and M. J. Rodwell, "InP HBT technologies for THz integrated circuits," *Proc. IEEE*, vol. 105, no. 6, pp. 1051-1067, May 2017.

[72] A. El Fatimy, R. L. Myers-Ward, A. K. Boyd, K. M. Daniels, D. K. Gaskill, and P. Barbara, "Epitaxial graphene quantum dots for high-performance terahertz bolometers," *Nat. Nanotechnol.*, vol. 11, no. 4, pp. 335, Apr. 2016.

[73] P. S. Stefanova, J. M. Hammler, A. K. Klein, A. J. Gallant, and C. Balocco, "Polymer-based micro-golay cells for THz detection," in *41st Int. Conf. on Infrared, Millimeter, and Terahertz waves*, Copenhagen, Denmark, 2016, pp. 1-2.

[74] H. Li, W. J. Wan, Z. Y. Tan, Z. L. Fu, H. X. Wang, T. Zhou, Z. P. Li, C. Wang, X. G. Guo, and J. C. Cao, "6.2-GHz modulated terahertz light detection using fast terahertz quantum well photodetectors," *Sci. Rep.*, vol. 7, no. 1, pp. 1-8, Jun. 2017.

[75] V. Mackowiak, J. Peupelmann, Y. Ma, and A. Gorges, "NEP–noise equivalent power," Thorlabs Inc., [White Paper], 2015.

[76] Y. Yang, M. Mandehgar, and D. Grischkowsky, "THz-TDS characterization of the digital communication channels of the atmosphere and the enabled applications," *J. Infrared, Millim., Terahertz Waves*, vol. 36, no. 2, pp. 97-129, Feb. 2015.

[77] "Attenuation by atmospheric gases and related effects," International Telecommunication Union, Geneva, Switzerland, Recommendation ITU-R P.676-12 (08/2019), Accessed: Jun. 8, 2020. [Online]. Available: https://www.itu.int/rec/R-REC-P.676-12-201908-I/en

[78] J. P. Oakley, "Whole-angle spherical retroreflector using concentric layers of homogeneous optical media," *Appl. Opt.*, vol. 46, no. 7, pp. 1026-1031, Mar. 2007.

[79] D. Kucharski, G. Kirchner, H. C. Lim, and F. Koidl, "Optical response of nanosatellite BLITS measured by the Graz 2 kHz SLR system," *Adv. Space Res.*, vol. 48, no. 8, pp. 1335-1340, Oct. 2011.

[80] M. Naftaly, and R. Dudley, "Terahertz reflectivities of metal-coated mirrors," *Appl. Opt.*, vol. 50, no 19, pp. 3201-3204, Jul. 2011.

[81] E. A. Tanner, D. J. Phillips, C. M. Persons, F. C. De Lucia, and H. O. Everitt, "Design and signature analysis of remote trace-gas identification methodology based on infrared-terahertz double-resonance spectroscopy," *Phys. Rev. Appl.*, vol. 2, no. 5, p. 054016, Nov. 2014.

[82] V. S. Hsu, J. M. Kahn, and K. S. Pister, "MEMS corner cube retroreflectors for free-space optical communications," *University of California Publication*, Oct. 1999, pp. 1-53.

[83] L. Zhou, J. M. Kahn, and K. S. Pister, "Corner-cube retroreflectors based on structure-assisted assembly for free-space optical communication," *J. Microelectromech. Syst.*, vol. 12, no. 3, pp. 233-242, Jun. 2003.

[84] T. Takatsuji, M. Goto, S. Osawa, R. Yin, and T. Kurosawa, "Whole-viewing-angle cat's-eye retroreflector as a target of laser trackers," *Meas. Sci. Technol.*, vol. 10, no. 7, p. N87, Jul. 1999.

[85] B. E. Bernacki, N. C. Anheier, K. Krishnaswami, B. D. Cannon, and K. B. Binkley, "Design and fabrication of efficient miniature retroreflectors for the mid-and long-range infrared," in *Infrared Technology and Applications XXXIV*, Orlando, FL, USA, May 2008, vol. 6940, p. 69400X.

[86] S. F. Busch, M. Weidenbach, J. C. Balzer, and M. Koch, "THz optics 3D printed with TOPAS," *J. Infrared Millim. Terahertz Waves*, vol. 37, no. 4, pp. 303-307, Apr. 2016.

[87] B. Ung, A. Dupuis, K. Stoeffler, C. Dubois, and M. Skorobogatiy, "High-refractive-index composite materials for terahertz waveguides: trade-off between index contrast and absorption loss," *J. Opt. Soc. Am. B*, vol. 28, no. 4, pp. 917-921, Apr. 2011.

[88] G. Zhang, H. Zhang H, H. Wei, S. Zhu, Z. Wu, Z. Wang, F. Jia, J. Zhang, and B. Yang, "Creation of transparent nanocomposite films with a refractive index of 2.3 using polymerizable silicon nanoparticles," *Part. Part. Syst. Charact.*, vol. 30, no. 8, pp. 653-657, Aug. 2013.

[89] M. M. Nazarov, E. V. Khaydukov, A. G. Savelyev, V. I. Sokolov, A. S. Akhmanov, A. P. Shkurinov, and V. Y. Panchenko, "Terahertz response of a polymer composite with high concentration of silicon micro-and nanoparticles," *Nanotechnol. Russ.*, vol. 10, no. 3-4, pp. 247-253, Mar. 2015.

[90] D. Headland, P. Thurgood, D. Stavrevski, W. Withayachumnankul, D. Abbott, M. Bhaskaran, and S. Sriram, "Doped polymer for low-loss dielectric material in the terahertz range," *Opt. Mater. Express*, vol. 5, no. 6, pp. 1373-1380, Jun. 2015.

[91] P. H. Bolivar, M. Brucherseifer, J. G. Rivas, R. Gonzalo, I. Ederra, A. L. Reynolds, M. Holker, and P. de Maagt, "Measurement of the dielectric constant and loss tangent of high dielectric-constant materials at terahertz frequencies," *IEEE Trans. Microw. Theory Tech.*, vol. 51, no. 4, pp. 1062-1066, Apr. 2003.

[92] C. Jansen, S. Wietzke, V. Astley, D. M. Mittleman, and M. Koch, "Mechanically flexible polymeric compound one-dimensional photonic crystals for terahertz frequencies," *Appl. Phys. Lett.*, vol. 96, no. 11, p. 111108, Mar. 2010.

[93] M. Scheller, S. Wietzke, C. Jansen, and M. Koch, "Modelling heterogeneous dielectric mixtures in the terahertz regime: a quasi-static effective medium theory," *J. Phys. D Appl. Phys.*, vol. 42, no. 6, pp. 065415, Mar. 2009.

[94] J. Lott, C. Xia, L. Kosnosky, C. Weder, and J. Shan, "Terahertz photonic crystals based on barium titanate/polymer nanocomposites," *Adv. Mater.*, vol. 20, no. 19, pp. 3649-3653, Oct. 2008.

[95] M. Kaushik, B. W. Ng, B. M. Fischer, and D. Abbott, "Terahertz scattering by granular composite materials: An effective medium theory," *Appl. Phys. Lett.*, vol. 100, no.1, pp. 011107, Jan. 2012.

[96] J. Lloyd-Hughes and T. I. Jeon, "A review of the terahertz conductivity of bulk and nano-materials," *J. Infrared Millim. Terahertz Waves*, vol. 33, no. 9, pp. 871–925, Sep. 2012.

[97] D. Polder, J. H. Van Santeen, "The effective permeability of mixtures of solids," *Physica*, vol. 12, no. 5, pp. 257-271, Aug. 1946.

[98] X. Wang, Y. Li, B. Cai, and Y. Zhu, "High refractive index composite for broadband antireflection in terahertz frequency range," *Appl. Phys. Lett.*, vol. 106, no. 23, pp. 231107, Jun. 2015.

[99] G. Banhegyi, "Comparison of electrical mixture rules for composites," *Colloid Polym. Sci.*, vol. 264, no. 12, pp. 1030-1050, Dec. 1986.

[100] A. Sihvola, "Dielectric polarization and particle shape effects," *J. Nanomater*, vol. 1, pp. 5, May 2007.

[101] C. T. Phare, Y. H. Lee, J. Cardenas, and M. Lipson, "Graphene electro-optic modulator with 30 GHz bandwidth," *Nat. Photon.*, vol. 9, no. 8, pp. 511-514, Aug. 2015.

[102] M. Liu, X. Yin, E. Ulin-Avila, B. Geng, T. Zentgraf, L. Ju, F. Wang, and X. Zhang, "A graphene-based broadband optical modulator," *Nature*, vol. 474, no. 7349, pp. 64-67, Jun. 2011.

[103] I. Libon, S. Baumgärtner, M. Hempel, N. E. Hecker, J. Feldmann, M. Koch, and P. Dawson, "An optically controllable terahertz filter," *Appl. Phys. Lett.*, vol. 76, no. 20, pp. 2821-2823, May 2000.

[104] W. S. Rabinovich, R. Mahon, P. G. Goetz, E. Waluschka, D. S. Katzer, S. C. Binari, and G. C. Gilbreath, "A cat's eye multiple quantum-well modulating retro-reflector," *IEEE Photon. Technol. Lett.*, vol. 15, no. 3, pp. 461-463, Mar. 2003.

[105] W. S. Rabinovich, G. C. Gilbreath, P. G. Goetz, R. Mahon, D. S. Katzer, K. Ikossi-Anastasiou, S. C. Binari, T. J. Meehan, M. Ferraro, I. Sokolsky, and J. A. Vasquez, "InGaAs multiple quantum well modulating retro-reflector for free-space optical communications," in *Free-Space Laser Communication and Laser Imaging*, San Diego, CA, USA, Jan. 2002, vol. 4489, pp. 190-202.

[106] H. T. Chen, S. Palit, T. Tyler, C. M. Bingham, J. M. Zide, J. F. O'Hara, D. R. Smith, A. C. Gossard, R. D. Averitt, J. W. Padilla, and N. M. Jokerst, "Hybrid metamaterials enable fast electrical modulation of freely propagating terahertz waves," *Appl. Phys. Lett.*, vol. 93, no. 9, p. 091117, Sep. 2008.

[107] H. T. Chen, H. Lu, A. K. Azad, R. D. Averitt, A. C. Gossard, S. A. Trugman, J. F. O'Hara, and A. J. Taylor, "Electronic control of extraordinary terahertz transmission through subwavelength metal hole arrays," *Opt. Express*, vol. 16, no. 11, pp. 7641-7648, May 2008.

[108] T. Kleine-Ostmann, P. Dawson, K. Pierz, G. Hein, and M. Koch, "Room-temperature operation of an electrically driven terahertz modulator," *Appl. Phys. Lett.*, vol. 84, no. 18, pp. 3555-3557, May 2004.

[109] L. Wang, X. W. Lin, W. Hu, G. H. Shao, P. Chen, L. J. Liang, B. B. Jin, P. H. Wu, H. Qian, Y. N. Lu, and X. Liang, "Broadband tunable liquid crystal terahertz waveplates driven with porous graphene electrodes," *Light Sci. Appl.*, vol. 4, no. 2, pp. e253, 2015.

[110] Y. F. Chen, B. J. Yang, and J. C. Tsai, "Surface-micromachined MEMS tunable three-leaf trefoil-type corner cube retro-reflector for free-space optical applications," *IEEE J. Sel. Topics Quantum Electron.*, vol. 21, no. 4, pp. 123-129, 2015.

[111] J. Cong, G. Zheng, Z. Zhou, M. Liu, M. Chen, H. Yao, P. Wei, and N. Ren, "Analytical model of terahertz metasurface for enhanced amplitude modulation," *J. Phys. D Appl. Phys.*, vol. 51, no. 34, pp. 345101, Jul. 2018.

[112] L. Cong, Y. K. Srivastava, H. Zhang, X. Zhang, J. Han, and R. Singh, "All-optical active THz metasurfaces for ultrafast polarization switching and dynamic beam splitting," *Light Sci. Appl.*, vol. 7, no. 1, pp. 1-9, Jul. 2018.

[113] J. H. Strait, P. A. George, M. Levendorf, M. Blood-Forsythe, F. Rana, and J. Park, "Measurements of the carrier dynamics and terahertz response of oriented germanium nanowires using optical-pump terahertz-probe spectroscopy," *Nano Lett.*, vol. 9, no. 8, pp. 2967–2972, 2009.

[114] P. A. George, J. Strait, J. Dawlaty, S. Shivaraman, M. Chandrashekhar, F. Rana, and M. G. Spencer, "Ultrafast optical-pump terahertz-probe spectroscopy of the carrier relaxation and recombination dynamics in epitaxial graphene," *Nano Lett.*, vol. 8, no. 12, pp. 4248-4251, Nov. 2008.

[115] G. Isić, G. Sinatkas, D. C. Zografopoulos, B. Vasić, A. Ferraro, R. Beccherelli, E. E. Kriezis, and M. Belić, "Electrically tunable metal–semiconductor–metal terahertz metasurface modulators," *IEEE J. Sel. Top. Quantum Electron.*, vol. 25, no. 3, pp. 1-8, Jan. 2019.

[116] H. T. Chen, W. J. Padilla, M. J. Cich, A. K. Azad, R. D. Averitt, and A. J. Taylor, "A metamaterial solid-state terahertz phase modulator," *Nat. Photonics*, vol. 3, no. 3, p. 148, Mar. 2009.

[117] M. C. Nuss and J. Orenstein, "Terahertz time-domain spectroscopy," *Millimeter and submillimeter wave spectroscopy of solids*, Springer, 1998, pp. 7-50.

[118] C. M. Collier, T. J. Stirling, I. R. Hristovski, J. D. Krupa, and J. F. Holzman, "Photoconductive terahertz generation from textured semiconductor materials," *Sci. Rep.*, vol. 6, no. 1, pp. 1-10, Mar. 2016.

[119] K. Aoki, J. Savolainen, and M. Havenith, "Broadband terahertz pulse generation by optical rectification in GaP crystals," *Appl. Phys. Lett.*, vol. 110, no. 20, pp. 201103, May 2017.

[120] V. Apostolopoulos and M. E. Barnes, "THz emitters based on the photo-Dember effect," *J. Phys. D-Appl. Phys.*, vol. 47, no. 37, p. 374002, Aug. 2014.

[121] G. Gallot, J. Zhang, R. W. McGowan, T. I. Jeon, and D. Grischkowsky, "Measurements of the THz absorption and dispersion of ZnTe and their relevance to the electro-optic detection of THz radiation," *Appl. Phys. Lett.*, vol. 74, no. 23, pp. 3450-3452, Jun. 1999.

[122] N. I. Lesack, N. V. Fredeen, A. Jirasek, and J. F. Holzman, "A methodology for dynamic material characterizations via terahertz time-domain spectroscopy," *IEEE Trans. Microw. Theory Tech.*, vol 10, no. 3, pp. 282-291, Feb. 2020.

[123] M. Naftaly and R. Dudley, "Methodologies for determining the dynamic ranges and signal-to-noise ratios of terahertz time-domain spectrometers," *Opt. Lett.*, vol. 34, no. 8, pp. 1213-1215, Apr. 2009.

[124] M. H. Bergen, J. Reich, T. Ho, F. Clark, M. Reid, and J. F. Holzman, "Terahertz field depolarization and absorption within composite media," *Appl. Phys. Lett.*, vol. 115, no. 4, pp. 041901, Jul. 2019.

[125] M. Z. Rong, M. Q. Zhang, and W. H. Ruan, "Surface modification of nanoscale fillers for improving properties of polymer nanocomposites: A review," *J. Mater. Sci. Technol.*, vol. 22, no. 7, pp. 787-796, Jul. 2006.

[126] D. Bera, L. Qian, T. K. Tseng, and P. H. Holloway, "Quantum dots and their multimodal applications: A review," *Materials*, vol. 3, no. 4, pp. 2260, Apr. 2010.

[127] D. M. Johansen, "Investigation of Topas for use in optical components," Master's thesis, Tech. Univ. Denmark, 2005.

[128] P. A. George, W. Hui, F. Rana, B. G. Hawkins, A. E. Smith, and B. J. Kirby, "Microfluidic devices for terahertz spectroscopy of biomolecules," *Opt. Express*, vol. 16, no. 3, pp. 1577-1582, Feb. 2008.

[129] S. Alfihed, M. H. Bergen, A. Ciocoiu, J. F. Holzman, and I. G. Foulds, "Characterization and integration of terahertz technology within microfluidic platforms," *Micromachines*, vol. 9, no. 9, pp. 453, Sep. 2018.

[130] S. Tsuzuki, N. Kuzuu, H. Horikoshi, K. Saito, K. Yamamoto, and M. Tani, "Influence of OH-group concentration on optical properties of silica glass in terahertz frequency region," *Appl. Phys. Express*, vol. 8, no. 7, p. 072402, Jun. 2015.

[131] C. J. Kaplan, P. M. Kraus, A. D. Ross, M. Zürch, S. K. Cushing, M. F. Jager, H. T. Chang, E. M. Gullikson, D. M. Neumark, and S. R. Leone, "Femtosecond tracking of carrier relaxation in germanium with extreme ultraviolet transient reflectivity," *Phys. Rev. B*, vol. 97, no. 20, pp. 205202, May 2018.

[132] A. Kannegulla, M. I. Shams, L. Liu, and L. J. Cheng, "Photo-induced spatial modulation of THz waves: opportunities and limitations," *Opt. Express*, vol. 23, no. 25, pp. 32098, Dec. 2015.

[133] B. Streetman, *Solid state electronic devices*, 4th Ed. Englewood Cliffs, NJ, USA: Prentice Hall 1995, p. 439 and p. 87.

[134] N. E. Posthuma, G. Flamand, W. Geens, and J. Poortmans, "Surface passivation for germanium photovoltaic cells," *Sol. Energy Mater. Sol. Cells*, vol. 88, no. 1, pp. 37–45, Jun. 2005.

[135] Y. Y. Chen, H. C. Chang, Y. H. Chi, C. H. Huang, and C. W. Liu, "GeO_2 passivation for low surface recombination velocity on Ge surface," *IEEE Electron Device Lett.*, vol. 34, no. 3, pp. 444–446, 2013.

[136] E. Gaubas and J. Vanhellemont, "Dependence of carrier lifetime in germanium on resistivity and carrier injection level," *Appl. Phys. Lett*., vol. 89, no. 14, pp. 142106, 2006.

[137] J. F. Holzman, P. Strasser, R. Wuest, F. Robin, D. Erni, and H. Jackel, "Picosecond free-carrier recombination in indium phosphide photonic crystals," in *International* Conference *on Indium Phosphide and Related Materials*, Glasgow, Scotland, UK, 2005, pp. 570-573.

[138] J. Shakya, J. Y. Lin, and H. X. Jiang, "Time-resolved electroluminescence studies of III-nitride ultraviolet photonic-crystal light-emitting diodes," *Appl. Phys. Lett.*, vol. 85, no. 11, pp. 2104–2106, Sep. 2004.

[139] J. P. McKelvey and R. L. Longini, "Volume and surface recombination rates for injected carriers in germanium," *J. Appl. Phys.*, vol. 25, no. 5, pp. 634–641, May 1954.

[140] K. Berdel, J. G. Rivas, P. H. Bolívar, P. De Maagt, and H. Kurz, "Temperature dependence of the permittivity and loss tangent of high-permittivity materials at terahertz frequencies," *IEEE Trans. Microw. Theory Tech.*, vol. 53, no. 4, pp. 1266-1271, Apr. 2005.

Appendix A: Drude Free Carrier Absorption Model for Metals

In this appendix, the derivation for Drude free carrier absorption is presented in additional detail. The Drude free carrier absorption models the motion of charge carriers assuming these charge-carriers are not bound to their nuclei. When subject to an applied force, F_{Applied}, from an external electric field, E_{Applied}, the dynamics of these charge-carriers depends on only their inertia and a damping force, F_{Damp}, resulting from their interactions with each other and with the lattice. The force equations are

$$F_{\text{Applied}} = qE_{\text{Applied}} \tag{A1.1}$$

and

$$F_{\text{Damp}} = -\frac{m^*_{\text{e/h}}}{\tau_{\text{s,e/h}}}\frac{dx}{dt}, \tag{A1.2}$$

giving the total equation of motion, which is the sum of forces, to be

$$m^*_{\text{e/h}}\frac{d^2x}{dt^2} + \frac{m^*_{\text{e/h}}}{\tau_{\text{s,e/h}}}\frac{dx}{dt} = qE_{\text{Applied}}\,. \tag{A1.3}$$

This linear ordinary differential equation can be solved by assuming harmonic oscillation in both the charge-carrier displacement, x, and the applied electric field, E_{Applied}. Doing so, gives a charge-carrier displacement, x, and an applied electric field, E_{Applied}, to be

$$x = x_o e^{j\omega t}, \tag{A1.4}$$

and

$$E_{\text{Applied}} = E_o e^{j\omega t}\,. \tag{A1.5}$$

Inserting (A1.4) and (A1.5) into (A1.3) and cancelling out $e^{-j\omega t}$ from all terms give the equation of motion for the charge carriers to be

$$-m_{e/h}^{*}\omega^{2}x_{o}+j\frac{m_{e/h}^{*}}{\tau_{s,e/h}}\omega x_{o}=qE_{o}. \tag{A1.6}$$

Solving (A1.6) for the maximum charge-carrier displacement, x_o, gives

$$x_{o}=\frac{-qE_{o}}{m_{e/h}^{*}\omega(\omega+j(1/\tau_{s,e/h}))}. \tag{A1.7}$$

This is the solution for the maximum charge-carrier displacement under an applied electric field. This maximum displacement creates a dipole moment, p, which is defined for a single charge to be

$$p=x_{o}q=\frac{-q^{2}E_{o}}{m_{e/h}^{*}\omega(\omega+j(1/\tau_{s,e/h}))} \tag{A1.8}$$

The dipole volume density, also known as polarization, is the sum of the contributions of $N(t)$ identical dipoles per unit volume. Summing these dipoles gives

$$P=\frac{-q^{2}N(t)E_{o}}{m_{e/h}^{*}\omega(\omega+j(1/\tau_{s,e/h}))}, \tag{A1.9}$$

which is the time varying polarization in the charge-carrier plasma. This can also be written in terms of the susceptibility for either electrons or holes, $\chi_{e/h}$, as

$$P=\varepsilon_{o}\chi_{e/h}E_{o}=\frac{-q^{2}N(t)E_{o}}{m_{e/h}^{*}\omega(\omega+j(1/\tau_{s,e/h}))}. \tag{A1.10}$$

Solving for susceptibility gives

$$\chi_{e/h} = \frac{-q^2 N(t)}{\varepsilon_o m^*_{e/h} \omega(\omega + j(1/\tau_{s,e/h}))}, \tag{A1.11}$$

which is the equation given in (2.4a) and (2.4b) for electrons and holes, respectively.

Appendix B: Material Parameter Extraction

Extraction of material parameters from THz TDS scans is a challenging task to accomplish in general. The internal reflections within the sample prevent the derivation of a closed form solution for refractive index and extinction coefficient. While iterative algorithms exist to solve (4.1), these are typically not required. It can be shown that the error introduced into the extinction coefficient using the simplified expressions is equal to

$$-\ln\left[\frac{1}{1-2r(\omega)^2 e^{-2k_0\kappa(\omega)\delta}\cos(2k_0 n(\omega)\delta)+r(\omega)^4 e^{-4k_0\kappa(\omega)\delta}}\right]\frac{c}{\omega\delta}. \tag{A2.1}$$

Interestingly, the same amount error is introduced into the refractive index as is introduced into the extinction coefficient, though the error phase shifted in the frequency domain by $\pi/2$. Consequently, etalon induced errors are much more noticeable in extinction coefficient since the background refractive index is typically several orders of magnitude larger than background extinction coefficient.

The most challenging material to extract parameters from is one with a high refractive index and a negligible extinction coefficient, which is common for many semiconductors. Spectroscopy of these materials can still be carried out if one can assume that the refractive index of the material is constant over the frequency of interest. In this case, the etalons can be compensated for by modelling the material with a constant estimated refractive index, n_E, and zero extinction coefficient. The estimated expressions for the compensated refractive index, $n_c(\omega)$, and extinction coefficient, $\kappa_c(\omega)$, with etalon effects are

$$n_c(\omega)=1+\left(\phi_{THz}(\omega)+\phi_E(\omega)+2\pi i\right)\frac{c}{\omega\delta} \tag{A2.2}$$

and

$$\kappa_c(\omega)=-\ln\left[\frac{E(\omega)E_E(\omega)}{t_{in}(\omega)t_{out}(\omega)E_0(\omega)}\right]\frac{c}{\omega\delta}, \tag{A2.3}$$

where $\phi_E(\omega)$ and $E_E(\omega)$ are the estimated phase and amplitude, respectively, introduced by the presence of internal reflections. The estimated amplitude and phase shift can be determined using

$$E_E(\omega)e^{-j\phi_E} = \frac{1}{1-r_E(\omega)^2 e^{-j2k_0 n_E \delta}}. \tag{A3.3}$$

To show the potential effect that etalons have on the measured refractive index and extinction coefficient, a sample of intrinsic germanium was measured with a thickness of 320 μm. Germanium, with its high refractive index and low extinction coefficient, produces very large etalons. Figure 7.1 below shows the results for parameter extraction with (Compensated) and without (Uncompensated) etalon estimation.

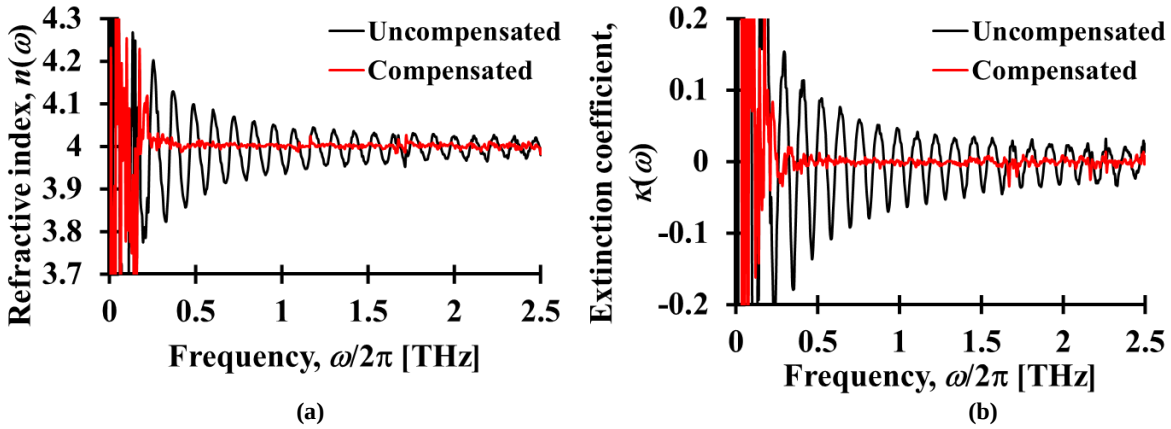

Figure 7.1: The extracted refractive index (a) and extinction coefficient (b) for an intrinsic germanium wafer is shown. The material parameters are extracted using two algorithms. One algorithm does not compensate for etalons (Uncompensated), while the other algorithm compensates for etalons by assuming a constant refractive index (Compensated).

The effects of etalons for this sample are clearly visible in both the refractive index and extinction coefficient of the parameters extracted without etalon compensation, as they are much larger than the measurement noise. Conversely, the results with etalon estimation push the internal reflections mostly into the measurement noise floor, and flat refractive index and extinction spectra are produced. This level of improvement in spectroscopy results is only possible when the refractive index of the sample is large and constant. Owing to the large etalons seen in germanium, the modulator results in Chapter 5 were analysed including internal reflections.

Etalon estimation can also be used to for samples with lower refractive indices, but this does not produce the same dramatic effects. The following results are for a composite sample with a volumetric fraction of approximately 8% of SiO_2 microparticles in HDPE wax and a thickness of 6.4 mm. This gives a sample with low refractive index and extinction coefficient. Figure 7.2 below shows the results for parameter extraction with (Compensated) and without (Uncompensated) etalon estimation.

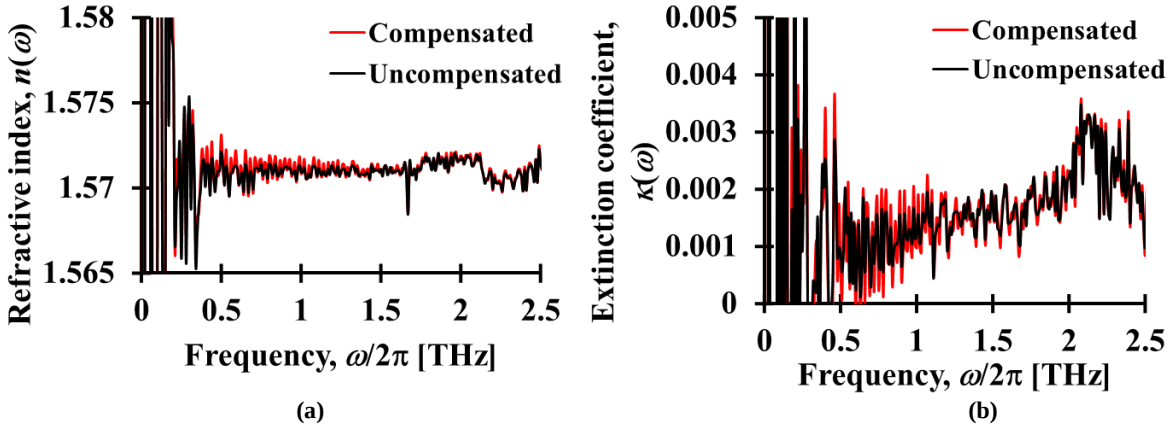

Figure 7.2: The extracted refractive index (a) and extinction coefficient (b) for composite sample comprised of approximately 8% of SiO_2 microparticles in HDPE wax is shown. The material parameters are extracted using two algorithms. One algorithm does not compensate for etalons (Uncompensated), while the other algorithm compensates for etalons by assuming a constant refractive index (Compensated).

The results for this case show that the low refractive index of the composite introduces minimal etalon effects regardless of which algorithm is chosen. Interestingly, the etalon compensation appears to actually introduce minor additional oscillations into the material parameters. Consequently, the material parameter estimation with and without etalon compensation are functionally equivalent for this type of sample. Therefore, the composite results presented in the thesis did not use any etalon compensation as it was not required.

Appendix C: Configuration Two

In configuration two, the reference frequency for the homodyne detection system is set to $\omega_{ref} = \omega_{pp}$. The THz probe frequency is set to zero, i.e. $\omega_{pr} = 0$. In this case, the expression for the measured spectrum becomes

$$V_d(\omega) = V_0(\omega)\frac{t_{in}(\omega)t_{out}(\omega)}{T_p}\int_0^{T_p}\cos(\omega_{pp}t)\frac{e^{-k_0(\kappa(\omega)+\Delta\kappa(\omega,t))\delta}e^{-jk_0(n(\omega)+\Delta n(\omega,t))\delta}}{1-r(\omega)^2e^{-2k_0(\kappa(\omega)+\Delta\kappa(\omega,t))\delta}e^{-j2k_0(n(\omega)+\Delta n(\omega,t))\delta}}dt\,, \qquad \text{(A3.1)}$$

which is a modified version of (5.5). To begin simplifying this expression, assumption 1, which is to ignore all internal reflections, is applied. This gives the measured spectrum to be

$$V_d(\omega) = V_0(\omega)\frac{t_{in}(\omega)t_{out}(\omega)}{T_p}e^{-k_0\kappa(\omega)\delta}e^{-jk_0n(\omega)\delta}\int_0^{T_p}\cos(\omega_{pp}t)e^{-k_0\Delta\kappa(\omega,t)\delta}e^{-jk_0\Delta n(\omega,t)\delta}dt\,. \qquad \text{(A3.2)}$$

Appling assumption 5, which states that $\kappa(\omega) = 0$ and $n(\omega) >> \Delta n(\omega,t)$, gives

$$V_d(\omega) = V_0(\omega)\frac{t_{in}(\omega)t_{out}(\omega)}{T_p}e^{-jk_0n(\omega)\delta}\int_0^{T_p}\cos(\omega_{pp}t)e^{-k_0\Delta\kappa(\omega,t)\delta}dt\,. \qquad \text{(A3.3)}$$

The challenge now is determining $\Delta\kappa(\omega,t)$. To do so, equation (5.7) for optically induced charge carrier density is first simplified using assumption 3, which stipulates that the square wave modulation can be approximated by its first term. This gives a charge carrier density of

$$N(t) = \frac{G_{op}\tau_r}{A_\phi\delta}\left(1+\frac{4}{\pi}\frac{\cos(\omega_{pp}t-\theta_1)}{\sqrt{1+(\omega_{pp}\tau_r)^2}}\right) = N_0\left(1+\frac{4}{\pi}\frac{\cos(\omega_{pp}t-\theta_1)}{\sqrt{1+(\omega_{pp}\tau_r)^2}}\right), \qquad \text{(A3.4)}$$

where the constant N_0 is a combination of several other constants. In order to relate this charge carrier density to a change in refractive index and extinction coefficient, the relationship between susceptibility and change in refractive index and extinction coefficient needs to be linearized. This is assumption 2 and gives

$$\sqrt{\tilde{n}(\omega)^2+(\tilde{\chi}_{\mathrm{e}}(\omega,t)+\tilde{\chi}_{\mathrm{h}}(\omega,t))}\approx\tilde{n}(\omega)+\frac{(\tilde{\chi}_{\mathrm{e}}(\omega,t)+\tilde{\chi}_{\mathrm{h}}(\omega,t))}{2\tilde{n}(\omega)}=\tilde{n}(\omega)+\Delta n(\omega,t)-\mathrm{j}(\Delta\kappa(\omega,t))\,, \tag{A3.5}$$

which can be simplified to

$$\frac{(\tilde{\chi}_{\mathrm{e}}(\omega,t)+\tilde{\chi}_{\mathrm{h}}(\omega,t))}{2\tilde{n}(\omega)}=\Delta n(\omega,t)-\mathrm{j}(\Delta\kappa(\omega,t))\,. \tag{A3.6}$$

Now, inserting (A3.4) into the susceptibilities gives

$$\Delta n(\omega,t)-\mathrm{j}\Delta\kappa(\omega,t)=\Delta n_0(\omega)\left(1+\frac{4}{\pi}\frac{\cos(\omega_{\mathrm{pp}}t-\theta_k)}{\sqrt{1+(\omega_{\mathrm{pp}}\tau_{\mathrm{r}})^2}}\right)-\mathrm{j}\Delta\kappa_0(\omega)\left(1+\frac{4}{\pi}\frac{\cos(\omega_{\mathrm{pp}}t-\theta_k)}{\sqrt{1+(\omega_{\mathrm{pp}}\tau_{\mathrm{r}})^2}}\right), \tag{A3.7}$$

where $\Delta n_0(\omega)$ and $\Delta\kappa_0(\omega)$ are the changes in refractive index and extinction coefficient induced by the scaling factor N_0. Taking the imaginary part of (A3.7) gives the change in extinction coefficient to be

$$\Delta\kappa(\omega,t)=\Delta\kappa_0(\omega)\left(1+\frac{4}{\pi}\frac{\cos(\omega_{\mathrm{pp}}t-\theta_k)}{\sqrt{1+(\omega_{\mathrm{pp}}\tau_{\mathrm{r}})^2}}\right). \tag{A3.8}$$

In order to insert (A3.8) back into (A3.3), the second exponential term in (A3.3) needs to be linearized. Assumption 4, which states that the absolute values of the terms in the second exponential function are much less than one, allows (A3.3) to be linearized into

$$V_2(\omega)=V_0(\omega)\frac{t_{\mathrm{in}}(\omega)t_{\mathrm{out}}(\omega)}{T_{\mathrm{p}}}e^{-jk_0n(\omega)\delta}\int_0^{T_{\mathrm{p}}}\left(\cos(\omega_{\mathrm{pp}}t)(1-k_0\Delta\kappa(\omega,t)\delta)\right)dt\,. \tag{A3.9}$$

This expression only takes the first two terms of the Taylor series. Inserting (A3.8) into (A3.9) and expanding gives

$$V_2(\omega)=V_0(\omega)\frac{t_{\mathrm{in}}(\omega)t_{\mathrm{out}}(\omega)}{T_{\mathrm{p}}}e^{-jk_0n(\omega)\delta}\int_0^{T_{\mathrm{p}}}\left(\cos(\omega_{\mathrm{pp}}t)-k_0\Delta\kappa_0(\omega)\cos(\omega_{\mathrm{pp}}t)\left(1+\frac{4}{\pi}\frac{\cos(\omega_{\mathrm{pp}}t-\theta_k)}{\sqrt{1+(\omega_{\mathrm{pp}}\tau_{\mathrm{r}})^2}}\right)\delta\right)dt\,. \tag{A3.10}$$

Multiplying further gives

$$V_{\mathrm{d}}(\omega) = V_0(\omega)\frac{t_{\mathrm{in}}(\omega)t_{\mathrm{out}}(\omega)}{T_{\mathrm{p}}}e^{-\mathrm{j}k_0 n(\omega)\delta} \times$$

$$\int_0^{T_{\mathrm{p}}} \cos(\omega_{\mathrm{pp}}t) - k_0\Delta\kappa_0(\omega)\delta\cos(\omega_{\mathrm{pp}}t) - k_0\Delta\kappa_0(\omega)\delta\cos(\omega_{\mathrm{pp}}t)\frac{4}{\pi}\frac{\cos(\omega_{\mathrm{pp}}t-\theta_k)}{\sqrt{1+(\omega_{\mathrm{pp}}\tau_{\mathrm{r}})^2}}dt\,. \qquad \text{(A3.11)}$$

The first two terms of the integral are zero after integration over one period giving

$$V_{\mathrm{d}}(\omega) = -V_0(\omega)\frac{t_{\mathrm{in}}(\omega)t_{\mathrm{out}}(\omega)}{T_{\mathrm{p}}}e^{-\mathrm{j}k_0 n(\omega)\delta}\frac{4}{\pi}\frac{k_0\Delta\kappa_0(\omega)\delta}{\sqrt{1+(\omega_{\mathrm{pp}}\tau_{\mathrm{r}})^2}}\int_0^{T_{\mathrm{p}}}\cos(\omega_{\mathrm{pp}}t)\cos(\omega_{\mathrm{pp}}t-\theta_k)dt\,. \qquad \text{(A3.12)}$$

Splitting up the second cosine and simplifying gives

$$V_{\mathrm{d}}(\omega) = -V_0(\omega)\frac{t_{\mathrm{in}}(\omega)t_{\mathrm{out}}(\omega)}{T_{\mathrm{p}}}e^{-\mathrm{j}k_0 n(\omega)\delta}\frac{4}{\pi}\frac{k_0\Delta\kappa_0(\omega)\delta}{\sqrt{1+(\omega_{\mathrm{pp}}\tau_{\mathrm{r}})^2}}\int_0^{T_{\mathrm{p}}}\cos^2(\omega_{\mathrm{pp}}t)\cos(\theta_k)+0.5\sin(2\omega_{\mathrm{pp}}t)\sin(\theta_k)dt\,. \qquad \text{(A3.13)}$$

The second term in the integral now goes to zero when integrating over one period giving

$$V_{\mathrm{d}}(\omega) = -V_0(\omega)\frac{t_{\mathrm{in}}(\omega)t_{\mathrm{out}}(\omega)}{T_{\mathrm{p}}}e^{-\mathrm{j}k_0 n(\omega)\delta}\frac{4}{\pi}\frac{k_0\Delta\kappa_0(\omega)\delta}{\sqrt{1+(\omega_{\mathrm{pp}}\tau_{\mathrm{r}})^2}}\cos(\theta_k)\int_0^{T_{\mathrm{p}}}\cos^2(\omega_{\mathrm{pp}}t)dt\,. \qquad \text{(A3.14)}$$

Now all that is left is to evaluate the integral, which gives

$$V_{\mathrm{d}}(\omega) = -V_0(\omega)\frac{t_{\mathrm{in}}(\omega)t_{\mathrm{out}}(\omega)}{T_{\mathrm{p}}}e^{-\mathrm{j}k_0 n(\omega)\delta}\frac{4}{\pi}\frac{k_0\Delta\kappa_0(\omega)\delta}{\sqrt{1+(\omega_{\mathrm{pp}}\tau_{\mathrm{r}})^2}}\cos(\theta_k)\frac{T_{\mathrm{p}}}{2}\,. \qquad \text{(A3.15)}$$

Simplifying and absorbing a few constants into V_0 gives

$$V_{\mathrm{d}}(\omega) = -\frac{V_0(\omega)t_{\mathrm{in}}(\omega)t_{\mathrm{out}}(\omega)k_0\Delta\kappa_0(\omega)\delta}{\sqrt{1+(\omega_{\mathrm{pp}}\tau_{\mathrm{r}})^2}}\cos(\theta_k)e^{-\mathrm{j}k_0 n(\omega)\delta}\,, \qquad \text{(A3.16)}$$

which is (5.11) in Section 5.2.